

ABSTRACT

Title of dissertation: HYBRID RANS LES SIMULATION
 OF NON-EQUILIBRIUM
 BOUNDARY LAYERS

Giuseppe De Prisco
Doctor of Philosophy, 2007

Dissertation directed by: Professor Ugo Piomelli
 Department of Mechanical Engineering

Hybrid simulations that couple the solution of the Reynolds-Averaged Navier-Stokes equations (RANS) to Large-Eddy Simulations (LES) have the ability to apply the high accuracy of LES only in regions of the flow that demand it, while using the less expensive RANS approach in regions of the flow where standard turbulence models are expected to be accurate, while LES is used in non-equilibrium flow regions. One issue that arises in these applications is the behavior of the flow in the transition zone between the RANS and LES regions. In the RANS zone the flow solution is either steady, or only contains information on the largest scales of motion; most or all of the Reynolds shear stress is provided by the turbulence model. In the LES region the resolved scales must supply most of the Reynolds shear stress. Typically, a transition zone exists in which the resolved eddies are gradually generated and grow.

In this work, methodologies for the improvement of hybrid LES/RANS are

studied, to shorten the transition from the smooth RANS field to the LES, which requires energy- and momentum-supporting eddies. The method tested is based on the generation of synthetic turbulence with a realistic spectrum, and statistics obtained from the RANS. The eddies thus generated are then selectively forced by a control method that amplifies the bursts, and maintains a desired Reynolds shear stress downstream of the RANS/LES interface. This method allows to match the two techniques smoothly, and to minimize the extent of the region required to develop the realistic turbulent eddies. It was found to perform well in several non-equilibrium boundary layers achieved by imposing either a variable freestream velocity or a spanwise pressure gradient on a flat-plate boundary layer. A finely resolved LES of the flow in a boundary layer subjected to strong acceleration was also performed. The flow in this configuration reverts to a laminar state and then retransitions to turbulence. Statistics and flow visualizations of this flow indicate the presence of two of the mechanisms that have been conjectured to cause the re-laminarization.

HYBRID RANS LES SIMULATION
OF NON-EQUILIBRIUM BOUNDARY LAYERS

by

Giuseppe De Prisco

Dissertation submitted to the Faculty of the Graduate School of the
University of Maryland, College Park in partial fulfillment
of the requirements for the degree of
Doctor of Philosophy
2007

Advisory Committee:
Professor Ugo Piomelli, Chair/Advisor
Professor Richard Calabrese,
Professor James Duncan
Professor Kenneth Kiger
Professor Elias Balaras

© Copyright by
Giuseppe De Prisco
2007

Acknowledgements

My special thanks to Professors Ugo Piomelli and Elias Balaras and Dr. Tony Keating for their guidance. Financial support of the Air Force Office of Scientific Research is gratefully acknowledged.

Effort sponsored by the Air Force Office of Scientific Research, under grant number FA95500610116, monitored by Dr. John D. Schmisser. The U.S. Government is authorized to reproduce and distribute reprints for Governmental purposes notwithstanding any copyright notation thereon. The views and conclusions contained herein are those of the authors and should not be interpreted as necessarily representing the official policies or endorsements, either expressed or implied, of the Air Force Office of Scientific Research or the U.S. Government.

Table of Contents

List of Figures	v
List of Abbreviations	x
1 Introduction	1
1.1 Motivation	1
1.2 Hybrid strategies: single grid and zonal approaches	4
1.3 Hybrid RANS/LES approach with single grid	8
1.3.1 Introduction	8
1.3.2 Previous work	8
1.4 Zonal Hybrid RANS/LES	16
1.4.1 Introduction	16
1.4.2 Inflow generation methods	18
1.4.3 Previous work	23
1.5 Plan of the present dissertation	25
2 Problem formulation	27
2.1 Governing equations	27
2.2 Numerical method and boundary conditions	29
2.3 Subgrid-scale modeling	32
2.3.1 Eddy-viscosity assumption	33
2.3.2 The dynamic procedure	34
2.3.3 Averaging of the eddy-viscosity coefficient	36
2.3.4 Filtering operations	37
2.4 RANS equations and Reynolds stress modeling	38
2.4.1 Spalart-Allmaras model	39
2.4.2 $k - \epsilon$ model	41
2.5 Synthetic turbulence generation	42
3 The controlled forcing method and its tuning	50
3.1 Introduction	50
3.2 Analysis of the controller parameters	53
3.2.1 Testing strategy: ZPG boundary layer	53
3.2.2 The moving-average exponential window	55
3.2.3 The PI control	60
3.2.4 Conclusions	66

4	Application of the controlled forcing	68
4.1	Introduction	68
4.1.1	Zero-pressure-gradient boundary layer	68
4.1.2	Adverse-pressure-gradient boundary layer	74
4.1.3	Favorable-pressure-gradient boundary layer	77
4.1.4	3-D Boundary layer	83
4.2	Conclusions	88
5	Favorable pressure gradient boundary layer	91
5.1	Introduction	91
5.2	Problem formulation	98
5.3	Results	100
5.4	Conclusions	115
6	Conclusion and future work	118
6.1	Hybrid RANS/LES	118
6.1.1	Control parameters	118
6.1.2	Applications	120
6.2	Resolved LES of the favorable pressure gradient boundary layer . . .	121
6.3	Future work	122
	Bibliography	124

List of Figures

1.1	Sketch of a hybrid method application with the boundary of the two domains parallel a) or orthogonal b) to the flow direction.	5
1.2	Sketch of a hybrid method application.	17
1.3	Sketch of the rescaling method (a) and recycling method (b).	19
2.1	Distribution of the wavenumbers d_i^n (top right) and modified wavenumbers $\frac{d_i^n}{c^n}$ for different distances from the wall: top right figure is for $y^+ = 12$, bottom left is $y^+ = 100$, and bottom right is $\frac{y}{\delta^*} = 5$	48
2.2	Synthetic fluctuation produced by the Batten's decomposition for different distance from the wall: bottom figure is for $y^+ = 12$, central is $y^+ = 100$, and top is $\frac{y}{\delta^*} = 5$ The distance are based on a LES calculation from which the Batten decomposition is evaluated.	49
3.1	Block diagram of the PI controller.	51
3.2	Sketch of the geometric configuration.	54
3.3	(a) Domain-averaged turbulent kinetic energy for $\cdots T_{ave} = 1, K_I = 5, K_P = 30$; $\text{---} T_{ave} = 10, K_I = 5, K_P = 30$; $\text{---} T_{ave} = 100, K_I = 1, K_P = 1$; $\text{---} T_{ave} = 100, K_I = 5, K_P = 30$. (b) C_f for the reference LES (\circ) and the cases shown in (a).	56
3.4	Skin friction coefficient C_f with $K_I = 5$ and $K_P = 30$; --- first control plane after one grid cell; --- first control plane after one boundary layer thickness	58
3.5	Skin friction coefficient C_f with $K_I = 5$ and $K_P = 30$; --- $\langle u'v' \rangle^t$ is spanwise-averaged; --- $\langle u'v' \rangle^t$ is not spanwise-averaged.	59
3.6	Bode plot of the frequency response of the PI system for different value of K_I and fixed $K_P = 30$. --- $K_I = 5$; --- $K_I = 20$; --- $K_I = 30$; It is evident that when K_I increase, the gain at low frequency increase and the phase lag value starting at -90 is kept to higher frequency, <i>i.e.</i> , the response of the PI system lags behind the input wave by 90 deg in the worst case	62

3.7	Bode plot of the amplitude and phase frequency response of the PI system for different values of K_P and fixed $K_I = 5$. — $K_P = 5$; - - - $K_P = 20$; - · - $K_P = 30$. When K_P increases, the gain at high frequency increase and the phase lag value decreases at higher frequency	63
3.8	Domain-averaged turbulent kinetic energy. (a) $K_I = 5$ and — $K_P = 0$; · · · · · 15; - - - 30; — 500; (b) $K_P = 30$ and — $K_I = 1$, - - - 5, - · - 20, · · · · · 30.	64
3.9	(a) Instantaneous and (b) integrated error for $K_P = 30$ and $K_I = 5$ (lines) and $K_I = 20$ (lines with symbols). — $y^+ = 13$; - - - $y/\delta_o^* = 4.5$. The curves for $K_I = 20$ are shifted upwards by 0.005 in (a) and 0.1 in (b).	65
4.1	Zero-pressure-gradient boundary layer. (a) Skin friction coefficient C_f (b) mean velocity profiles and (c) profiles of the Reynolds shear stress at the locations indicated by a vertical line in part (a). ○ Reference LES; — $k - \epsilon$ RANS; - - - Hybrid $k - \epsilon$ /LES; - · - SA RANS; - - - Hybrid SA/LES.	70
4.2	Zero-pressure-gradient boundary layer. (a) Skin friction coefficient C_f (b) mean velocity profiles and (c) profiles of the Reynolds shear stress at the locations indicated by a vertical line in part (a). ○ Reference LES; - · - SA RANS; - - - error based on $\langle u'v' \rangle$; — production-based error.	71
4.3	Skin friction coefficient C_f in the case of hybrid $k - \epsilon$ /LES simulation. ○ Reference LES; - - - RANS $k - \epsilon$; — Hybrid $k - \epsilon$ /LES with $T_{ave} = 10$, $K_I = 5$, $K_P = 30$; - - - Hybrid $k - \epsilon$ /LES with $T_{ave} = 100$, $K_I = 1$, $K_P = 1$ as in [30]; · · · · · Hybrid $k - \epsilon$ /LES with only Batten synthetic turbulence at the interface	72
4.4	Freestream velocity for the adverse-pressure-gradient calculation.	74
4.5	Adverse-pressure-gradient boundary layer. (a) Skin friction coefficient C_f (b) mean velocity profiles and (c) profiles of the Reynolds shear stress at the locations indicated by a vertical line in part (a). ○ Reference LES; - · - $k - \epsilon$ RANS, - · - SA RANS; — hybrid $k - \epsilon$ /LES; - - - Hybrid SA/LES.	76
4.6	Mean streamlines for the APG boundary layer. (a) Reference LES; (b) $k - \epsilon$ RANS; (c) SA-RANS; (d) hybrid $k - \epsilon$ /LES; (e) hybrid SA/LES.	78

4.7	Skin friction coefficient C_f in the case of LES/LES simulation (a) and hybrid RANS SA/LES (b). In (a) — $T_{ave} = 38$, $K_I = 5$, $K_P = 30$; — $T_{ave} = 100$, $K_I = 1$, $K_P = 1$ as in [30]. In (b) --- RANS SA model, --- hybrid SA/LES with $T_{ave} = 38$, $K_I = 5$, $K_P = 30$; --- $T_{ave} = 100$, $K_I = 1$, $K_P = 1$ as in [30]; Hybrid SA/LES with only Batten synthetic turbulence at the interface	79
4.8	Streamwise velocity fluctuations in the APG boundary layer, in the $y/\delta_o^* = 0.09$ plane. (a) Reference LES; (b) hybrid $k - \epsilon$ /LES; the red rectangle indicates the region where the control is active.	80
4.9	Favorable-pressure-gradient boundary layer. (a) Skin friction coefficient C_f (b) mean velocity profiles and (c) profiles of the Reynolds shear stress at the locations indicated by a vertical line in part (a). \circ Reference LES; SA RANS; — hybrid SA/LES, T_{ave} from LES data; --- hybrid SA/LES, T_{ave} from RANS data;	81
4.10	Skin friction parameter C_f for the favorable pressure gradient boundary layer: \circ reference LES, RANS, — hybrid RANS/LES with $T_{ave} = 2.4$ and --- $T_{ave} = 1$; Hybrid SA/LES with only Batten synthetic turbulence at the interface	82
4.11	3D boundary layer. Flow angle $\alpha = \tan^{-1} U/W$. \circ Reference LES. SA-RANS; --- error based on $\langle u'v' \rangle$; — production-based error.	84
4.12	Grid resolution obtained in the 3D boundary layers — $\Delta\zeta^+$; — $\Delta\zeta^+$	85
4.13	3D boundary layer. (a) Streamwise and spanwise skin friction coefficients, $C_{f,x}$ and $C_{f,z}$; (b) mean streamwise velocity profiles and (c) mean spanwise velocity profiles at the locations indicated by a vertical line in part (a). \circ Reference LES; SA RANS; --- error based on $\langle u'v' \rangle$; — production-based error.	86
4.14	3D boundary layer. (a) Streamwise and spanwise skin friction coefficients, $C_{f,x}$ and $C_{f,z}$; (b) secondary shear stress $\langle v'w' \rangle$ and (c) principal shear stress $\langle u'v' \rangle$ at the locations indicated by a vertical line in part (a). \circ Reference LES; SA RANS; --- error based on $\langle u'v' \rangle$; — production-based error.	87
4.15	Contours of streamwise velocity fuctuations in a xz -plane at $y/\delta_o^* = 0.18$. (a) Reference LES (only part of the domain is shown); (b) hybrid RANS/LES.	88

5.1	Sketch of the configuration. The computational domain is shown as a hatched area.	99
5.2	Streamwise development of statistical quantities. (a) Freestream velocity, U_∞/U_o and friction velocity $u_\tau/u_{\tau,o}$; (b) Acceleration parameter K ; (c) Momentum-thickness Reynolds number Re_θ ; (d) Skin friction coefficient C_f . • Experiments [97]; — high- K case; --- low- K case; — ZPG boundary-layer correlation.	102
5.3	Wall-normal profiles of the mean streamwise velocity at the locations shown in the top figure. • Experiments [97]; — high- K case; --- low- K case. Each profile is shifted by 0.5 units for clarity	103
5.4	Wall-normal profiles of the mean streamwise velocity in inner coordinates at the locations shown in the top figure. • Experiments [97]; — high- K case; --- low- K case; — $U^+ = 2.5 \log y^+ + 5$. Each profile is shifted by 18.0 units for clarity	104
5.5	Wall-normal profiles of the streamwise Reynolds stresses at the locations shown in the top figure. • Experiments [97]; — high- K case; --- low- K case. Each profile is shifted by 12.0 units for clarity . . .	106
5.6	Wall-normal profiles of the Reynolds shear stresses at the locations shown in the top figure. • Experiments [97]; — high- K case; --- low- K case. Each profile is shifted by 0.8 units for clarity	107
5.7	Contours of averaged quantities for the high- K case. The red line shows the local boundary layer thickness δ_{99} . (a) $\langle u'u' \rangle / U_\infty^2$; (b) $\langle v'v' \rangle / U_\infty^2$; (c) $\langle u'v' \rangle / U_\infty^2$; (d) $C_{uv} = \langle u'v' \rangle / u_{rms}v_{rms}$	108
5.8	Development of the Reynolds stresses along selected streamlines. (a) Streamline coordinates; (b) $\langle u'u' \rangle / U_o^2$; (c) $\langle v'v' \rangle / U_o^2$; (d) $\langle u'v' \rangle / U_o^2$. The thick black line corresponds to the boundary-layer edge. Streamline originating in: — outer-layer; --- middle boundary layer; - - - - - log region; - - - - - viscous sublayer.	109
5.9	Development of a_1 parameter and correlation coefficient along selected streamlines. (a) Streamline coordinates; (b) a_1 ; (c) C_{uv} . The thick black line corresponds to the boundary-layer edge. Streamline originating in: — outer-layer; --- middle of the boundary layer; - - - - - logarithmic region; - - - - - viscous sublayer.	111
5.10	Instantaneous contours of u' velocity fluctuations in a plane parallel to the wall.	113

5.11	Instantaneous isosurfaces of $Q = -0.002$ in the outer layer colored by the streamwise vorticity.	114
5.12	Contours of instantaneous $u'v'$ correlation in planes normal to the mean flow, and secondary $(v - w)$ velocity vectors. The two solid lines represent contours of $U/U_\infty = 0.95$ and 0.99	116

List of Abbreviations

3D	Three-dimensional
APG	Adverse pressure gradient
CPU	Central processing unit
DES	Detached eddy simulation
DNS	Direct numerical simulation
FPG	Favorable pressure gradient
LES	Large eddy simulation
LNS	Limited Numerical Scales
NLDE	Non-linear disturbance equations
NS	Navier-Stokes
RANS	Reynolds averaged Navier-Stokes
TKE	Turbulent kinetic energy
URANS	Unsteady RANS
WLES	Wall-modeled LES
ZPG	Zero pressure gradient
K_P	Proportional parameter
Re	Reynolds number based on the reference length and velocity scale
S_{ij}	Strain rate tensor
U	A velocity scale
U_o	Free stream input velocity
f	generic function
\bar{f}	filtered function
k	Turbulent kinetic energy
p	Pressure
t	Nondimensional time
u (u_1)	Streamwise velocity component
v (u_2)	Wall-normal velocity component
w (u_3)	Spanwise velocity component
x (x_1)	Streamwise coordinate
y (x_2)	Wall-normal coordinate
z (x_3)	Spanwise coordinate
$\bar{\Delta}$	filter width
ϵ	Komlogorov eddy dissipation rate
ν	Kinematic viscosity
ρ	Density
τ_{ij}	The subgrid-scale stress
τ_w	The wall stress
θ	Boundary-layer momentum thickness

Chapter 1

Introduction

1.1 Motivation

Recent years have seen the spread of inexpensive parallel computer clusters that are able to reduce the computational time for the solution of numerical models; at the same time smart computational strategies that allow for faster simulations without compromising the accuracy of the results have been developed. These developments have allowed the extension of the numerical solution of the Navier-Stokes equations to turbulent flows in more realistic configurations than possible until now.

The solution of turbulent flow problems is theoretically possible through the direct numerical simulation (DNS) of the Navier Stokes equation (with appropriate boundary conditions). This method constitutes the conceptually simplest approach to the problem of turbulence. Practically, however, the cost of DNS confines this approach to simple application in terms of Reynolds number and geometry complexities. In fact, in DNS all the scales of motion must be resolved, from the integral (L) to the Kolmogorov (η) scales. The grid size must be on the order of the smallest scale, and the computational domain must be on the order of the largest scale. This results in a number of grid points in each direction that is proportional to the ratio

between the largest and the smallest scale ($\frac{L}{\eta}$). Defining a Reynolds number based on the integral scale L , Re_L , the number of grid points will be proportional to $Re_L^{\frac{3}{4}}$ in each direction, so a total number of points proportional to $Re_L^{\frac{9}{4}}$ is required by DNS. Moreover, the equations must be integrated for a time on the order of the integral time scale (T). Supposing that the time step of the calculation Δt is limited by the CFL condition, that is $\Delta t < \frac{\Delta x}{V}$ where V is the local velocity determined by the integral time and length scale, we have that the total number of points in time is $\frac{T}{\Delta t}$ again proportional to ($\frac{L}{\eta}$). In this way the total cost of a DNS calculation will be on the order of Re_L^3 . This means that for high Re number, the DNS takes an unrealistic time to be completed: assuming that a computer power will increase by a factor of 5 every five years, Spalart [1] estimated that DNS will not be applicable to the study of the flow over an airliner or a car until 2080.

In large-eddy simulations (LES) the target is to simulate only the eddies containing the bulk of the energy of the flow. These scales are typically anisotropic and are dependent on the boundary conditions of the problem, therefore they are extremely difficult to be modeled analytically; the fact that the small, dissipative eddies are modeled reduces the cost of LES considerably compared with DNS. However, when LES have to be applied to wall-bounded flows at high Reynolds numbers it is still very demanding because of the inner layer resolution. In fact, as found in Chapman [2], considering a flat-plate boundary layer, the outer part has energy-carry structures on the order of the boundary layer thickness δ . Assuming that

the grid spacing is fixed in the stream and spanwise direction and on the order of 0.1δ , Chapman estimated a total number of grid points proportional to $Re^{0.4}$. In the inner part of the boundary layer, on the other hand, the number of points must be based on the inner units; in fact, the dimension of quasi-streamwise vortices are constant in wall units (*i.e.*, normalized by kinematic viscosity, wall stress and fluid density). In this way, the total cost of the calculation in the inner layer is estimated be proportional to $C_f Re_L^2$ which, assuming $C_f \sim Re_L^{-0.2}$, makes again this technique only suitable for moderate Reynolds number applications.

A powerful way to use LES is either to apply it in non-bounded flow simulations, or to use LES calculations only on the outer part of the flow. Wall-modeled LES (WMLES), in which the inner layer is modeled either by the Reynolds-Averaged Navier-Stokes (RANS) equations or through approximate boundary conditions, can be a smart solution to the expensive full LES (see the review in Ref. [3]). Spalart [1], however, estimates that application of WMLES to external flow of aeronautical interest is still several decades away from being practical. His estimate assumes the presence, in these flows, of very thin boundary layers (near the wing leading-edge, for instance), where a large number of points is required to cover a small physical area. In environmental or oceanographic flows, in which the Reynolds numbers are comparably high, but the boundary layers are thicker, WMLES is already applicable to practical problems.

Traditionally, high-Reynolds number flows have been predicted using RANS

models. However, RANS is designed to be accurate for problems such as thin shear layers. In many cases, especially in the presence of fluid-dynamical non-equilibrium, RANS cannot give an accurate prediction. A possible avenue to solve fluid-flow problems in practical engineering cases, then, is by using a combination of RANS and LES, in which the RANS equations are solved in quasi-equilibrium regions or where the models can be accurately tuned, while LES or WMLES are used in non-equilibrium regions or where the RANS models are expected to fail. Hybrid LES/RANS techniques have emerged as a tool that allows the simulation of complex fluid flows within reasonable amounts of CPU time. In fact, in recent years the hybrid methods have received increasing attention; different terminologies have been used as LNS, DES, PANS, zonal approach, single grid approach, etc. The target of this chapter is to introduce and discuss the different methods and try to underline the drawbacks and key points of each. A review of previous work is, in some cases, necessary in order to understand the motivation of the new hybrid strategies. In the next section, an overview of hybrid strategies is presented. Detailed descriptions of each method can be found in Sections 1.3 and 1.4. The chapter is concluded with an analysis of the hybrid method used in the rest of the present dissertation.

1.2 Hybrid strategies: single grid and zonal approaches

It is conceptually possible to divide the hybrid RANS/LES methods into two main categories: one in which a single grid is used and only the turbulence model

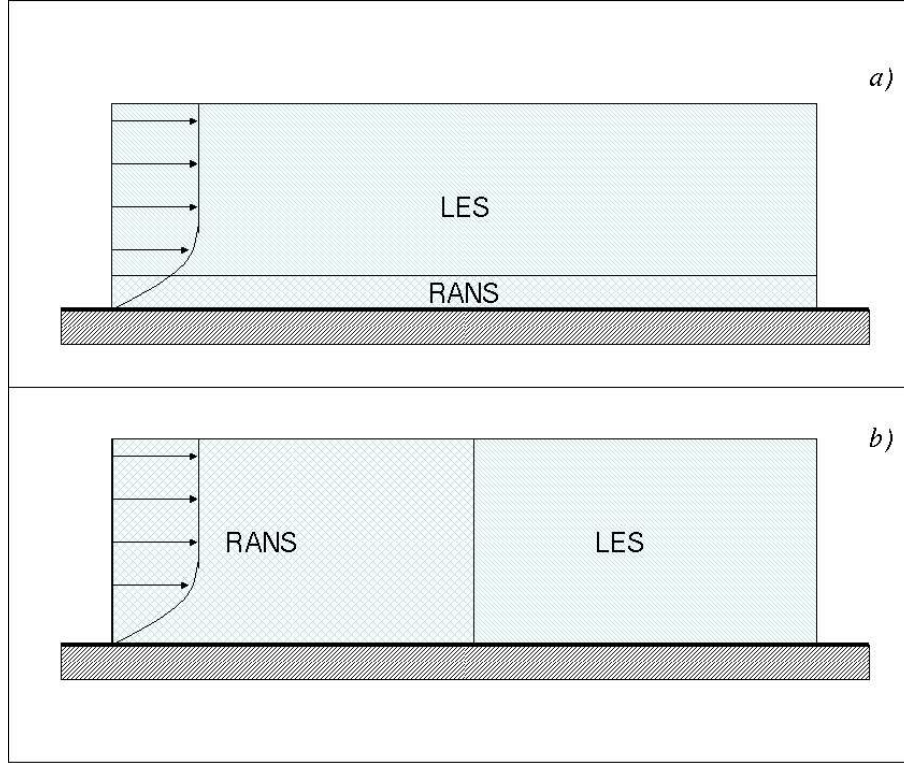


Figure 1.1: Sketch of a hybrid method application with the boundary of the two domains parallel a) or orthogonal b) to the flow direction.

changes; another case occurs when the RANS/LES domains are separated, and two separate grids as well as sets of equations are used (zonal approach). In both cases, two different scenarios are possible, as shown in figure 1.1: the interface of the two domains can be parallel or orthogonal to the flow direction. This interface can be either a true discontinuous interface that separates the two domains as in the zonal methods, or can be representative of a region in which the model gradually switches from RANS to LES calculations as in the single grid methods.

One issue that arises when hybrid RANS/LES methods are used is the behavior

of the flow in this transition zone between the RANS and LES regions, and how that region could affect the downstream results. In the RANS zone the flow solution is either steady, or only contains information on the largest scales of motion if unsteadiness is present; most, or all, of the Reynolds shear stress is provided by the turbulence model. In the LES region, on the other hand, the resolved scales must supply most of the Reynolds shear stress and small scale structures must be present to provide it. In both the zonal approach where the interface between the two domains is explicit, and the single-grid method where the interface is an overlapping zone between RANS/LES, a transition zone exists in which the resolved, energy-containing eddies are gradually generated and grow. In this region the flow may be unphysical. Different hybrid methods, that are illustrated in this paragraph, have different ways to switch from RANS and LES to trigger instabilities and to develop small eddies to support LES calculations. In the next section each method will be addressed with emphasis on the literature available.

In the single grid approach, the switch from RANS to LES is typically smooth and determined by the damping of the turbulent viscosity: in the LES region it must be damped to the levels implied by the sub-grid model. The damping can be a function of the grid spacing, as in DES where the level of the effective sub-grid viscosity is a function of the local mesh spacing and/or distance from the wall; or the damping is a function of turbulence quantities as in the LNS of Batten *et al.* [8] where the turbulent viscosity is damped through a blending function that depends

on length and velocity scales; the damping can also be a combination of the two (Speziale’s latency parameter [7]). In the zonal approach, on the other hand, the switch between RANS and LES is, by definition, explicit: two separate domains are defined and two different sets of equations, RANS and LES, are solved. The problem, in this case, is how to transfer information between the two domains: appropriate boundary conditions are needed for each domain; these can give either a two-way coupling (RANS solution influences the full LES and *vice versa*) or a one-way coupling.

As mentioned above, another issue is the generation of the energy-carry eddies in the transition zone. If a natural instability is present in the RANS/LES transition area the small eddies are generated by the natural amplification of noise or small fluctuations. This instability is particularly effective if adverse pressure gradients, separated shear layers or other very unstable flow features are present. In the case where such features are not present, other techniques must be implemented to generate turbulent fluctuations quickly. In the next sections we will describe some of these methods: forcing methods that add energy in the LES domain through the addition of forcing terms in the momentum equations, the method that recycles and rescales fluctuations from the downstream part of the calculation, and techniques that introduce coherent structures taken from a precursor calculation. Each of these methods will be illustrated in the next sections either applied to a single grid calculation or to zonal hybrid methods.

1.3 Hybrid RANS/LES approach with single grid

1.3.1 Introduction

As pointed out in the first section, the bottleneck of LES is the calculation of the flow dynamics close to the wall. To avoid this costly requirement, it is necessary to model the inner part of the flow in a less expensive way, from a computational perspective, than the full LES solution. Many hybrid methods try to achieve this end, by using RANS in the boundary layer (or in the inner layer) and LES away from solid walls. In the following, an overview of the literature of single grid approaches is presented.

1.3.2 Previous work

One of the first theoretical approaches to hybrid RANS/LES was due to Speziale [7] where the model Reynolds stress was damped by a latency factor that was a function of the grid size and the Kolmogorov scale. In this way, Speziale was able to merge RANS and LES depending on the grid size and/or Reynolds number. However, some parameters in the latency factor were never completely specified by Speziale. Moreover, the choice of the Kolmogorov length scale and the grid size as parameters to damp the eddy viscosity appear to be too drastic: for high Re numbers we can expect that no grid is fine enough to result in an LES calculation (since the ratio between grid size and Kolmogorov scale remains large). The latency

factor of Speziale [7], appears to be more of an on/off switch from RANS to full DNS because of the Kolmogorov length scale used in the model.

The method proposed by Batten *et al.*, the Limited Numerical Scales (LNS) approach [8], is an attempt to improve Speziale’s approach: they defined a parameter-free latency factor, based on some characteristic length and velocity scale of LES and RANS models. In the LNS approach the unresolved stress is a fraction of that predicted by a RANS model; the fraction was determined by a ratio of LES and RANS length- and velocity-scales. In this model the blending of the eddy viscosity is based entirely on RANS and LES quantities with no other empirical constants involved. One of the issues of the LNS approach regards the generation of small eddies in the LES region, when no natural instability, such as those present in massively separated flow, was present in the domain. In order to accelerate the generation of turbulent structures, Batten *et al.* [31] introduced a method to generate synthetic turbulence, based on Kraichnan’s [46] proposal, that takes into account the anisotropy of the flow. The method by Batten *et al.* [31] is based on the superposition of sinusoidal modes with random frequencies and wave-numbers, with given moments and spectra. The wave-numbers are modulated to yield eddies that are more elongated in the direction of larger Reynolds stresses, thus introducing more realistic, anisotropic eddies into the flow. Batten *et al.* [31] performed calculations of the spatially developing flow in a channel in which the inlet section had a very coarse grid in the streamwise direction, capable of supporting a RANS solution but

not an LES. The grid was then suddenly clustered, and forcing terms were used to generate synthetic turbulence.

The synthetic turbulence generation method proposed by Batten *et al.* [43, 31] was significantly more effective than older, simpler, methods. For instance, Le *et al.* [44] performed calculations of a backward-facing step in which at the inflow they assigned a mean velocity profile plus a superposition of random fluctuations with given moments and spectra. The amplitude of the random fluctuations was such that the bulk of the energy was contained in a range of well-resolved wave-lengths [45]. Since the fluctuations lacked phase information, however, the turbulence levels decayed rapidly, and only some distance downstream the turbulent eddies regenerated.

The most popular of the hybrid RANS/LES techniques that fall in the “single-grid category” is Detached Eddy Simulation [5]. In this model the switch between RANS and LES is determined by the grid size: when the mesh becomes small enough to resolve the energy-carrying eddies the eddy viscosity is reduced. DES was designed for the simulation of massively separated flows, in which the integral scales of motion in the separated flow region are determined by the geometry, and their size is not significantly affected by the Reynolds number. Applying LES in this region, therefore, results in a relatively small increase of the cost of the calculation compared, for instance, with an Unsteady RANS (URANS) model. Thus, in standard applications of this method, the thin attached shear layers are modeled by RANS, and only away from solid bodies the technique switches to LES, and the

RANS/LES interface occurs generally in the separated shear layers. The strong instability caused by the inflection points in the velocity profiles is extremely beneficial from the point of view of the generation of energy-carrying eddies, since any disturbance present in the flow is quickly amplified, resulting in a very short transition region. The application of DES to flows with weaker instability mechanisms or with thick boundary layer, however, creates some problems: if the turbulent eddies do not grow sufficiently fast, the simulations can become inaccurate as the modeled shear stress decreases while the resolved one does not increase sufficiently fast. Such quantities as the mean velocity profile, skin friction coefficient and separation location can be significantly in error. This case is typical [9] when the grid cells parallel to the wall are refined and become of the same order of the boundary layer thickness within the boundary layer region, with the boundary layer attached to the wall. In this case, within the boundary layer, the grid spacing is fine enough to switch the calculation to LES solution by decreasing the amplitude of the eddy viscosity, but the turbulent eddies are not yet generated. Another challenging case is when the grid is refined enough to switch the model to LES, but not fine enough to support resolved velocity fluctuations internal to the boundary layer: in that region the solution is neither a pure RANS, nor a pure LES. In these kinds of scenarios, the grid plays a key role: it must be fine enough to support eddies and damp in an appropriate way the eddy viscosity; this double achievement is the cause of error of the DES model (gray region).

At this point it is important to stress that the problem mentioned in the DES calculation is not solely specific to that kind of method. In fact, as mentioned in the previous section, a transition zone exists in all of the hybrid RANS/LES methods, in which energy-containing eddies are gradually generated and grow. This issue is of outstanding importance for the prediction of the correct behavior of the solution, especially in the case where separation of the flow is not determined by the geometry of the problem. One first solution to the problem mentioned was already illustrated: the Batten *et al.* [31] decomposition. In the following paragraphs, we will present other solutions to overcome the limitations of the gray area.

The problems of the gray area have motivated the use of zonal-DES approach [11], in which attached boundary layer regions are modeled by RANS independently of the grid spacing. In this way, the user can refine the grid as much as desired in the LES region, and use RANS in all of the regions where an attached boundary layer is expected. This “manual” switching is, however, too elaborate to be applied in a complex 3D geometry and could be a source of error.

Recently, to overcome the problem of the gray region, Spalart *et al.* [9] modified the DES approach and introduced the Delayed Detached Eddy Simulation (DDES), which maintains the RANS solution in the boundary layers independently of the grid spacing. They started from the idea of Menter *et al.* [75], who used appropriate functions in the SST RANS model to identify the boundary layers and prevent the switch to the LES model within that region; the DDES of Spalart *et al.*

[9] is applicable to any RANS model that involves an eddy viscosity. Spalart *et al.* [9] performed calculations on boundary layers, on a single and multi-element airfoil, a cylinder, and a backward-facing step and proved that the RANS solution was maintained in thick boundary layers, and switched in LES after massive separation.

Another method that used one grid is the Partially Averaged Navier Stokes (PANS) solution by Girimaji *et al.* [10]. In this method the averaging of the Navier Stokes equation is performed only over a portion of the fluctuating scales. The scale-resolution (cutoff) of the PANS closure is controlled by two model parameters: the fraction of unresolved kinetic energy and unresolved dissipation. The model production-to-dissipation ratio must be consistent with the turbulence physics at the cutoff to give accurate results. Girimaji *et al.* [10] applied this method in a flow past a circular cylinder and a flow past a backward facing step with encouraging results.

The trend in the most recent hybrid solutions to the one-grid hybrid RANS/LES is to apply a technique that resembles the wall-modeled LES. As described in [9], wall-modeled LES (WMLES) was introduced in the 1970s. An extensive review of wall-layers models can be found in Cabot *et al.* [13] and Piomelli *et al.* [3]. Here only a brief summary will be given.

An early application of WMLES can be found in Balaras [6]: the Two-layer model (TLM); here a simplified (parabolized) version of the momentum equations was solved in the inner layer together with a turbulence-model equation; the bound-

ary conditions were taken from the external LES. The solution of the simple set of equations provided the wall-shear stress imposed in the LES calculation. In this case the coupling between the near-wall region and the outer region was supposed to be weak from inner to outer layer and strong in the opposite direction (two way coupling).

Nikitin *et al.* [12], used DES as a wall-layer model in high Re numbers of turbulent channel flow, letting the model switch from RANS to LES behavior inside the boundary layer. In the inner layer the Reynolds shear stress was provided entirely by the turbulence model. In the outer part, the eddy viscosity was damped, which allowed the formation of turbulent eddies. The results that they obtained were promising: a clear logarithmic law was observed, and turbulence in the outer layer was sustained with a grid not particularly fine. The skin friction coefficient, however, was under-predicted.

Improved results in an attached flow were obtained when backscatter forcing was used [15] to introduce small-scale fluctuations in the transition region. This stochastic forcing generated small-scale fluctuations that acted as “seeds” for the development of realistic, energy-carrying eddies in the LES region. Piomelli *et al.* [15] found that with the correct amount of backscatter they could successfully remove the shift in the log-law, and improve the prediction of the skin friction coefficient. Although this work showed a promising approach to the solution of the RANS/LES interface problem, the backscatter model proposed lacked physical justification, and

tuning the forcing magnitude was required as the grid or the Reynolds number were changed. To overcome this problem, Keating *et al.* [20] introduced a dynamic method to calculate the magnitude of the stochastic forcing, based on the fact that in the interface region, the resolved Reynolds shear stress should become larger than the modeled one. They applied the method to a turbulent channel flow.

Davidson *et al.* [18] and Dahlstrom *et al.* [23], add turbulent fluctuations, synthesized or from a DNS precursor simulation, to the momentum equation at the interface region RANS/LES to generate rapidly turbulent structure in the LES region. The source terms are scaled in order to match turbulent kinetic energy modeled with the RANS. They found that the turbulent length scale of the synthesized fluctuation has a large impact on the results. In these cases, the turbulent length scale and the eddy viscosity are not the same in the LES and RANS domain.

Tessicini *et al.* [21] instead, used an URANS close to the wall and an LES subgrid scale model in the outer part where they adjusted dynamically the constant C_μ in the turbulent viscosity model of RANS to have a continuity between the two regions. The smooth transition between the constant value of C_μ in the inner RANS domain to the value calculated dynamically, is obtained by an empirical smoothing exponential function.

As can be seen from the last authors cited, better results were in general obtained by adding energy at the interface where the switch from RANS to LES was supposed to be. This is a problem very similar to the other approach zonal

RANS/LES, where an explicit interface between the two domains exist. This zonal approach will be presented in the next section.

1.4 Zonal Hybrid RANS/LES

1.4.1 Introduction

We focus, in this work, on applications of hybrid RANS/LES methods of the type shown in Figure 1.2, in which RANS is used in equilibrium regions of the flow, while LES is performed in a small part of the domain, possibly including attached boundary layers as well as separated flow. As shown in Figure 1.2, the separation between RANS and LES calculations is pre-defined, so a smooth transition of the eddy viscosity between the two domains does not have to be defined. The interface RANS/LES defines the two regions in a discontinuous way: the turbulent kinetic energy is zero in the RANS domain and not zero in the other. The main difficulty is now that information must be exchanged between two solutions radically different in their energy content: RANS or unsteady RANS (URANS) in one domain and LES in the other.

The interface problem is critical for applications in which the upstream flow is essential for predicting the correct behavior of the flow downstream; one case is when the flow undergoes separation, and errors in the separation prediction can affect the flow for long distances downstream. In this type of configuration the generation of energy- and momentum-carrying eddies is expected to be much slower,

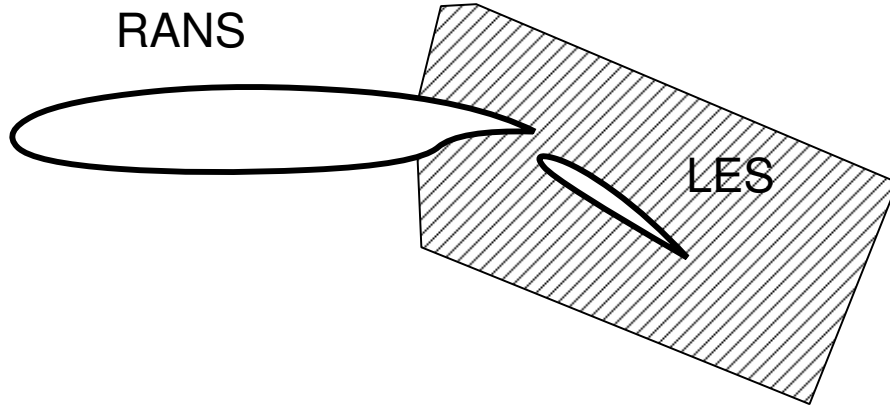


Figure 1.2: Sketch of a hybrid method application.

as the instability mechanism in the attached boundary layer is weaker than in the separated shear layer. Using the RANS solution alone to feed the LES domain is not sufficient, but further modeling must be included in order to have an accurate LES simulation.

One way to couple RANS and LES is by adding an external source of energy on the boundary of the two domains for the generation of small scales needed in the LES domain. The external source of energy can be either a stochastic reconstruction of the turbulent fluctuations, or a precursor simulation to feed the required unsteady flow to the LES domain. These reconstructions, of course, must match the upstream field given by the RANS model in a statistical sense.

The problem of generating turbulent fluctuations for the LES domain is analogous to the problem of inflow conditions for LES and DNS simulations. In the following subsection we will describe the most common methods of inflow generation for spatially developing problems that have been used in LES. We will particularly

stress those methods that have a more immediate application to hybrid RANS/LES calculations.

1.4.2 Inflow generation methods

The first applications of LES were to temporally developing flows, in which it was possible to use periodic boundary conditions in the direction of homogeneity. To extend LES to the more realistic spatially developing cases, initially modifications of the periodic boundary conditions were developed that either added extra terms to the governing equations to account for the boundary-layer growth [34, 35, 36] or rescaled the fluctuations before applying periodicity [102, 38] (see Figure 1.3 a). These methods have some shortcomings: first, they require a longer computational domain, and can be applied only if some similarity law exists, at least in the initial part of the domain. Furthermore, it is not easy to control precisely the inflow parameters (boundary-layer thickness and wall stress, in particular)

Schlüter *et al.* [40] adopted a method that improved the recycling by Lund *et al.* [102]: they introduced fluctuations that already have some level of correlation at the inflow of the LES. To this end they specified the inflow by superposing to a mean flow obtained from the RANS, the fluctuations obtained from a separate LES of a wall-bounded flow. These fluctuations were rescaled to match the Reynolds stresses predicted by the RANS. A similar method, that uses an auxiliary calculation in which the mean profile is assigned to match the RANS result was recently proposed

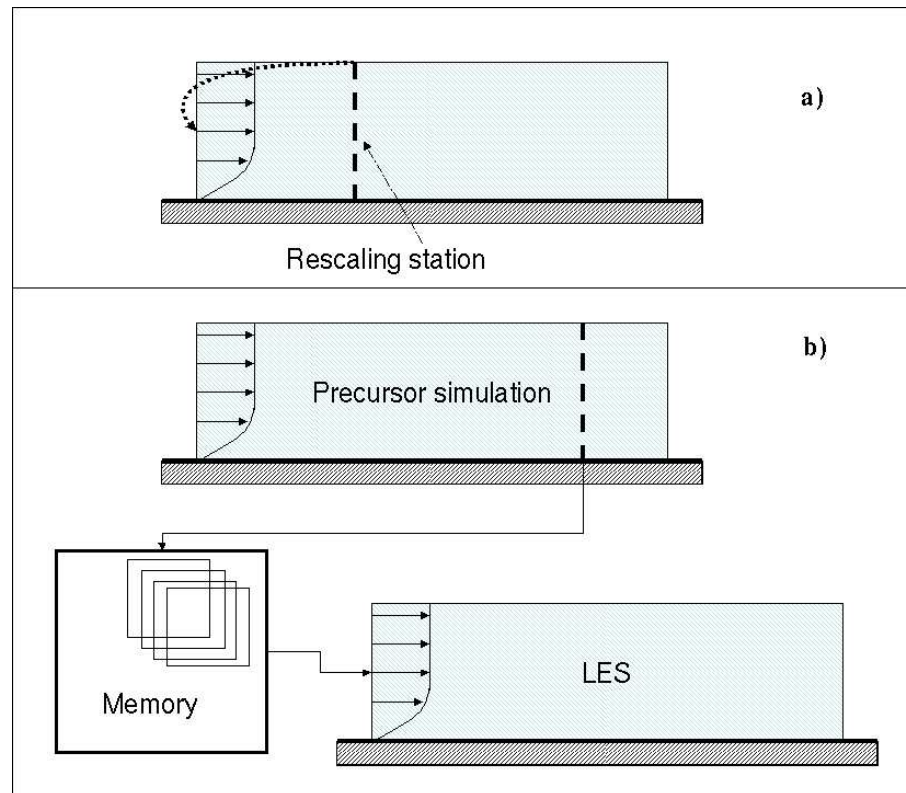


Figure 1.3: Sketch of the rescaling method (a) and recycling method (b).

by Medic *et al.* [41].

Another method to generate inflow conditions, (see Figure 1.3 b) consists of running a separate, precursor, calculation of an equilibrium flow in which either periodic boundary conditions or recycling arguments can be used. Then, a plane of velocity data orthogonal to the flow direction is stored at each time step. The sequence of planes is then read-in as inflow data for a separate calculation of the flow of interest, with a necessary space and time interpolation. This method has the advantage, over recycling methods, that the control of integral parameters can be achieved precisely but may require considerable additional computational resources.

Recycling and precursor techniques are very efficient for simple geometries; however, the application to complex three-dimensional geometries, non-equilibrium flow and arbitrary meshes presents some challenges [43]. Because of the limitations of these approaches, several researchers have attempted to develop methods to generate realistic inflow conditions from synthetic turbulence.

Le *et al.* [44] performed calculations of a backward-facing step in which at the inflow they assigned a mean velocity profile plus a superposition of random fluctuations with given moments and spectra. The amplitude of the random fluctuations was such that the bulk of the energy was contained in a range of well-resolved wave-lengths [45]. Since the fluctuations lacked phase information, however, the turbulence levels decayed rapidly, and only some distance downstream the turbulent eddies regenerated.

Synthetic turbulence generation methods like that one by Batten *et al.* [31] described in the previous section, have also been proposed by Smirnov *et al.* [47] and Klein *et al.* [48]. These methods achieve improved results (compared with the simple superposition of random fluctuations) by a judicious assignment of the turbulence spectrum and by trying to match the flow anisotropy. An important feature of turbulence in wall-bounded flows is its structure, however; since none of these methods contains realistic phase information between the modes, a fairly long adjustment region downstream of the inflow is unavoidable. In this region the initially random fluctuations are selectively amplified by the flow, and realistic turbulent eddies are generated.

A procedure to obtain flow field with temporal correlation was applied by Davidson [32]; he generates new fluctuating velocity with a prescribed time exponential correlation with a time scale proportional to the turbulent time scale. He applied the methods to an hybrid LES/RANS channel flow and found that the time scale was more important than the length scale and that both should not be based on physical values but related to the grid.

Another method to generate synthetic turbulence was adopted by Sandham *et al.* [33]. It is based on the fact that outer and inner part of a boundary layer are dominated by large scale coherent structures and low speed streaks respectively; they, therefore, introduced streamwise and spanwise disturbances with deterministic phase information, and frequencies and wave numbers chosen to match typical size of

the coherent structures in the inner and outer part of the boundary layer. Moreover, the spanwise component was computed using the divergence-free condition. To break any remaining symmetries in the inflow condition, random noise was added. They tested his method for a flat plate turbulent boundary layer.

Recently, Mathey *et. al* [28] apply a vortex method to generate random fluctuations representing a turbulent field at the inlet of an LES domain. The generated velocity field has temporal and spatial correlation. A perturbation is added on a specified mean velocity profile via a fluctuating two dimensional vorticity field. Mathey *et. al* [28] validate the vortex method on fully developed turbulent channel flow, pipe flow and separated hill obtaining results that compare well with the reference data. However, they only used methods based on simple random noise for comparison.

These methods achieve improved results (compared with the simple superposition of random fluctuations) by a judicious assignment of the turbulence spectrum and by trying to match the flow anisotropy. As a result, their downstream development is more realistic than when random noise was used. In all cases, however, we continue to observe an initial decay of the turbulence levels (albeit shorter than with simpler specifications) followed by an eventual establishment of realistic turbulence.

This was shown by Keating *et al.* [50], who compared various types of inflow conditions for LES, among them the use of random noise, the adapted database method by Schlüter [40], the synthetic turbulence generation method proposed by

Batten *et al.* [31], and a method based on controlled forcing proposed by Spille-Kohoff and Kaltenbach [49]. This method is based on the selective amplification of strong bursts downstream of an inflow supplied by some synthetic turbulence generation method. A controller is used at several location downstream of the inflow to determine the amplitude of a forcing term in the wall-normal momentum equation. This forcing term acts to reinforce the more realistic eddies, by requiring that a desired Reynolds shear-stress profile (obtained from the RANS, or from experiments) be achieved. They found that the adapted database and the controlled forcing methods resulted in significantly shorter development lengths than any of the other techniques.

1.4.3 Previous work

Applications of the type sketched in Figure 1.2 have been studied by zonal hybrid RANS/LES methods by several researchers. Labourasse and Sagaut [24], for instance, developed a coupling method to perform LES overlaid on a mean flow generated by RANS. The RANS parametrization yields the mean flow field over the entire region, while the LES equations, which are formulated in perturbation form (Non-Linear Disturbance Equations — NLDE) are solved only in a small region of the flow. They applied this method to stationary and pulsed channel, as well as to the flow over a turbine blade (a configuration conceptually similar to that shown in Figure 1.2). The turbulent fluctuations in their calculation were generated

by the natural amplification of acoustic perturbations and numerical errors in the adverse-pressure-gradient region on the suction side of the blade. The authors did not quantify how effective this amplification was (*i.e.*, what distance was required to develop a realistic turbulent flow).

Terracol [25] performed calculations of the flow over a flat-plate trailing edge with thickness comparable to the boundary layer thickness and a NACA0012 airfoil also using the NLDE method [24]. In the first configuration he compared various treatments of the RANS/LES interface: allowing the amplification of existing instabilities to develop (the method used in [24]), a recycling method [26, 102], and a synthetic reconstruction of the fluctuation field [27]. He found that, in this flow, the amplification of existing disturbances was not sufficient to establish a well-developed turbulent flow prior to the trailing edge, while the recycling resulted in correct turbulent statistics, but produced spurious peaks in the pressure spectrum; the synthetic reconstruction offered the best result, and gave reasonable pressure spectra in the NACA0012 case.

Schlüter *et al.* [39] presented results of the hybrid simulation of the flow in a gas turbine engine in which both the turbine and compressor were simulated by RANS while the combustor was computed using LES. The calculation was performed in separate stages: the outflow from the RANS solution of the compressor supplied inflow conditions for the LES, while the outflow of the LES was used to supply inlet conditions to the RANS calculation of the turbine. In order to generate turbulence

at the RANS/LES interface the authors used the results of a related investigation of inflow conditions for LES by Schlüter *et al.* [40].

Recently, Keating *et al.* [30] applied the controlled forcing method by Spille-Kohoff and Kaltenbach [49] coupled with the synthetic turbulent by Batten *et al.* [31] in a hybrid RANS/LES framework for the simulation of boundary layers in favorable and adverse pressure gradients, and found that it produced physically realistic turbulence in short distances. They also observe that the quality of the RANS data used affects the results significantly; this is true in particular in favorable and adverse-pressure-gradient boundary layers.

1.5 Plan of the present dissertation

The controlled forcing methods has shown very good performance to generate realistic eddies in a short distance. This method, moreover, can be used both in a zonal calculation, as an inflow condition and in a single-grid method, through forcing terms added to the momentum equations.

The purpose of this dissertation is to improve the controlled forcing method [49, 50, 30] by optimizing the controller parameters (which previously were assigned by trial-and-error) to shorten the transition region and the simulation transient, and also to explain their physical significance. The test cases used to evaluate the model will be a flat-plate boundary layer subjected to zero, adverse and favorable pressure gradients, and a three-dimensional boundary layer. An additional contribution of

this work was the study of the favorable pressure gradient boundary layer. This flow was initially computed as a test case for the hybrid calculations. The richness of the physics we encountered prompted us to look at this problem in additional depth.

In the following chapters we will first describe the methodology used, then discuss the controller function, and the optimization of its parameters. The result of four applications will be presented next, followed by conclusions and recommendations for future work. The following chapter will describe some results relating to the relaminarization and retransition of boundary layers subjected to strong acceleration. Finally, conclusions and recommendations for future work will be made.

Chapter 2

Problem formulation

2.1 Governing equations

The numerical methods used in this work is the same as [51] The reference system is cartesian with x or x_1 being the streamwise direction, y or x_2 the wall-normal direction, and z or x_3 the spanwise direction, and with velocity components u , v and w or u_1 , u_2 and u_3 respectively. The equations are in non-dimensional form, with the following definition:

$$\begin{aligned} x_i^* &= \frac{x_i}{L} & u_i^* &= \frac{u_i}{U_o} & t^* &= \frac{tU_o}{L} & p^* &= \frac{p}{\rho U_o^2} \\ \text{Re} &= \frac{LU_o}{\nu} \end{aligned}$$

where L and U_o are the reference length and velocity.

The non-dimensional equations can, therefore, be written as

$$\frac{\partial u_i}{\partial x_i} = 0 \tag{2.1}$$

$$\frac{\partial u_i}{\partial t} + \frac{\partial u_j u_i}{\partial x_j} = \frac{1}{\text{Re}} \frac{\partial^2 u_i}{\partial x_j \partial x_j} - \frac{\partial p}{\partial x_i} \tag{2.2}$$

where the $*$ is omitted. The large-eddy simulation equations are derived from the previous equation by applying a filtering operation, defined as

$$\bar{f}(x) = \int f(x') G(x, x'; \bar{\Delta}) dx' \tag{2.3}$$

where G is a filter function with a characteristic length, $\overline{\Delta}$. The filtering operation separates the turbulent motion into large and small scales. The filter functions used include the sharp Fourier cutoff filter, the Gaussian filter and the top-hat (or box) filter. Both the Fourier cutoff and Gaussian filter are defined in spectral space, while the top-hat filter is defined in physical space. As finite difference methods are used in the present work, it is computationally more efficient to use the top-hat filter, which is defined in physical space as

$$G(x) = \begin{cases} 1/\overline{\Delta} & \text{if } |x| \leq \overline{\Delta}/2 \\ 0 & \text{otherwise} \end{cases} \quad (2.4)$$

Applying the filter operator to the Navier-Stokes equation gives:

$$\frac{\partial \overline{u}_i}{\partial x_i} = 0 \quad (2.5)$$

$$\frac{\partial \overline{u}_i}{\partial t} + \frac{\partial \overline{u}_j \overline{u}_i}{\partial x_j} = \frac{1}{\text{Re}} \frac{\partial^2 \overline{u}_i}{\partial x_j \partial x_j} - \frac{\partial \overline{p}}{\partial x_i} - \frac{\partial \tau_{ij}}{\partial x_j} \quad (2.6)$$

where the subgrid-scale stress term, τ_{ij} is defined as

$$\tau_{ij} = \overline{u_i u_j} - \overline{u}_i \overline{u}_j \quad (2.7)$$

This term is unclosed and must be modelled. The closure of the subgrid-scale stress terms is known as subgrid-scale modelling. In this work we use an eddy-viscosity closure with dynamic determination of the coefficient. After describing the numerical technique used to solve the governing equations (2.6) and the SGS model employed, the final subsection details the averaging procedures required to remove the numerical instability arising from sharp fluctuations in the coefficients.

2.2 Numerical method and boundary conditions

The Navier-Stokes equations are integrated in time using a fractional step technique [62]. The wall-normal viscous and subgrid-scale diffusion terms are advanced implicitly using the Crank-Nicolson method. The other terms in the equations are advanced using a low-storage third-order Runge-Kutta scheme [61]. The three-step ($k = 1, 2, 3$) fractional steps, time advancement scheme is, therefore,

$$\widehat{u}_i - \beta_k \Delta t M(\widehat{u}_i) = r_i^{k-1} \quad (2.8)$$

$$\frac{\partial^2 (\delta p)}{\partial x_i \partial x_i} = \frac{1}{2\beta_k \Delta t} \frac{\partial \widehat{u}_i}{\partial x_i} \quad (2.9)$$

$$u_i^k = \widehat{u}_i - 2\beta_k \Delta t \frac{\partial (\delta p)}{\partial x_i} \quad (2.10)$$

$$p^k = p^{k-1} + \delta p \quad (2.11)$$

where the explicit terms, r_i^{k-1} , are

$$r_i^{k-1} = u_i^{k-1} + \Delta t \left(\beta_k M(u_i^{k-1}) + \gamma_k A(u_i^{k-1}) + \zeta_k A(u_i^{k-2}) - 2\beta_k \frac{\partial p^{k-1}}{\partial x_i} \right) \quad (2.12)$$

At the first substep, when $k = 1$, $u^{k-1} = u^n$, and at the end of the third substep, the solution is $u^{n+1} = u^k$. The coefficients of the time advancement scheme are

$$\beta_1 = 4/15 \quad \beta_2 = 1/15 \quad \beta_3 = 1/6 \quad (2.13)$$

$$\gamma_1 = 8/15 \quad \gamma_2 = 5/12 \quad \gamma_3 = 3/4 \quad (2.14)$$

$$\zeta_1 = 0 \quad \zeta_2 = -17/60 \quad \zeta_3 = -5/12 \quad (2.15)$$

This time advancement scheme is stable under the following conditions:

$$\alpha = \Delta t \left(\frac{u_i}{\Delta x_i} \right) < \sqrt{3} \quad (2.16)$$

where $i = 1, 2, 3$ and

$$\beta = \left(\frac{4}{\text{Re}} \frac{\Delta t}{\Delta x_i^2} \right) < \sqrt{3} \quad (2.17)$$

where $i = 1, 3$.

A second-order finite difference scheme is used for spatial discretisation of all terms [63]. While spectral methods are more accurate and less diffusive than finite difference schemes, they are more difficult to use in complex geometries. Moin and Mahesh [64] found that equivalent results to a spectral method can be obtained using a second-order finite difference method if the mesh is doubled in each direction. Higher-order, conservative finite difference schemes have been proposed [63]; however these have additional complications in the use of nonperiodic boundary conditions. A staggered grid [65] is used for its good conservation properties [63], its accuracy and to prevent the “odd-even” decoupling of pressure.

The following discrete differencing and averaging operators [63] are defined on the staggered grid:

$$\left. \frac{\delta_1 \phi}{\delta_1 x} \right|_i \equiv \frac{\phi_{i+1/2} - \phi_{i-1/2}}{x_{i+1/2} - x_{i-1/2}} \quad (2.18)$$

$$\left. \overline{\phi}^{1x} \right|_i \equiv \frac{\phi_{i+1/2} + \phi_{i-1/2}}{2} \quad (2.19)$$

These operators are then used to discretise the Navier-Stokes equations yielding

$$\frac{\delta_1 u_i}{\delta_1 x_i} = 0 \quad (2.20)$$

$$\frac{\delta_1 u_i}{\delta_1 t} + \frac{\delta_1 \overline{u_j^{1x_i}} \overline{u_i^{1x_j}}}{\delta_1 x_j} = \frac{1}{\text{Re}} \frac{\delta_1}{\delta_1 x_j} \left(\frac{\delta_1 u_j}{\delta_1 x_j} \right) - \frac{\delta_1 p}{\delta_1 x_i} - \frac{\delta_1 \tau_{ij}}{\delta_1 x_j} \quad (2.21)$$

The subgrid-scale coefficient is evaluated using the dynamic procedure at each timestep. The subgrid-scale eddy-viscosity, and the scale-similar contribution to the subgrid-scale stress is evaluated at every Runge-Kutta substep.

All the results are averaged in time for a long time period (at least 15 Large eddy turn over times) in order to have statistically steady quantities. The samples of turbulent quantities for each cases are recorded after the transient time is over.

Periodic boundary conditions are used in the spanwise direction, with no-slip boundaries at the solid wall, and convective conditions [82] used at the outflow. The freestream condition for the zero pressure gradient boundary layer and the 3D boundary layer [102],

$$\frac{\partial \bar{u}}{\partial y} = 0; \quad \bar{v} = U_\infty \frac{d\delta^*}{dx}; \quad \frac{\partial \bar{w}}{\partial y} = 0; \quad (2.22)$$

was used at the upper boundary, where δ^* is the boundary layer displacement thickness and U_∞ is the freestream velocity. We calculated $d\delta^*/dx$ using a linear regression on the calculated $\delta^*(x)$ distribution. In the case of favorable or adverse pressure-gradient boundary layer the U_∞ was assigned and the following expression were used:

$$\frac{\partial \bar{u}}{\partial y} = -\frac{\partial \bar{v}}{\partial x}; \quad \bar{v} = U_\infty \frac{d\delta^*}{dx} + (\delta^* - h) \frac{dU_\infty}{dx}; \quad \frac{\partial \bar{w}}{\partial y} = 0; \quad (2.23)$$

with h the higher of the domain. In the adverse pressure gradient boundary layer case, V_∞ was assigned. Other boundary condition are described with the specific cases in Chapter 4. When a derivative of a flow variable is required at a wall (*i.e.*,

for the wall-normal diffusion term), a three-point one-sided approximation is used [66]

The Poisson equation (2.9) resulting from the fractional step technique is solved using Fourier transforms in the spanwise directions followed by cyclic reduction, and a direct tridiagonal matrix inversion in the wall-normal direction. Neumann boundary conditions are used for no-slip walls.

The code is parallelized using Message Passing Interface (MPI). The computation is distributed between n processors (n was varied between 1 and 4 for all the simulations described in this dissertation).

2.3 Subgrid-scale modeling

The term τ_{ij} denotes the subgrid-scale (SGS) stress, which represent the coupling of small scales on the resolved turbulence. The closure of the subgrid-scale stress is known as subgrid-scale modeling. In the following subsection the eddy-viscosity closure is presented, and in the next subsection the dynamic modeling is described. Dynamic modeling removes the need for a priori specification of the model coefficient. In the last subsection the averaging procedure required to damp sharp fluctuations in the model parameters is presented.

2.3.1 Eddy-viscosity assumption

Eddy-viscosity subgrid-scale models relate the subgrid-scale stresses, τ_{ij} , to the large-scale (*i.e.*, resolved) strain rate tensor, $\overline{S}_{ij} = \frac{1}{2} \left(\frac{\partial u_i}{\partial x_j} + \frac{\partial u_j}{\partial x_i} \right)$, through a subgrid-scale eddy-viscosity, ν_t^{sgs} :

$$\tau_{ij} - \frac{\delta_{ij}}{3} \tau_{kk} = -2\nu_t^{\text{sgs}} \overline{S}_{ij} \quad (2.24)$$

The simplest eddy-viscosity subgrid-scale model is Smagorinsky's (1963), where the eddy viscosity is modeled as the product of a length scale (proportional to the filter width, $\overline{\Delta}$) and a velocity difference at that scale (proportional to $\overline{\Delta}|\overline{S}|$, where $|\overline{S}| = (2\overline{S}_{ij}\overline{S}_{ij})^{1/2}$). A constant, C_s , is included, giving the following model for the subgrid-scale eddy viscosity:

$$\nu_t^{\text{sgs}} = C_s^2 \overline{\Delta}^2 |\overline{S}| \quad (2.25)$$

The Smagorinsky constant must be evaluated in order to apply the model. In isotropic turbulence, if the filter width is in the inertial subrange, the constant takes values between $C_s = 0.179$ and $C_s = 0.23$ [52]. However in the presence of shear, near solid boundaries or near transition this value needs to be decreased. Methods such as van Driest near-wall damping [53] and intermittency factors [54] have also been used.

Eddy-viscosity models can represent the dissipative effects of the small scales accurately. However, they fail to reproduce the local stresses with adequate accuracy. A priori studies comparing the actual subgrid-scale stresses calculated using DNS

and those calculated using an eddy-viscosity subgrid-scale model show a correlation coefficient of between 0 and 0.25 [55, 56].

2.3.2 The dynamic procedure

Dynamic models evaluate the subgrid-scale model coefficient from information contained in the resolved-flow field of a large eddy simulation. In this way the dynamic of the smallest resolved scales are implicitly assumed similar to the dynamic of the subgrid scale. The advantages of the dynamic model are that is not necessary to tune any constant for different flow field problem, that the subgrid scale stress vanish in a laminar flow and at a solid boundary, and that they have the correct asymptotic behavior in the near wall region of a turbulent boundary layer. Thus the introduction of the dynamic procedure by Germano *et al.* [100] resolved one of the major difficulties in using subgrid-scale models – the need for *a priori* input of model coefficients. Using the dynamic procedure, the coefficients in the model are determined during the calculation and are based on the energy content of the smallest resolved scales.

A test filter is defined with a width, $\widehat{\Delta}$, larger than the grid filter width, $\overline{\Delta}$. The calculation of the coefficients in the model is based on the Germano identity [100] :

$$\mathcal{L}_{ij} = T_{ij} - \widehat{\tau}_{ij} \quad (2.26)$$

which relates the resolved turbulent stresses, \mathcal{L}_{ij} ,

$$\mathcal{L}_{ij} = \widehat{\overline{u_i u_j}} - \widehat{\overline{u_i}} \widehat{\overline{u_j}} \quad (2.27)$$

to the subgrid-scale stresses, τ_{ij} , (equation (2.5)) and the subtest stresses, T_{ij} ,

$$T_{ij} = \widehat{\overline{u_i u_j}} - \widehat{\overline{u_i}} \widehat{\overline{u_j}} \quad (2.28)$$

If an eddy-viscosity model is used to parameterize the subgrid-scale and subtest stresses,

$$\tau_{ij} = -2C_{ev} \overline{\Delta}^2 |\overline{S}| \overline{S}_{ij} \quad (2.29)$$

$$T_{ij} = -2C_{ev} \widehat{\Delta}^2 |\widehat{S}| \widehat{S}_{ij} \quad (2.30)$$

then Germano's identity (2.26) yields the following equation for C_{ev} :

$$C_{ev} M_{ij} = \mathcal{L}_{ij} \quad (2.31)$$

where

$$M_{ij} = -a^2 \overline{\Delta}^2 |\widehat{S}| \widehat{S}_{ij} + \overline{\Delta}^2 |\overline{S}| \overline{S}_{ij} \quad (2.32)$$

and $a = \widehat{\Delta}/\overline{\Delta}$ is the ratio of the test filter width to the grid filter width.

As equation(2.31) has a single coefficient and five independent equations, the system is overdetermined. Lilly [60] proposed a least-squares minimization of the error, giving the following equation for determining the coefficient:

$$C_{ev} = -\frac{1}{2} \frac{\langle \mathcal{L}_{ij} M_{ij} \rangle}{\langle M_{ij} M_{ij} \rangle} \quad (2.33)$$

where $\langle \cdot \rangle$ is an appropriate average.

2.3.3 Averaging of the eddy-viscosity coefficient

The averaging in the dynamic procedure is required to remove the very sharp fluctuations in the coefficient which can lead to significant errors, not to mention numerical instability. These sharp fluctuations are caused by a mathematical inconsistency in the expression for C_s in the dynamic procedure. Meneveau *et al.* [80] proposed averaging along pathlines in order to reduce the noise. To have Galilean invariance, the time average have to be performed by following fluid particles of the flow. This average method is known as the Lagrangian dynamic model, allowing for averaging in inhomogeneous flows in complex geometries. Here, the average is defined as

$$\langle f \rangle = \mathcal{I}_f = \int_{-\infty}^t f(t') W(t - t') dt' \quad (2.34)$$

where the integral is carried out following a flow pathline, and $W(t)$ is a weighting function. These are then used to replace the averages in the calculation for the coefficient. For example, in the dynamic eddy-viscosity model,

$$C_s = -\frac{1}{2} \frac{\langle \mathcal{L}_{ij} M_{ij} \rangle}{\langle M_{ij} M_{ij} \rangle} = -\frac{1}{2} \frac{\mathcal{I}_{LM}}{\mathcal{I}_{MM}} \quad (2.35)$$

where

$$\mathcal{I}_{LM} = \int_{-\infty}^t \mathcal{L}_{ij}(t') M_{ij}(t') W(t - t') dt' \quad (2.36)$$

$$\mathcal{I}_{MM} = \int_{-\infty}^t M_{ij}(t') M_{ij}(t') W(t - t') dt' \quad (2.37)$$

An exponential weighting function is usually chosen [80]:

$$W(t) = T^{-1} \exp(-t/T) \quad (2.38)$$

where the time scale, T , controls the memory length of the Lagrangian averaging and here is set to

$$T = 1.5\bar{\Delta} \times (-8\mathcal{I}_{LM}\mathcal{I}_{MM})^{-1/8} \quad (2.39)$$

As an exponential weighting function is used, \mathcal{I}_{LM} and \mathcal{I}_{MM} are actually solutions to relaxation-transport equations. Meneveau *et al.* [80] suggests that the computational cost of the solution of the two additional transport equations can be reduced by approximating them as

$$\mathcal{I}_{LM}^{n+1}(x) = H\{\epsilon\mathcal{L}_{ij}^{n+1}M_{ij}^{n+1} + (1 - \epsilon)\mathcal{I}_{LM}^n(x - \bar{u}^n\Delta t)\} \quad (2.40)$$

$$\mathcal{I}_{MM}^{n+1}(x) = H\{\epsilon M_{ij}^{n+1}M_{ij}^{n+1} + (1 - \epsilon)\mathcal{I}_{MM}^n(x - \bar{u}^n\Delta t)\} \quad (2.41)$$

where $H\{\cdot\}$ is the ramp function ($H\{x\} = x$ if $x \geq 0$, and zero otherwise) and

$$\epsilon = \frac{\Delta t/T}{1 + \Delta t/T} \quad (2.42)$$

Linear interpolation is used to evaluate the integrals at the position $x - \bar{u}^n\Delta t$. A thorough analysis of the Lagrangian averaging procedure is given in Meneveau *et al.* [80].

2.3.4 Filtering operations

In the present study, filtering of the large-scale governing equations is implicitly defined by the second-order finite differences on the numerical grid. Explicit filtering is performed at test filter level (for the dynamic method). Second-order top-hat

filters were used and were calculated using

$$\bar{f}_i = f_i + \frac{h_f^2}{24} \frac{\delta^2 f}{\delta x^2} = f_i + \frac{h_f^2}{24} \left(\frac{f_{i-1} - 2f_i + f_{i+1}}{h^2} \right) \quad (2.43)$$

where h is the grid width and h_f is the filter width. This yields the well known Simpson's rule and trapezoidal rule filters with filter widths of $h_f/h = 2$ and $\sqrt{6}$ respectively. Trapezoidal rule filters were used in this work, comprising a test filter, \hat{f} , of width $\sqrt{6}\Delta$, where Δ is defined as geometric mean in each direction's filter width:

$$\hat{f}_i = \frac{1}{4} (f_{i-1} + 2f_i + f_{i+1}) \quad (2.44)$$

and a grid filter, \bar{f} , of width $\sqrt{3}\Delta$:

$$\bar{f}_i = \frac{1}{8} (f_{i-1} + 6f_i + f_{i+1}) \quad (2.45)$$

Trapezoidal rule filters were selected over Simpson's rule based filters due to slightly improved results in LES of turbulent channel flow using the dynamic mixed model.

2.4 RANS equations and Reynolds stress modeling

The equation for the RANS model are formally identical to the (2.6) where the term τ_{ij}

$$\tau_{ij} = \overline{u_i u_j} - \bar{u}_i \bar{u}_j \quad (2.46)$$

are defined as the Reynolds stresses and must be modeled. In this dissertation an eddy-viscosity model is used to close the equations (2.6):

$$\tau_{ij} - \frac{\delta_{ij}}{3} \tau_{kk} = -2\nu_t \bar{S}_{ij} \quad (2.47)$$

with ν_t evaluated through the one equation Spalart-Allmaras model [70], or through a two equations $k - \epsilon$ model. In this section, the two basic models will be shown: the Spalart-Allmaras [70] model and the two-layer $k - \epsilon$ model [71, 72].

2.4.1 Spalart-Allmaras model

The Spalart-Allmaras model relies directly on a transport equation for the turbulent viscosity. The form of this model leads to the following equations:

$$\begin{aligned} \frac{\partial \nu^*}{\partial t} + \vec{u} \cdot \nabla (\nu^*) &= c_{b1} (1 - f_{t2}) S^* \nu^* + \frac{1}{\sigma} (\nabla \cdot (\nu + \nu^*) \nabla \nu^*) \\ &+ c_{b2} (\nabla \nu^*)^2 - \left(c_{w1} f_w - \frac{c_b^2}{\kappa} f_{t2} \right) \left(\frac{\nu^*}{d} \right)^2 + f_{t1} D u^2 \end{aligned} \quad (2.48)$$

The turbulent viscosity μ_t is computed from

$$\mu_t = \rho \nu^* f_{v1} \quad (2.49)$$

$$f_{v1} = \frac{\chi^3}{\chi^3 + C_{v1}^3} \quad (2.50)$$

$$\chi = \frac{\nu^*}{\nu} \quad (2.51)$$

where the modified viscosity ν^* equals ν_t away from the wall. The damping function f_{v1} is based on the well know logarithmic law of the wall and lets ν_t go smoothly to zero near the wall.

S^* is related to the modified magnitude of the vorticity:

$$S^* = |S| + \frac{\nu^*}{\kappa^2 d^2} f_{v2} \quad (2.52)$$

$$f_{v2} = 1 - \frac{\chi}{1 + \chi f_{v1}} \quad (2.53)$$

where $|S|$ is the magnitude of the vorticity and d the distance to the closest wall. The function f_{v2} is built as f_{v1} on the hypothesis of a classical logarithmic-layer behaviour. κ is the von Karman constant 0.41.

The function f_w recovers the decay of the destruction term in the outer layer and produces a realistic skin-friction coefficient:

$$f_w = g \left(\frac{1 + c_{w3}^6}{g^6 + c_{w3}^6} \right)^{\frac{1}{6}} \quad (2.54)$$

$$g = r + c_{w2} (r^6 - r) \quad (2.55)$$

$$r = \frac{\nu^*}{S^* \kappa^2 d^2} \quad (2.56)$$

The function f_{t1} and f_{t2} makes it possible to prescribe transition to turbulence:

$$f_{t1} = c_{t1} g_t e^{-c_{t2} \frac{\omega_t^2}{Du^2} (d^2 + g_t^2 d_t^2)} \quad (2.57)$$

$$f_{t2} = c_{t3} e^{-c_{t4} \chi^2} \quad (2.58)$$

where d_t is the distance between the current point and the transition to turbulence point, ω_t is the wall vorticity at the transition point, Du is the difference between the velocity at the current point and that at the transition point, and g_t is

$$g_t = \min \left(0.1, \frac{Du}{\omega_t \Delta x_t} \right) \quad (2.59)$$

where Δx_t is the grid spacing along the wall at the transition point. The model constants have the following default values: $c_{b1} = 0.1355$, $c_{b2} = 0.622$, $\sigma = 0.6667$, $c_{v1} = 7.1$, $c_{w1} = \frac{c_{b1}}{\kappa} + \frac{1+c_{b2}}{\sigma}$, $c_{w2} = 0.3$, $c_{w3} = 2.0$.

2.4.2 $k - \epsilon$ model

We tested the two-layer $k - \epsilon$ model [71, 72] where in the outer layer, the standard $k - \epsilon$ model is used; the equations for k and ϵ in this case are:

$$\frac{\partial k}{\partial t} + \nabla \cdot (\vec{u}k) = \nabla \cdot \left(\nu + \frac{\nu_t}{\sigma_k} \right) \nabla k + P_k - \epsilon \quad (2.60)$$

and for its dissipation rate ϵ is

$$\frac{\partial \epsilon}{\partial t} + \nabla \cdot (\vec{u}\epsilon) = \nabla \cdot \left(\nu + \frac{\nu_t}{\sigma_\epsilon} \right) \nabla \epsilon + C_{\epsilon 1} f_{\epsilon 1} \frac{\epsilon}{k} P_k - C_{\epsilon 2} f_{\epsilon 2} \frac{\epsilon^2}{k}, \quad (2.61)$$

with the term P_k , the production of turbulent energy, defined as

$$P_k = \langle u_i u_j \rangle \frac{\partial u_i}{\partial x_j}. \quad (2.62)$$

and the turbulent viscosity:

$$\nu_t = C_\mu f_\mu \frac{k^2}{\epsilon}, \quad (2.63)$$

with

$$f_\mu = e^{-2.5/(1+R_t/50)} \quad (2.64)$$

$$f_{\epsilon 1} = 1.0 \quad (2.65)$$

$$f_{\epsilon 2} = 1 - 0.3e^{-R_t^2} \quad (2.66)$$

as given function of the turbulent Reynolds number

$$Re_t = \frac{k^2}{\nu \epsilon} \quad (2.67)$$

and $C_\mu = 0.09$, $C_{\epsilon 1} = 1.55$, $C_{\epsilon 2} = 2$, $\sigma_k = 1$, $\sigma_\epsilon = 1.3$

In the inner-layer, the eddy viscosity is computed using

$$\nu_{t,inner} = C_\mu \ell_\mu \sqrt{k} \quad (2.68)$$

where the length scale, ℓ_μ is given by

$$\ell_\mu = y c_\ell \left(1 - e^{-Re_y/A_\mu}\right), \quad Re_y = \frac{y\sqrt{k}}{\nu} \quad (2.69)$$

where y is the distance to the nearest wall and $A_\mu = 70$, $c_\ell = \kappa C_\mu^{-3/4}$.

The eddy viscosity is obtained by combining the inner- and outer-layer eddy viscosities through a blending function, λ_ϵ , which uses a hyperbolic tangent to vary smoothly from 0 to 1:

$$\nu_t = \lambda_\epsilon \nu_{t,outer} + (1 - \lambda_\epsilon) \nu_{t,inner}; \quad (2.70)$$

$$\lambda_\epsilon = \frac{1}{2} \left[1 + \tanh \left(\frac{Re_y - 200}{0.1 Re_y / \tanh(0.98)} \right) \right]. \quad (2.71)$$

2.5 Synthetic turbulence generation

The synthetic turbulence generation method of Batten *et al.* [31] is used to create a three-dimensional, unsteady velocity field at the inflow plane of the LES region. The Batten method is easy to implement numerically and takes into account the anisotropy of the flow with a very simple solution that will be explained in the following. An intermediate velocity, v_i is first constructed, using a sum of sines and cosines with random phases and amplitudes:

$$v_i(x_j, t) = \sqrt{\frac{2}{N}} \sum_{n=1}^N \left[p_i^n \cos \left(\widehat{d}_j^n \widehat{x}_j^n + \omega^n \widehat{t} \right) + q_i^n \sin \left(\widehat{d}_j^n \widehat{x}_j^n + \omega^n \widehat{t} \right) \right], \quad (2.72)$$

where

$$\hat{x}_j = 2\pi x_j / L_b, \quad \hat{t} = 2\pi t / \tau_b, \quad (2.73)$$

are spatial coordinates normalized by the length- and time-scale of the turbulence. In the above, $\tau_b = k/\varepsilon$ and $L_b = \tau_b V_b$ are the turbulence time- and length-scales, and $V_b = k^{1/2}$ is the velocity scale. The random frequencies $\omega^n = N(1, 1)$ are taken from a normal distribution $N(\mu, \sigma^2)$ with mean $\mu = 1$ and variance $\sigma^2 = 1$. The amplitudes are given by

$$p_i^n = \epsilon_{ijk} \zeta_j^n d_k^n, \quad q_i^n = \epsilon_{ijk} \xi_j^n d_k^n \quad (2.74)$$

where $\zeta_i^n, \xi_i^n = N(0, 1)$, and

$$\hat{d}_j^n = d_j^n \frac{V}{c^n}. \quad (2.75)$$

are modified wavenumbers obtained by multiplying the wavenumbers, d_i^n , by the ratio of the velocity scale $V_b = L_b/\tau_b$ to c^n , given by

$$c^n = \sqrt{\frac{3}{2} \langle u'_l u'_m \rangle \frac{d_l^n d_m^n}{d_k^n d_k^n}}. \quad (2.76)$$

The wave-numbers $d_i^n = N(0, 1/2)$ are chosen from a normal distribution with variance $1/2$, resulting in a three-dimensional spectrum that behaves like $d^4 \exp(-d^2)$. Although the wave-numbers d_i^n are distributed isotropically in a sphere, dividing them by c^n tends to elongate those wave-numbers that are most closely aligned with the largest component of the Reynolds-stress tensor, and contract those aligned with the smaller ones. This results in a more physically realistic spectrum of turbulence,

with eddies that (near the walls) are more elongated in x , and tend to be more spherical in the channel center.

The synthetic turbulent fluctuation field is finally reconstructed by a tensor scaling:

$$u'_i = a_{ik} v_k \quad (2.77)$$

where a_{ik} is the Cholesky decomposition of the Reynolds-stress tensor.

To better understand the effects of the decomposition (2.2) in the generation of synthetic turbulence, it can be written as:

$$v_i(x_j, t) = \left(\frac{2}{N}\right)^{\frac{1}{2}} \sum_{n=1}^N \Re \left[(p_i^n - j q_i^n) \left(\cos(\widehat{d_j^n x_j^n} + \omega^n \widehat{t}) + j \sin(\widehat{d_j^n x_j^n} + \omega^n \widehat{t}) \right) \right] \quad (2.78)$$

where \Re is the real part and j is the imaginary unit. From (2.78) we obtain

$$v_i(x_j, t) = \left(\frac{2}{N}\right)^{\frac{1}{2}} \sum_{n=1}^N \Re \left[(p_i^n - j q_i^n) e^{j(\widehat{d_j^n x_j^n} + \omega^n \widehat{t})} \right]; \quad (2.79)$$

expanding the exponential in Taylor series gives

$$v_i(x_j, t) = \left(\frac{2}{N}\right)^{\frac{1}{2}} \sum_{n=1}^N \Re \left[(p_i^n - j q_i^n) \left(1 + \sum_{m=1}^{\infty} j^m \frac{(\widehat{d_j^n x_j^n} + \omega^n \widehat{t})^m}{m} \right) \right] \quad (2.80)$$

where

$$(\widehat{d_j^n x_j^n} + \omega^n \widehat{t}) = \left(\widehat{d_j^n} \frac{2\pi x_j}{L_b} + \widehat{\omega^n} \frac{2\pi t}{\tau_b} \right) = \left(\widehat{d_j^n} \frac{2\pi x_j}{\tau_b \sqrt{k}} + \widehat{\omega^n} \frac{2\pi t}{\tau_b} \right) \quad (2.81)$$

with $\tau_b = k/\epsilon$. The wavenumber and frequency modulation depends on the time scale τ_b that is large near the wall and small far from it. As we can see from (2.80), the in-phase and in-quadrature decomposition (2.2) has all the powers of

$(\widehat{d_j^n x_j^n} + \omega^n \widehat{t})$. This results in an energetic non linear modulation (in wave-number and frequency) that spreads the energy of the signal on to a broad spectrum. Far from the wall, however, $\tau_b = k/\epsilon$ is large with respect to its value near the wall, so that in (2.80) we can neglect the non linear term, resulting in a smooth linear modulation (uniform distribution of the wave number) of the signal energy. In this way, the spectra module of the turbulence is mimicked by the decomposition (2.2).

Figure 2.1 shows the distribution of the wavenumbers d_i^n and modified wavenumber $\frac{d_i^n}{c^n}$ for different distances from the wall. It is clear that far from the wall the distribution of the modified wavenumber becomes more isotropic in space.

The result of the synthetic fluctuation produced by the Batten's decomposition (2.2) for different distance from the wall is shown in Figure 2.2. It is evident that close to the wall the structure are strongly anisotropy, stretched in the direction of the larger Reynolds stress. Far from the wall, on the other hand, the distribution becomes more isotropic.

In the present work either the Spalart-Allmaras (S-A) or $k - \epsilon$ model [71, 72] is used in the RANS section of the domain. From one of the two models the time scale and Reynolds stresses for the synthetic turbulence generation are computed. The Spalart-Allmaras model gives the averaged flow field, and the turbulent viscosity ν_t , while the $k - \epsilon$ model gives the turbulent kinetic energy k , and the dissipation rate ϵ other than the averaged field, of course. From the $k - \epsilon$ model we have:

$$\nu_t = \rho C_\mu k^2 / \epsilon \quad (2.82)$$

where $C_\mu = 0.09$; therefore, the Reynolds shear stress $\langle u'v' \rangle$ are:

$$-\langle u'v' \rangle = \nu_t \frac{\partial u}{\partial y} \quad (2.83)$$

and the normal Reynold stresses are assumed to be equal:

$$\langle u'u' \rangle = \langle v'v' \rangle = \langle w'w' \rangle = \frac{2}{3}k. \quad (2.84)$$

Therefore, the wavenumbers used in the present hybrid RANS/LES formulation are also isotropic. The time-scale for the generation of synthetic turbulence is the ratio of k over ϵ :

$$\tau_b = \frac{k}{\epsilon} \quad (2.85)$$

If the Spalart-Allmaras model is used, to relate the TKE, k , to the Reynolds shear stress, $\langle u'v' \rangle$, we use the experimental result [73, 74]

$$| -\langle u'v' \rangle | = \nu_t \left| \frac{\partial u}{\partial y} \right| = a_1 k \quad (2.86)$$

where $a_1 = \sqrt{C_\mu}$ and C_μ is typically 0.09 as in the previous case. The normal Reynolds stresses are evaluated as in the S-A model, and for the time-scale, we use the definition of eddy-viscosity from the $k - \epsilon$ turbulence model to express ϵ in terms of k and ν_t [75]:

$$\epsilon = c_\mu k^2 / \nu_t \quad . \quad (2.87)$$

so the time scale

$$\tau_b = \frac{k}{\epsilon} = \frac{1}{\sqrt{C_\mu} \left| \frac{\partial U}{\partial y} \right|} \quad (2.88)$$

In the simulations presented here, the number of modes, N , used to generate the synthetic field was 200. This number was required to ensure that the resulting statistics were independent of the number of modes used. Further details of the method can be found in [31].

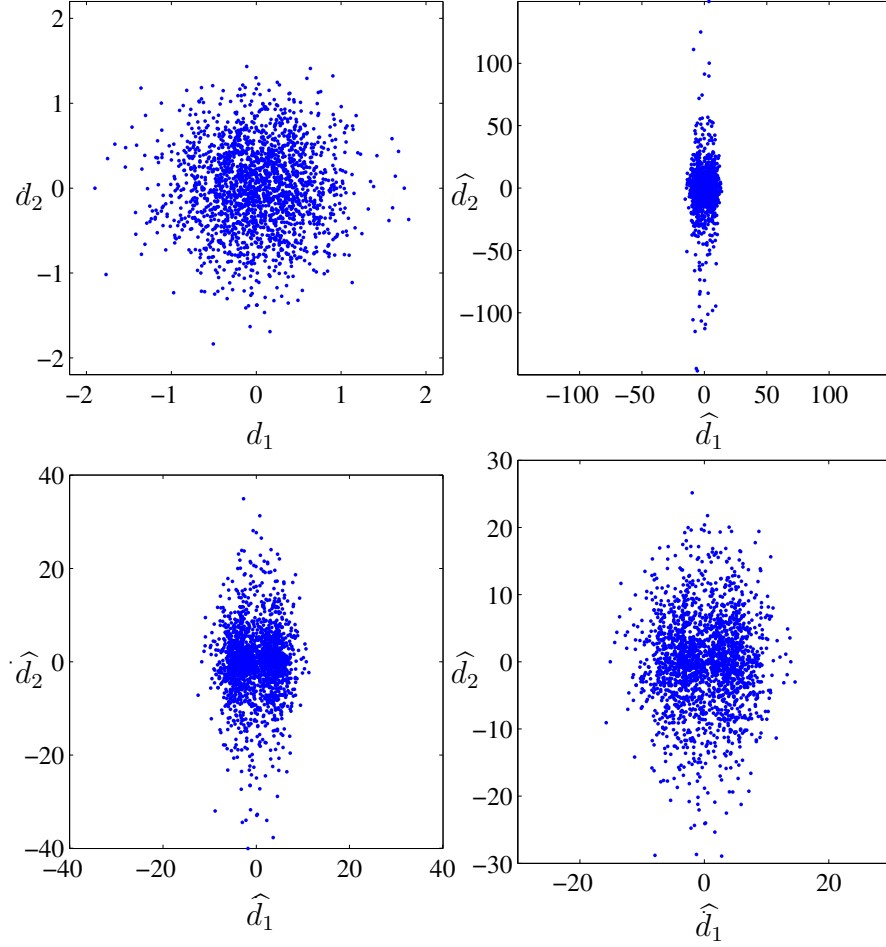


Figure 2.1: Distribution of the wavenumbers d_i^n (top right) and modified wavenumbers $\frac{d_i^n}{c^n}$ for different distances from the wall: top right figure is for $y^+ = 12$, bottom left is $y^+ = 100$, and bottom right is $\frac{y}{\delta^*} = 5$

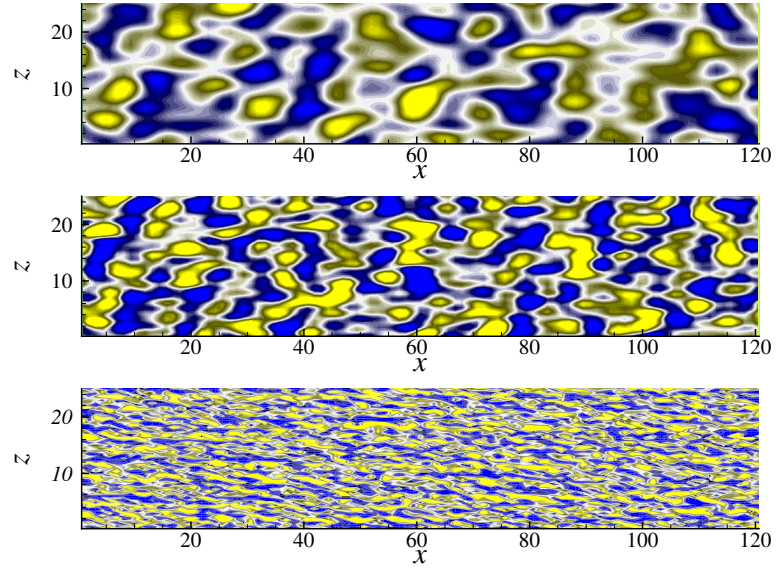


Figure 2.2: Synthetic fluctuation produced by the Batten's decomposition for different distance from the wall: bottom figure is for $y^+ = 12$, central is $y^+ = 100$, and top is $\frac{y}{\delta^*} = 5$. The distance are based on a LES calculation from which the Batten decomposition is evaluated.

Chapter 3

The controlled forcing method and its tuning

3.1 Introduction

The controlled forcing method for the turbulence generation consists of two parts: a method to generate synthetic turbulence at the inflow (the method by Batten *et al.* [31] is used here) and the addition of a forcing term to the wall-normal momentum equation that amplifies the velocity fluctuations in that direction, thus enhancing the production term in the shear-stress budget. The forcing amplitude is determined by a PI controller, which has two components acting in concert: a proportional part and an integral one; the two outputs are added together to form the actuating signal of the system to control, the Navier-Stokes equation system.

PI controllers give a robust performance over a wide range of operating conditions and are widely used due to their easy implementation. They are frequently used when the mathematical model of the system to control is complex or unavailable. Typically, the PI tuning for complex systems is based on semiempirical rules which have been proven in practice (for example the Cohen Coon tuning method [76] when a first-order approximation of the system to control is available). In other cases, for unknown non-linear system for instance, the primary target in the PI tun-

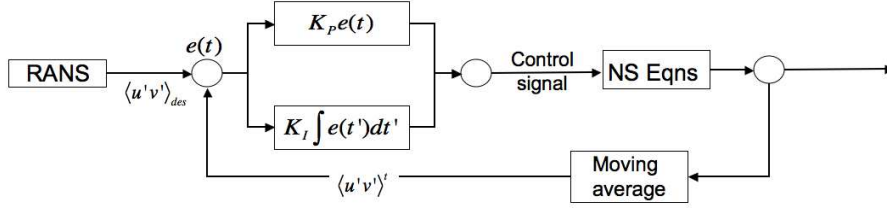


Figure 3.1: Block diagram of the PI controller.

ing is the stabilization of the controlled system and, marginally, the steady state performances (*e.g.*, minimize the steady state error).

In the controlled-forcing method, the system to control is the filtered NS equation system with a dynamic subgrid model. The desired output is the time-averaged Reynolds shear stress, generally obtained from the RANS solution. The output of the system is the instantaneous $u'v'$ correlation; an exponentially weighted moving-average filter is added to obtain smooth Reynolds stresses. The block diagram of the resulting system is shown in Figure 3.1.

First of all, we describe how the PI controller works in the closed-loop system using the schematic in Figure 3.1. The variable $e(t)$, the difference between the desired output $\langle u'v' \rangle^{des}$ and the actual output $\langle u'v' \rangle^t$, is sent to the PI that computes the integral of the error. The output of the PI (the control signal) is equal to K_P times the magnitude of the error, plus K_I times the integral of the error. The control signal is sent to the system to control, and a new output $u'v'$ is obtained. The new output is sent back (through the moving average filter) to obtain the new

error signal $e(t)$. This process goes on and on. The error is defined as

$$e(y, z, t) = \langle u'v' \rangle^{des}(x_o, y) - \langle u'v' \rangle^t(x_o, y, z, t) \quad (3.1)$$

where $\langle u'v' \rangle^{des}(x_o, y)$ is the target Reynolds shear stress at the control plane $x = x_o$, which is obtained from the RANS solution, and $\langle u'v' \rangle^t(x_o, y, z, t)$ is the Reynolds shear stress or production, averaged over some time interval. The magnitude of the forcing is set to

$$f(x_o, y, z, t) = r(y, z, t) [u(x_o, y, z, t) - \langle u \rangle^t(x_o, y, z, t)] \quad (3.2)$$

where

$$r(t) = K_P e(t) + K_I \int e(t') dt' \quad (3.3)$$

is the output of the PI controller. The significance and optimal values of the two constants, K_P and K_I , will be discussed later. The forcing so defined is added to the y -momentum equation. Enhancing the v' fluctuations through events with large u' [the term in square brackets in (3.2)] has the effect of accelerating the production of either Reynolds shear stress or the production of turbulent kinetic energy (TKE). The error is evaluated and forcing is performed at several planes within a few integral scales of the inflow (see below).

In the next section we will analyze and the time-averaging window filter to relate it to local time scales of the flow. Then, the PI controller will be tuned in order to have stable results and minimize the error in a short distance downstream the controlled region.

3.2 Analysis of the controller parameters

The controller described above has three parameters: the constants K_P and K_I and the width T_{ave} of the averaging window used to obtain $\langle u'v' \rangle^t$. In past applications [49, 50, 30] no investigation was carried out in which they were systematically varied. In this section we examine the transient and steady-state responses of the flow to these parameters, and relate them to physical properties of the flow. The target is to choose them to obtain statistically steady-state Reynolds stresses that match the desired ones in a short distance without destabilizing the Navier-Stokes equation system. While we cannot claim that to have found true optimal values of these parameters, we will call as “optimal” the value that gives realistic turbulence in the shortest distance, and with the shortest transient. In the next subsection it is presented the test case where the controller will be tuned.

3.2.1 Testing strategy: ZPG boundary layer

We test the PI controller in a flat-plate, zero-pressure-gradient (ZPG) boundary layer. In general the strategy to implement a RANS/LES calculation is the following (see Figure 5.1): first we perform a reference LES of the entire domain of interest; then we perform a RANS calculation of the equilibrium region, and use the RANS statistics to assign the inflow of the LES. Comparisons between the hybrid RANS/LES and the reference calculation allow us to evaluate the effectiveness of the method. However, to test the PI control we will perform an LES calculation

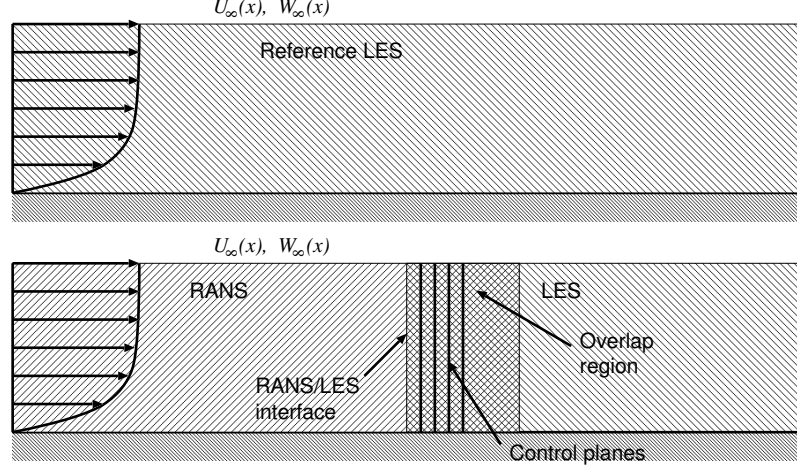


Figure 3.2: Sketch of the geometric configuration.

instead of a RANS calculation: first, we carried out the reference LES on a domain $240\delta_o^* \times 25\delta_o^* \times 25\delta_o^*$ in the streamwise, wall-normal and spanwise directions, respectively; here δ_o^* is the displacement thickness at the inflow. From this calculation, the time average Reynolds stress and the turbulence scales were extracted at $x/\delta_o^* = 80$. At this section a LES of dimension $120\delta_o^* \times 25\delta_o^* \times 25\delta_o^*$ with the synthetic turbulence generation and the controlled forcing at the inflow began; in this way it was possible to analyze the effect of the K_I , K_P and T_{ave} parameters without the influence introduced by a RANS model. The control planes were distributed over a length of $27.5\delta_o^*$ downstream of the inflow of the LES domain, with a spacing between planes of one boundary-layer thickness to allow the flow to re-adjust after the forcing (test calculations in which the forcing was distributed continuously were also carried out, with no significant differences). The inflow Reynolds number (based on freestream velocity U_o and displacement thickness) was $Re_\delta^* = 1000$. The grid spacings in the

streamwise and spanwise directions were $\Delta x/\delta_o^* = 1.25$ and $\Delta z/\delta_o^* = 0.385$, while 64 points were used in the wall-normal direction (with $y_{\min}^+ \approx 1.0$). The recycling and rescaling method of Lund [102] was used as inflow boundary condition for the reference LES.

3.2.2 The moving-average exponential window

We begin by discussing the moving-average (MA) filter. In the classical terminology used in the feedback control theory, this block is called “Measuring Device”; the output of the NS equations are the three instantaneous velocity fluctuations u'_i , which are the inputs to the MA block. Its output is an appropriate time-averaged Reynolds stress that can be compared to the result of the RANS. We use an exponentially weighted moving-average filter, which places more emphasis on the most recent data available. At time-step k we use the following expression:

$$\langle x_k \rangle = \left(1 - \frac{\Delta t}{T_{ave}}\right) \langle x_{k-1} \rangle + \frac{\Delta t}{T_{ave}} x_k \quad (3.4)$$

Δt is the time-step, and x is the data to average.

As new data is accumulated, the contribution of the oldest data decreases. The value of $\Delta t/T_{ave}$ determines the memory of the filter. We define an attenuation time T_d as the time after which the contribution of the signal at some time to the averaged data is negligible (say, 5% of the original contribution). It is easy to show

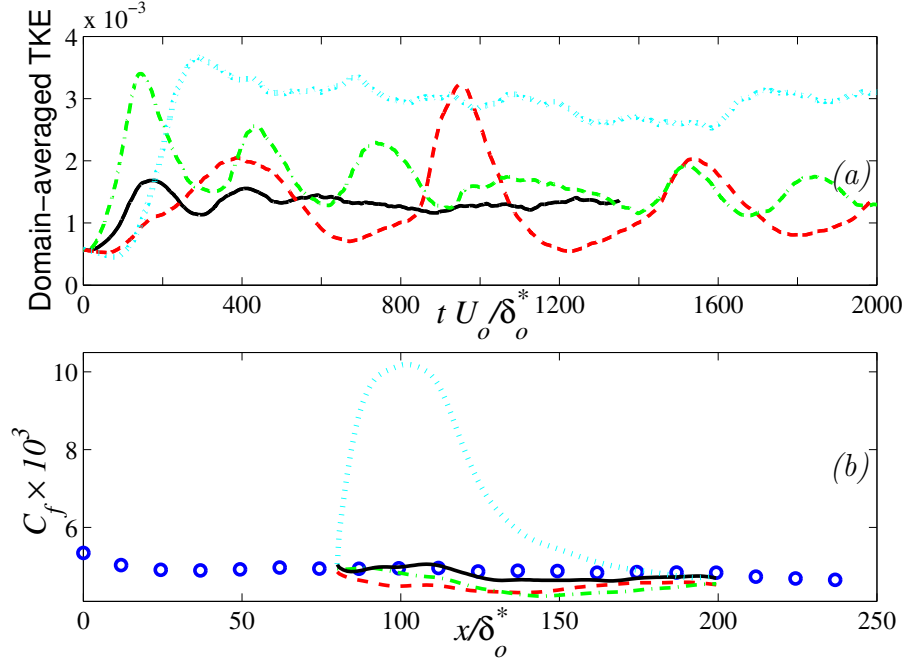


Figure 3.3: (a) Domain-averaged turbulent kinetic energy for $\cdots T_{ave} = 1, K_I = 5, K_P = 30$; $\text{—} T_{ave} = 10, K_I = 5, K_P = 30$; $-\text{--} T_{ave} = 100, K_I = 1, K_P = 1$; $-\cdot-\cdot T_{ave} = 100, K_I = 5, K_P = 30$. (b) C_f for the reference LES (\circ) and the cases shown in (a).

that, in this case,

$$\frac{T_d}{T_{ave}} = \frac{\Delta t}{T_{ave}} \frac{\log 0.05}{\log \left(1 - \frac{\Delta t}{T_{ave}}\right)} \quad (3.5)$$

since $1 \gg \Delta t/T_{ave}$, (3.5) gives $T_{ave} \simeq T_d/3$. We expect that T_d should be of the order of a large-eddy turnover time (LETOT) δ^*/u_τ , which results in $T_{ave} \simeq 10$ in the present calculation. Values much larger than this result in long transients, as the error affects the input to the forcing for a long time, and the forcing does not adjust rapidly enough to the present flow conditions, but is strongly affected by past events. This is shown in Figure 3.3(a) where the domain-averaged turbulent kinetic energy (TKE) is plotted as a function of time; in all the calculations we used the optimal values of K_P and K_I , except for one case in which we employed the values used in [50, 30], that is $K_P = K_I = 1$. A longer transient can be observed in the case $T_{ave} = 100$ compared with $T_{ave} = 10$. With the lower values of K_P and K_I used in early applications of this method the transient is still quite long, the magnitude of the oscillations is significant, and reasonable flow statistics require very long averaging times. An optimal choice of K_P and K_I , on the other hand, reduces the amplitude of the fluctuations, so that even an incorrect value of T_{ave} is less damaging. A low value of T_{ave} results in incorrect prediction of the flow: since the short averaging gives values of $\langle u'v' \rangle^t$ that are too far from a stationary sample, and thus may result in excessive forcing even if the flow has reached a realistic state.

In Figure 3.3(b) the skin-friction coefficient $C_f = 2\tau_w/\rho U_\infty^2$ (where τ_w is the wall stress) is shown for the same two cases, and it appears that the steady state

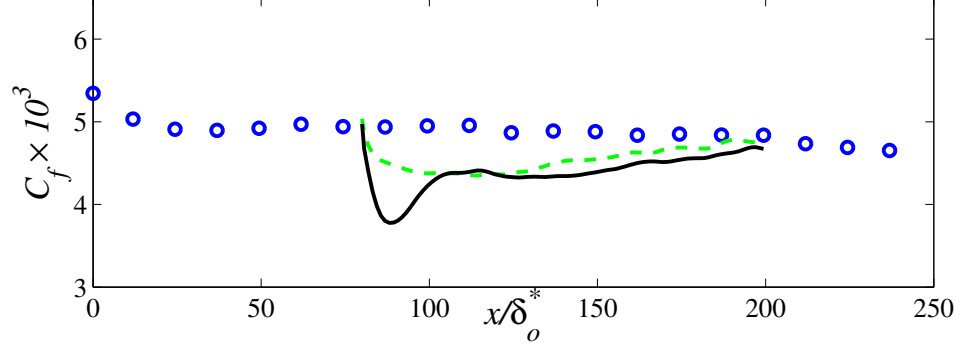


Figure 3.4: Skin friction coefficient C_f with $K_I = 5$ and $K_P = 30$; --- first control plane after one grid cell; — first control plane after one boundary layer thickness results are also strongly influenced by the time window of the MA filter. Excessively small values of T_{ave} result in incorrect steady state results, while the other values of T_{ave} are in reasonable agreement with each other. The case with $T_{ave} = 10$ (*i.e.*, T_d of the order of one LETOT) seems, altogether optimal, since it results in somewhat more accurate statistics and a much shorter transient (and reduced CPU costs). Unless explicitly specified, $T_{ave} = 10$ for all following cases.

On a related note, it should be mentioned that previous applications of the controlled forcing method [49, 50, 30] used spanwise averaging (in addition to the time-averaging in the MA block) to supply a smoother signal to the forcing; also the first control plane was located one boundary-layer thickness downstream of the inflow plane. We now try to better address these choices. Regarding the control plane, the result in term of C_f coefficient in Figure 3.4 shows that the best choice is to have the first control plane immediately after the inflow plane. This was not evident in [50, 30] because the parameters were not in the optimal range, expecially

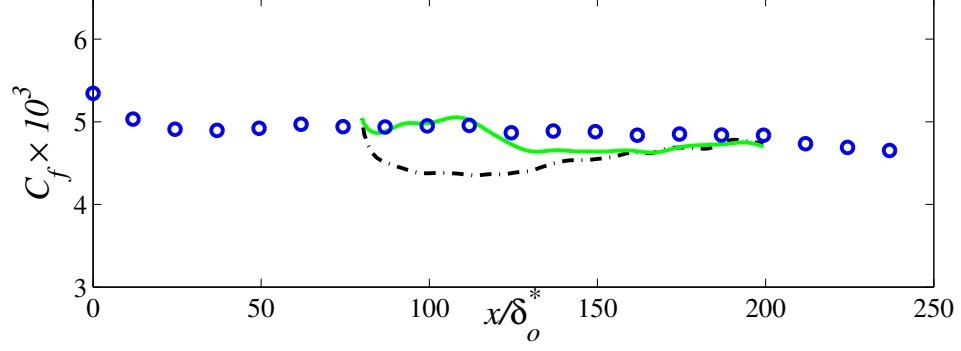


Figure 3.5: Skin friction coefficient C_f with $K_I = 5$ and $K_P = 30$; $---$ $\langle u'v' \rangle^t$ is spanwise-averaged; $---$ $\langle u'v' \rangle^t$ is not spanwise-averaged.

the time window T_{ave} . If this is not tuned well, the control has a weak sensitivity on the position of the control planes.

Regarding the spanwise average, Figure 3.5 shows calculations in which no spanwise averaging was performed, compared to a simulation in which the $u'v'$ correlation is averaged in the spanwise direction as well as in time. Better results are obtained when the error reflects more closely the local and instantaneous conditions of the flow. We observe more rapid adjustment of the flow towards the reference LES, as the forcing is more responsive to the local state of the flow.

In the next subsection we will turn the attention to the PI controller. This will allow us to evaluate the influence of its parameters on the transient time and steady-state results.

3.2.3 The PI control

In general a proportional controller affects the rise-time and the transient time of the dynamic system: it modifies the bandwidth of the frequency response of the closed loop system and the gain of the zero frequency. If K_P is large, the output of the integral block is more sensitive to the high-frequency variation of the error, and the stability of the system can be affected. The integral control, on the other hand, gives a large gain at low frequency and reduces the break frequency (the point where the amplitude spectrum of the transfer function is zero); its effect is to eliminate the steady-state error and attenuate the high-frequency disturbances. In fact, the output of the integral control will change over time as long as an error exists, but the phase lag between the input and output of the integral block increases for all of the frequencies (the phase of the integrator block starts at -90°). If K_I is large, the phase lag is extended to higher frequency, so the system can become oscillatory and potentially unstable.

To better understand these considerations, we evaluate the transfer function of the PI control, *i.e.*, the Laplace transform of (3.3) divided by the Laplace transform of the error $e(t)$:

$$G(s) = K_P + \frac{K_I}{s} \quad (3.6)$$

where s is the complex variable $s = \alpha + j\omega$. It is simple to see the frequency response of the PI control: setting $s = j\omega$ (Fourier domain) we have that the magnitude and

the phase of $G(\omega)$ are

$$|G(\omega)| = \sqrt{K_P^2 + \frac{K_I^2}{\omega^2}} \quad (3.7)$$

$$\Phi = \tan^{-1} \left(-\frac{K_I}{\omega K_P} \right). \quad (3.8)$$

To see the behaviour of these function in the frequency domain, the Bode plot is used in figures 3.6 and 3.7 (*i.e.* $|G(\omega)|_{dB} = 20 \log_{10}(|G(\omega)|)$ *vs* $\log_{10}(\omega)$ and Φ *vs* $\log_{10}(\omega)$). From these figures is evident that the integral control introduce a phase lag that increases with K_I

Figure 3.8 shows how the transient is affected by K_P and K_I . If $K_P = 0$ (only the integral control is activated) the calculation diverges: in the initial transient the forcing is proportional to $e(t')dt'$ and the initial time-step is small because of the initial unphysical flow in the computational domain. Because of the small time-step the integral action is weakened, so the integral control needs a longer time before it can give a correct control signal. As the simulation advances, however, the time-step is further decreased because no fast correction is present in the domain, so the correct integral action is even more delayed until the simulation goes unstable. The case of high K_P is the opposite: as soon as the simulation starts there is the fast correction due to the proportional control. Apart from the length of the transient, however, the steady-state results did not differ much in all the converged calculations, showing little sensitivity of the flow to the proportional controller (at least for $K_P > 1$).

Similarly, we found instability for $K_I \geq 30$, as can be expected by the theory of the PI feedback control. If K_I was close to zero, only the proportional control

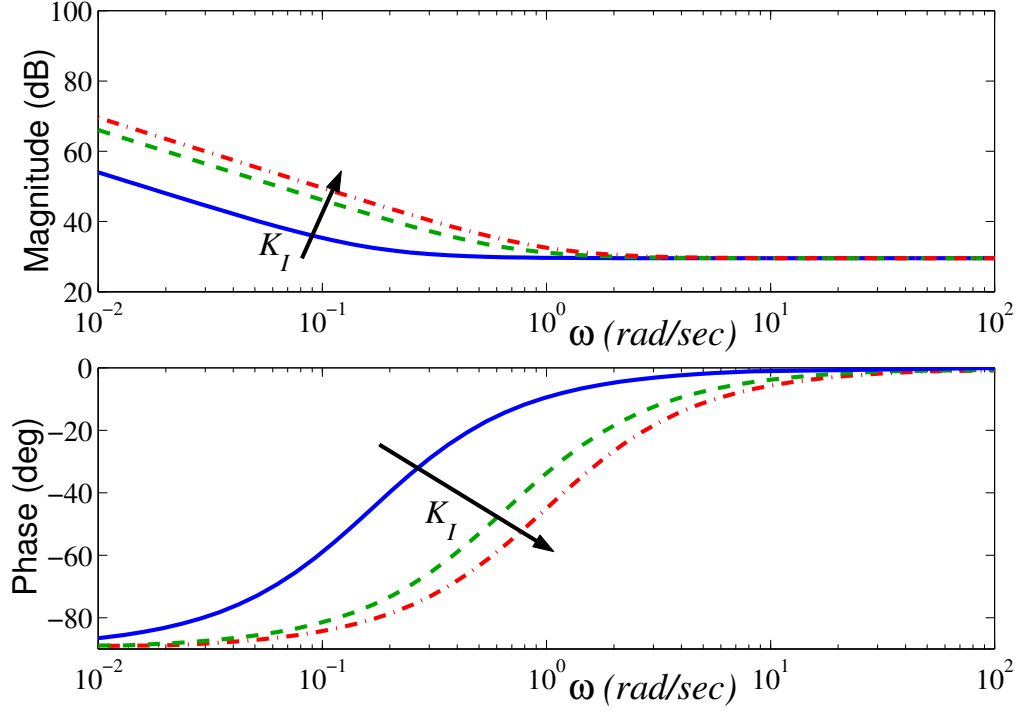


Figure 3.6: Bode plot of the frequency response of the PI system for different value of K_I and fixed $K_P = 30$. — $K_I = 5$; - - - $K_I = 20$; - · - $K_I = 30$; It is evident that when K_I increase, the gain at low frequency increase and the phase lag value starting at -90 is kept to higher frequency, *i.e.*, the response of the PI system lags behind the input wave by 90 deg in the worst case

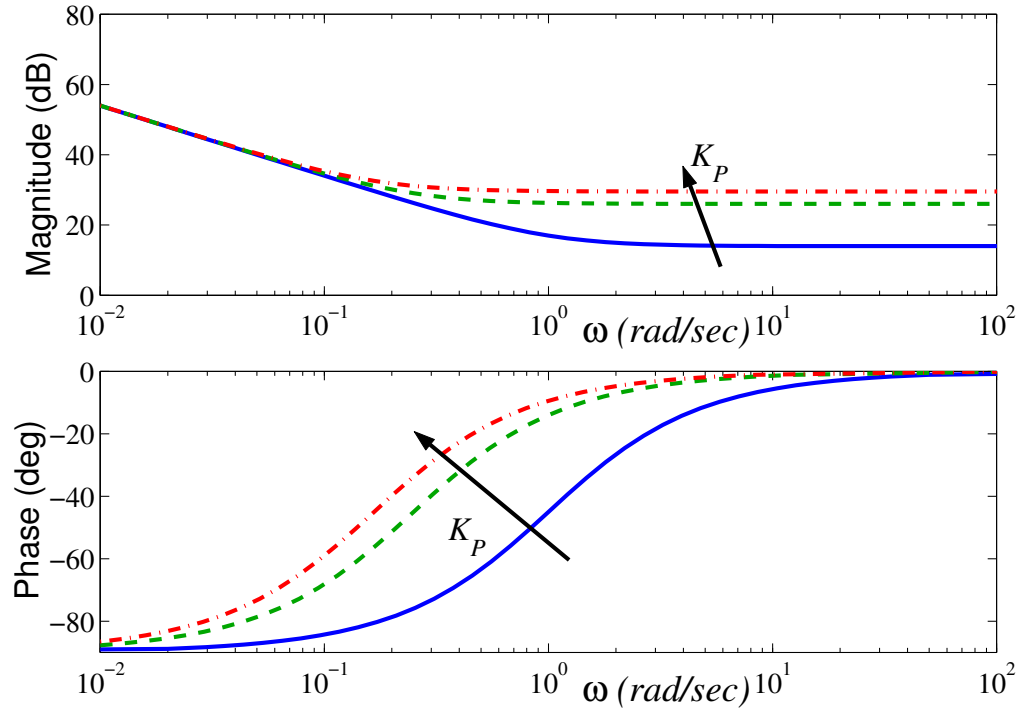


Figure 3.7: Bode plot of the amplitude and phase frequency response of the PI system for different values of K_P and fixed $K_I = 5$. — $K_P = 5$; - - $K_P = 20$; - · - $K_P = 30$. When K_P increases, the gain at high frequency increase and the phase lag value decreases at higher frequency

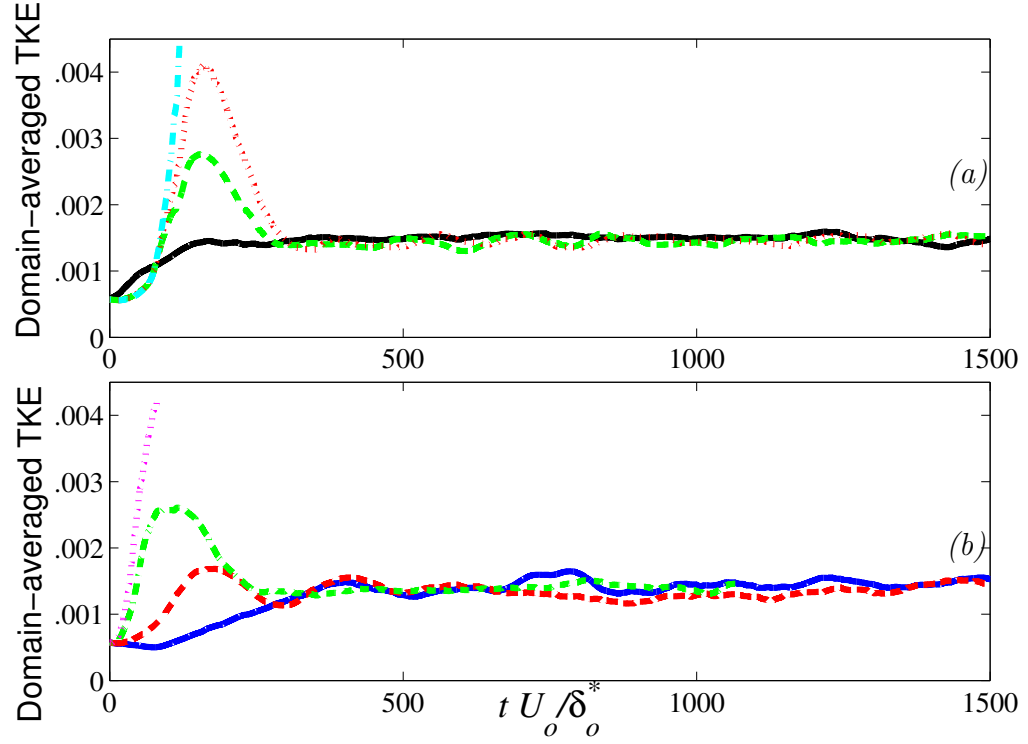


Figure 3.8: Domain-averaged turbulent kinetic energy. (a) $K_I = 5$ and $K_P = 0$; $K_I = 15$; $K_I = 30$; $K_I = 500$; (b) $K_P = 30$ and $K_I = 1$, $K_P = 5$, $K_P = 20$, $K_P = 30$.

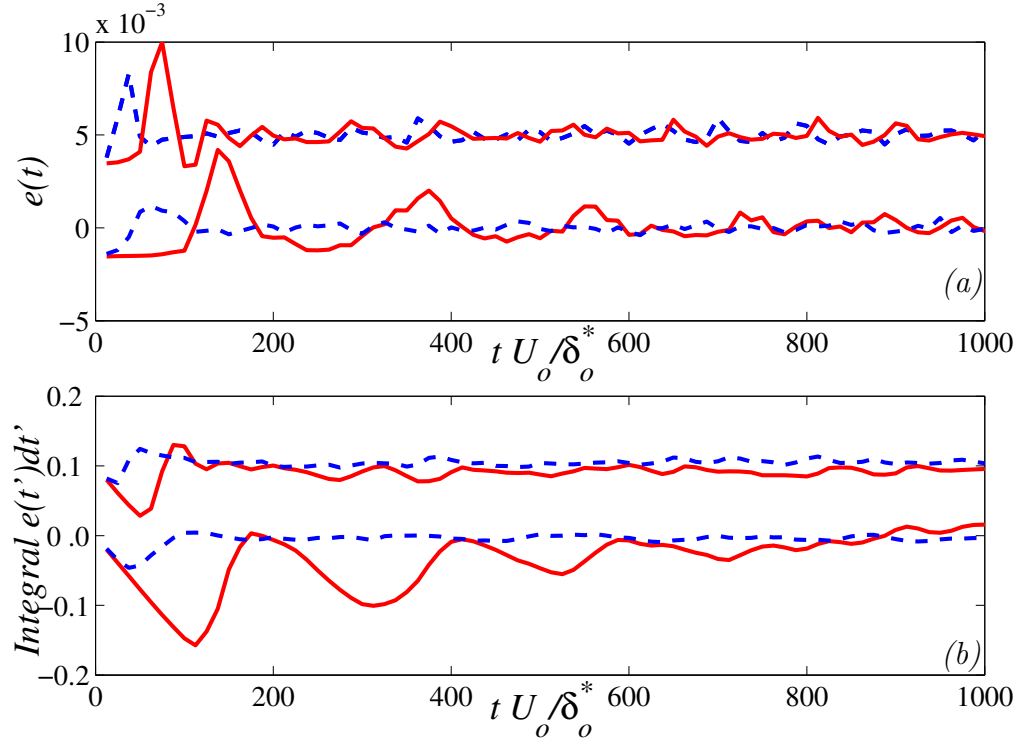


Figure 3.9: (a) Instantaneous and (b) integrated error for $K_P = 30$ and $K_I = 5$ (lines) and $K_I = 20$ (lines with symbols). — $y^+ = 13$; --- $y/\delta_o^* = 4.5$. The curves for $K_I = 20$ are shifted upwards by 0.005 in (a) and 0.1 in (b).

was activated and the steady state error (the difference between the desired Reynold stress and the one obtained from the calculation) was large. Figure 3.9 shows the error and its integral at two locations, one in the wall layer, the other in the outer region of the boundary layer, for $K_P = 30$ and two values of K_I . Increasing K_I reduces the amplitude of the dominant frequency of the error, as well as its amplitude, at least in the outer layer. Note, however, that the forcing signal (which has the integral error multiplied by K_I) does not change its magnitude.

3.2.4 Conclusions

As a result of the tests described in this section, we conclude that some localization of the error, both in time and space, is desirable. Compared with the work of Keating *et al.* [30], we obtained improved results using a shorter time-averaging window, and removing the spanwise averaging. Averaging over a time interval of the order of the local integral time-scale resulted in shorter transient and more rapid development of physically realistic turbulent eddies. Removal of the spanwise averaging used in previous investigations also gave improved results, as the error (and hence the forcing) reflected more accurately the local state of the flow. The controller parameters, the constants K_P and K_I , play a less significant role. Giving excessive weight to the integral error, or insufficient one to the proportional part, resulted in instabilities of the flow. For a wide range of values of K_P and K_I , on the other hand, the flow statistics were found to be insensitive to the constants. We

observed that the controller coefficients mostly affect the length of the transient; for a wide range of both K_I and K_P , however, the flow statistics are fairly insensitive to the parameter values. In the next section we will apply the method with the improved coefficients to four flows, to determine its performance (with the new coefficients) in actual cases.

In the next Chapter, we will report results obtained applying the PI control to different boundary layer cases, including boundary layers undergoing adverse and favorable pressure gradients, and a three-dimensional boundary layer.

Chapter 4

Application of the controlled forcing

4.1 Introduction

In this Chapter the application of the controlled forcing is presented for different boundary layer configurations: zero pressure gradient (ZPG), adverse pressure gradient (APG), favorable pressure gradient (FPG), and three dimensional boundary layer (3D). It is important to test the controlled forcing for these different flow, to prove that the tuning discussed setup in the previous Chapter, especially the optimal range found for the PI control, is not a “single-case” optimal tuning, but can be extended to different configuration. The only parameter that need to be matched with the local characteristic of the flow is T_{ave} , the width of the moving average filter that must match with the intrinsic scales of the turbulent structures.

4.1.1 Zero-pressure-gradient boundary layer

In this Section we report results obtained from calculations of the zero-pressure-gradient (ZPG) boundary layer. In the previous Chapter the reference LES provided the inflow statistics; here, they are calculated from the RANS; the modeling errors that would affect real hybrid RANS/LES calculations are going to play an important

role.

Figure 4.1 compares a case in which the $k - \epsilon$ model is used for the RANS with one that employs the SA model. One can observe the effect of modeling errors: First, the $k - \epsilon$ model gives a prediction of the wall stress in better agreement with the reference LES than the SA model; the $k - \epsilon$ model also gives k and ϵ (which are required by the synthetic turbulence generation method) directly, while with the SA model they must be estimated using (2.86). The skin-friction coefficient matches the reference LES value after only $20\delta_o^*$ from the end of the control region (approximately 2 boundary layer thicknesses) with the $k - \epsilon$ model, while it requires a longer distance with the SA model. Both the mean velocity profiles and the Reynolds stresses are in good agreement with the reference calculation, except perhaps in the outer layer where the growth of realistic structures is somewhat slower (as was discussed in [50]). Figure 4.3 shows the C_f obtained with the coefficients $T_{ave} = 100$, $K_I = K_P = 1$ as in [50], and the case when only synthetic turbulence is applied at the inflow without any control.

One limitation of the current approach lies in the fact that the error is based on the Reynolds shear stress, which is not a coordinate-invariant quantity; in complex geometries, the error might be ill-defined. The proposed RANS/LES merging approach, however, is predicated on the RANS calculation being accurate in the interface region, which in practice restricts the interface to lie in a thin, attached shear layer, where the definition of directions along and normal to the shear layer is

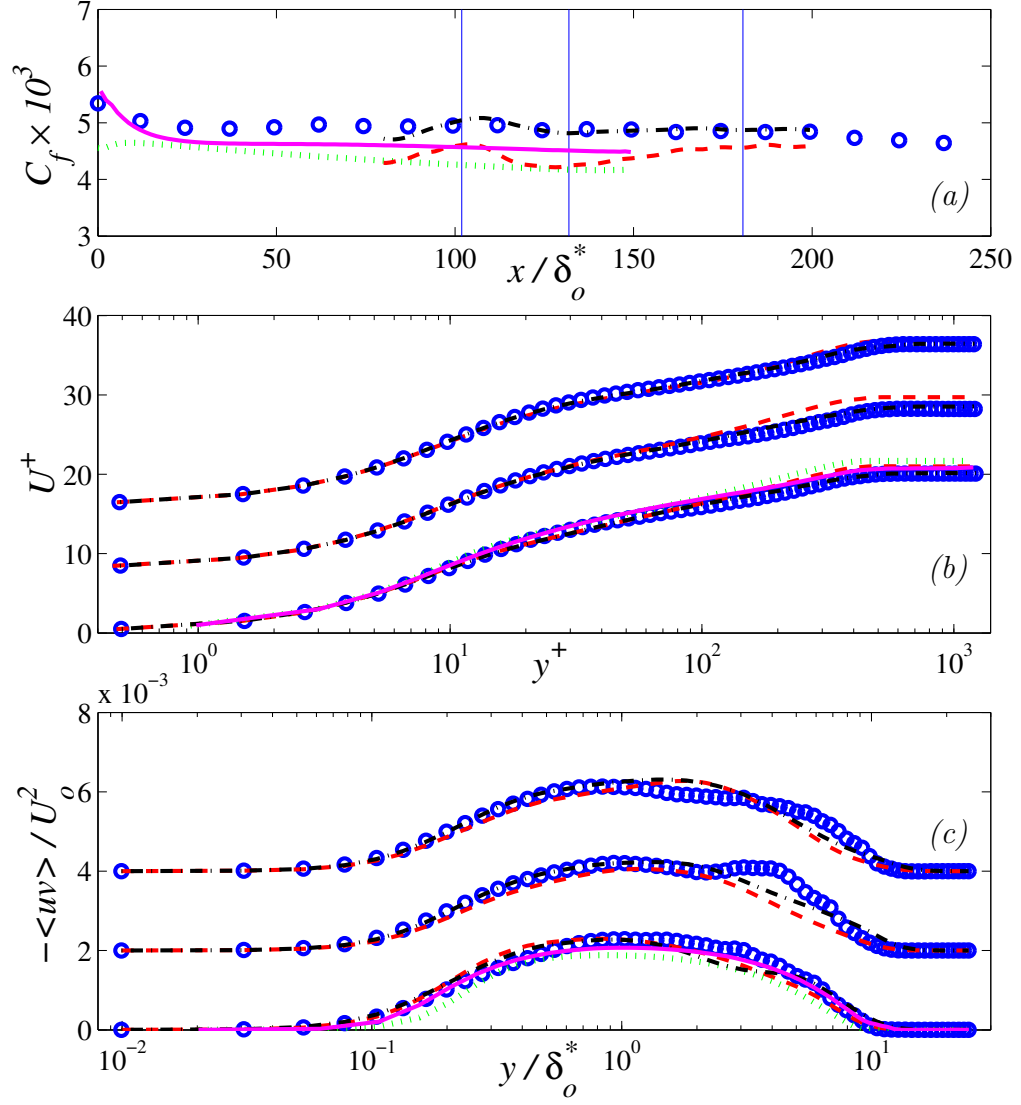


Figure 4.1: Zero-pressure-gradient boundary layer. (a) Skin friction coefficient C_f (b) mean velocity profiles and (c) profiles of the Reynolds shear stress at the locations indicated by a vertical line in part (a). \circ Reference LES; — $k - \epsilon$ RANS; --- Hybrid $k - \epsilon$ /LES; - - - SA RANS; - - - Hybrid SA/LES.

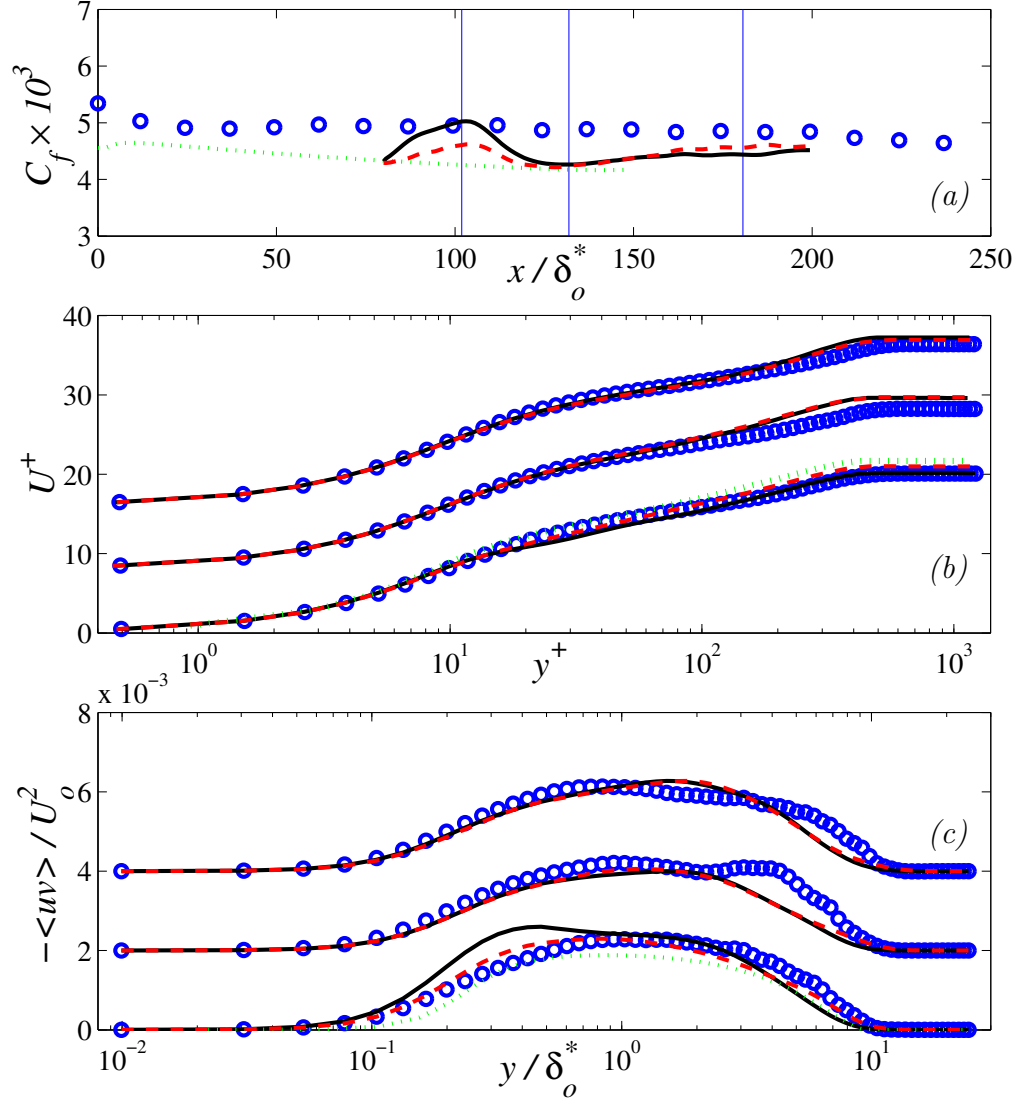


Figure 4.2: Zero-pressure-gradient boundary layer. (a) Skin friction coefficient C_f (b) mean velocity profiles and (c) profiles of the Reynolds shear stress at the locations indicated by a vertical line in part (a). \circ Reference LES; \cdots SA RANS; $---$ error based on $\langle u'v' \rangle$; $—$ production-based error.

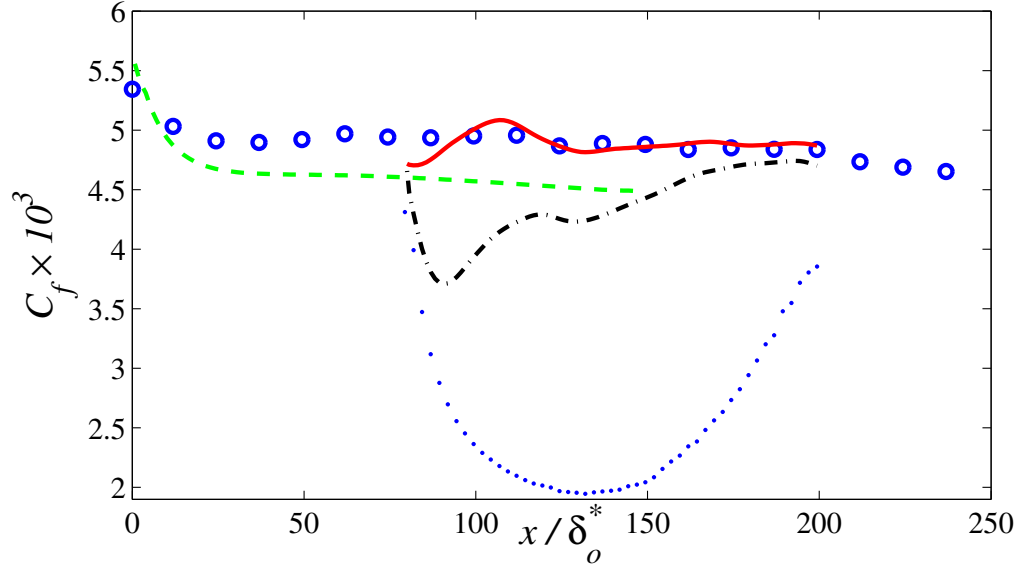


Figure 4.3: Skin friction coefficient C_f in the case of hybrid $k-\epsilon$ /LES simulation.

\circ Reference LES; $---$ RANS $k-\epsilon$; $—$ Hybrid $k-\epsilon$ /LES with $T_{ave} = 10$,
 $K_I = 5$, $K_P = 30$; $- \cdot -$ Hybrid $k-\epsilon$ /LES with $T_{ave} = 100$, $K_I = 1$, $K_P = 1$ as in
 [30]; \cdots Hybrid $k-\epsilon$ /LES with only Batten synthetic turbulence at the interface

unique. Despite this practical observation, it would be desirable to develop a more universal error definition, and in particular one that is invariant to the choice of the frame of reference. One possible choice to satisfy this requirement is to base the error on the production of turbulent kinetic energy, which satisfies the desired invariance properties. Thus, we define a production-based error

$$e^P(y, z, t) = -\langle u'_i u'_j \rangle_{des} \langle S_{ij} \rangle_{des} + \langle u'_i u'_j \rangle^t \langle S_{ij} \rangle^t \quad (4.1)$$

(where the dependence on x_o , y , z and t has been omitted, and S_{ij} is the strain-rate tensor). For the ZPG boundary layer examined here this definition of the error should give the same result as (3.1), since the shear stress is the leading term in the definition of the production. We found results comparable to those obtained using the shear stress in the definition of the error, with two notable differences: first, e^P decays more rapidly than e away from the wall (since the velocity gradient goes to zero); this results in less forcing in the outer layer, so that the correct Reynolds-stress profile away from the wall is established further downstream, compared with the case in which the error is defined by (3.1). Secondly, we observed a much longer transient before the error stabilized; may be due to the decreased forcing in the outer layer again, which slows the production of $\langle u'v' \rangle$, and hence the decrease of the error there.

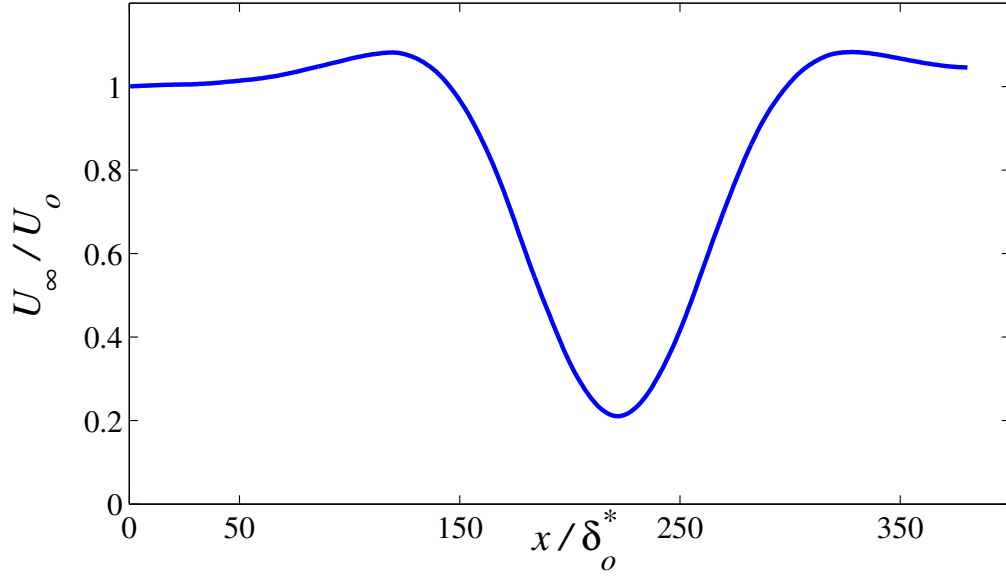


Figure 4.4: Freestream velocity for the adverse-pressure-gradient calculation.

4.1.2 Adverse-pressure-gradient boundary layer

Hybrid simulations were next carried out in an adverse-pressure-gradient (APG) boundary-layer that undergoes separation. The configuration of these simulations is similar to that of [30], with an inflow Reynolds number, $Re_{\delta^*} = 1260$, and a profile of V_∞ imposed at the top boundary that results in a significant deceleration of the flow (see Figure 4.4). Due to the strong adverse pressure-gradient, the flow separates; a favorable pressure gradient then closes the recirculation bubble.

The computational domain used in the full-domain LES was $380\delta_o^* \times 64\delta_o^* \times 20\delta_o^*$. This LES, which used the rescaling/recycling method at the inflow, had a grid of $384 \times 192 \times 64$. The RANS calculations for the hybrid cases were extended to cover the entire flow domain to remove difficulties of placing outflow boundary

conditions close to reversed-flow regions; both SA and $k - \epsilon$ models were used for the RANS solution. The LES region started at $x/\delta_o^* \approx 80$, and used the RANS data at that location for the synthetic turbulence generation, as well as target for the controlled forcing algorithm. The δ^*/u_τ obtained from the $k - \epsilon$ model at the interface location was approximately 110, which agrees well with the value from the full LES. To match this value, T_{ave} was fixed to 38, so that the memory T_d was approximately 113. K_I was fixed at 5 and K_P to 30.

Figure 4.5 shows the C_f , mean velocity profiles and Reynolds shear stresses at three locations. As the boundary layer is subjected to the adverse pressure-gradient, C_f decreases until the flow separates at $x/\delta_o^* \approx 170$. A weak separation bubble, which has a length of approximately $80\delta_o^*$, can be observed in the full-domain LES. The results from the RANS simulation in terms of C_f are close to those of the full LES. Switching to the LES is, however, beneficial (the prediction of C_f and the dimensions of the separation bubble are both more accurate). Shortly after separation (the second profile in Figure 4.5) some differences between the hybrid cases can be observed, whereas inside the separation bubble the LES give similar results. In this flow, the amplification of turbulence in the separated shear layer acts as a powerful mechanism to accelerate the generation of realistic eddies. However, the mean streamline shown in Figure 4.6 show that the separation bubble in the hybrid calculation is still larger than the full LES, especially when the SA model is applied in the RANS region. As the zero pressure gradient boundary layer, the

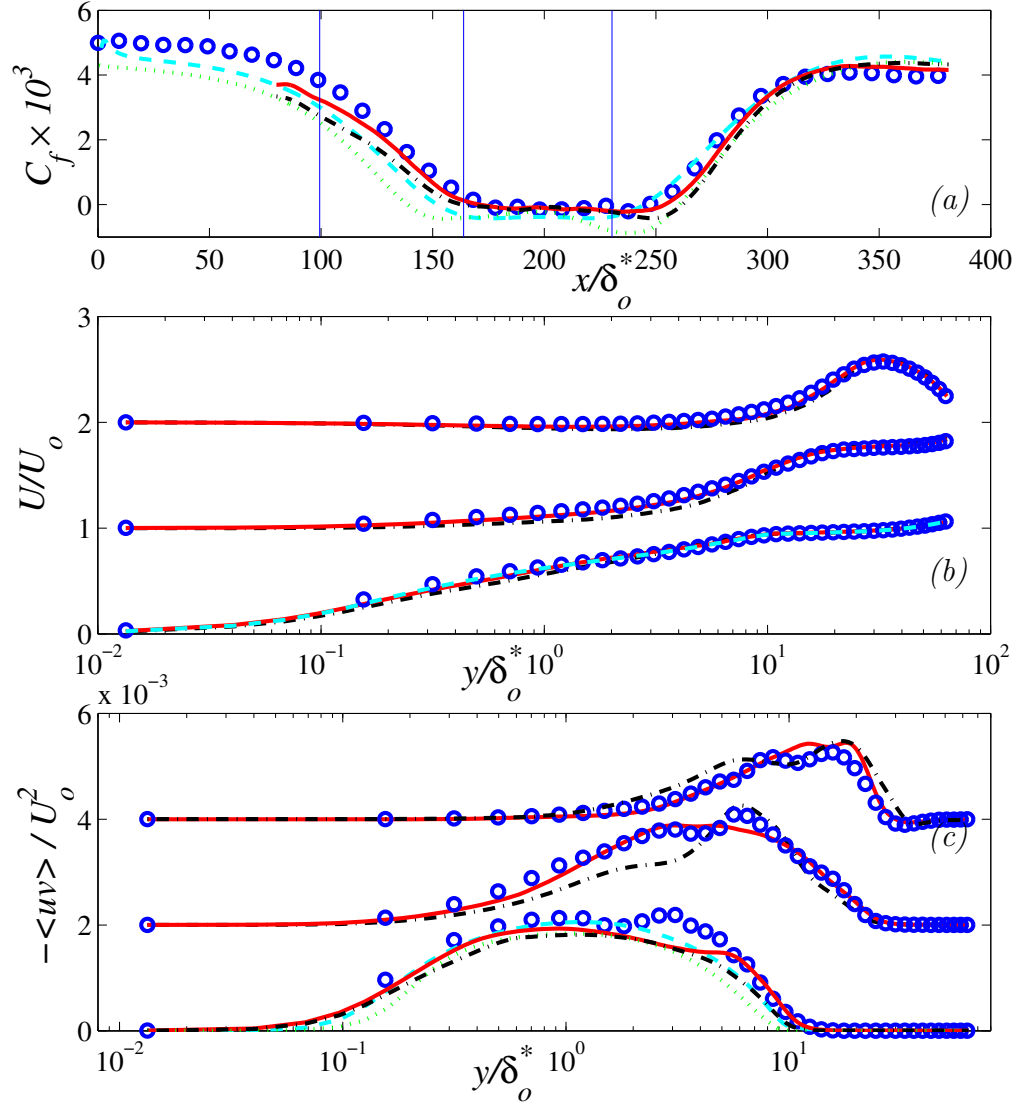


Figure 4.5: Adverse-pressure-gradient boundary layer. (a) Skin friction coefficient C_f (b) mean velocity profiles and (c) profiles of the Reynolds shear stress at the locations indicated by a vertical line in part (a). \circ Reference LES; $---$ $k-\epsilon$ RANS, \cdots SA RANS; $—$ hybrid $k-\epsilon$ /LES; $- - -$ Hybrid SA/LES.

$k - \epsilon$ model gives better performances in the hybrid simulation

Keating *et al.* [30] observed a much stronger dependence of the hybrid results on the accuracy of the RANS model (see Figure 11 in [30]), as is shown in figure 4.7. This effect is due to the use of suboptimal PI controller parameters and averaging window. With the more localized averaging used here, the initial decay of the wall stress that was observed by Keating *et al.* [30] does not occur.

Figure 4.8 shows contours of streamwise velocity fluctuations in a plane near the wall for the reference LES and a hybrid case. We observe a very rapid development of a physical streaky structure. The onset of separation (which is strongly affected by the flow state immediately before the separation occurs) is predicted well, and the length-scales of the flow in the separated-flow region are remarkably similar, confirming again the robustness and effectiveness of the method.

4.1.3 Favorable-pressure-gradient boundary layer

Simulations of a boundary layer subjected to a favorable pressure-gradient (FPG) were performed. In this flow, if the acceleration is rapid enough, re-laminarization and re-transition of the flow may occur. The case studied here matches the experiments of [97]. The freestream acceleration (from $U_\infty = 1$ to $U_\infty \approx 3$) begins at approximately $100\delta_o^*$ and is completed by $450\delta_o^*$. The flow acceleration is achieved by imposing a streamwise velocity profile $U_\infty(x)$ at the top boundary of the domain [102]. Its magnitude was calculated from the acceleration parameter,

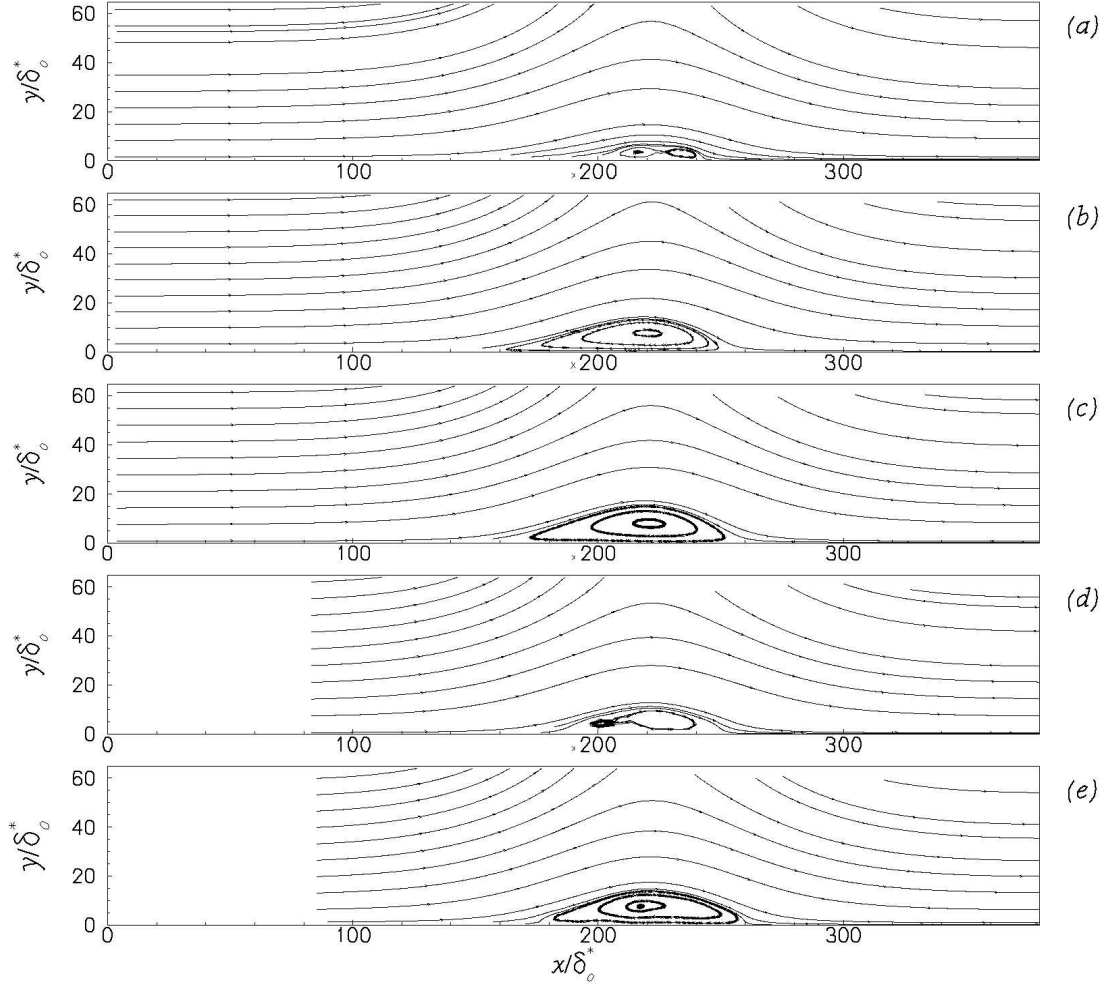


Figure 4.6: Mean streamlines for the APG boundary layer. (a) Reference LES; (b) $k - \epsilon$ RANS; (c) SA-RANS; (d) hybrid $k - \epsilon$ /LES; (e) hybrid SA/LES.

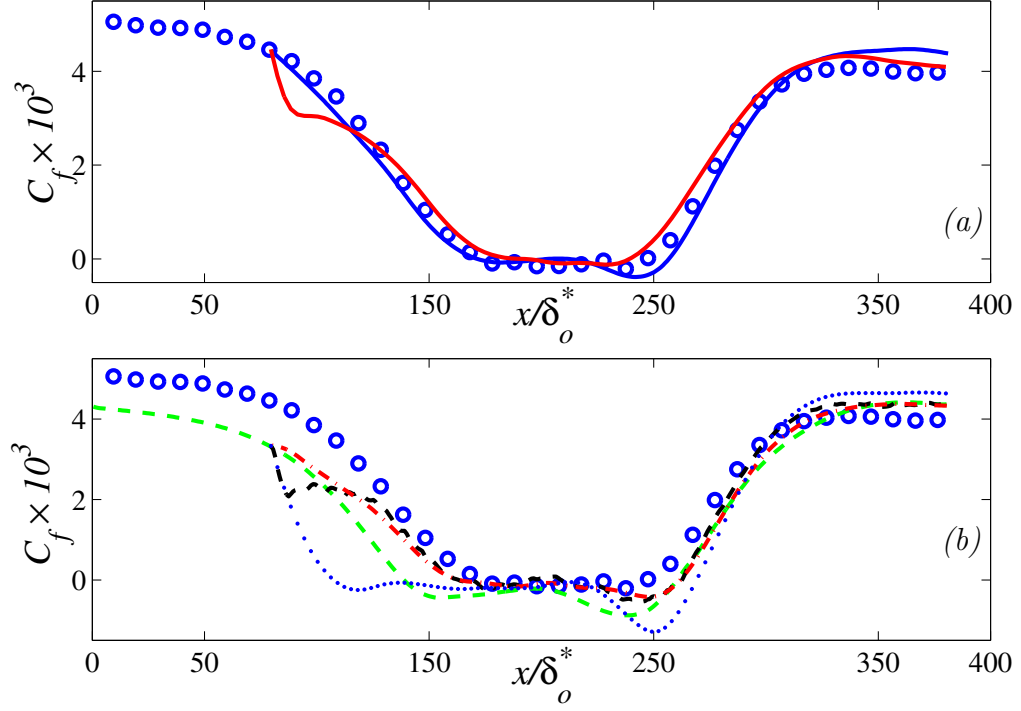


Figure 4.7: Skin friction coefficient C_f in the case of LES/LES simulation (a) and hybrid RANS SA/LES (b). In (a) — $T_{ave} = 38$, $K_I = 5$, $K_P = 30$; — $T_{ave} = 100$, $K_I = 1$, $K_P = 1$ as in [30]. In (b) --- RANS SA model, -.- hybrid SA/LES with $T_{ave} = 38$, $K_I = 5$, $K_P = 30$; --- $T_{ave} = 100$, $K_I = 1$, $K_P = 1$ as in [30]; Hybrid SA/LES with only Batten synthetic turbulence at the interface

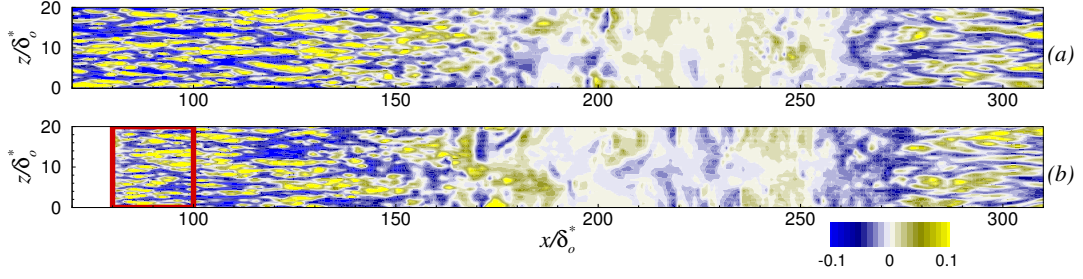


Figure 4.8: Streamwise velocity fluctuations in the APG boundary layer, in the $y/\delta_o^* = 0.09$ plane. (a) Reference LES; (b) hybrid $k - \epsilon$ /LES; the red rectangle indicates the region where the control is active.

$K = (\nu/U_\infty^2)(dU/dx)$, experimentally obtained from [97]. The acceleration parameter, K , and the free-stream velocity distribution $U_\infty(x)$ are the same as [30]. Since K exceeds the critical value for re-laminarization ($K_{crit} = 3.5 \times 10^{-6}$) for an extended region of the flow, turbulence is expected to be damped in the region of high acceleration. The flow then re-transitions once the acceleration is removed.

A full-domain LES was first performed using the rescaling/recycling method at an inflow Reynolds number, $Re_{\delta^*} = 1260$. For this simulation the domain length was $476\delta_o^*$, the width was $20\delta_o^*$ and the height was $20\delta_o^*$. A somewhat coarse grid ($512 \times 64 \times 64$) was used, since the comparisons were primarily being made between this full LES and a hybrid RANS/LES simulations. One hybrid calculations was performed that included a RANS domain $350\delta_o^*$ long, and an LES region that started at $x/\delta_o^* = 225$ and extended to $476\delta_o^*$ (*i.e.*, had a length $251\delta_o^*$). Synthetic turbulence with controlled forcing was introduced at the RANS/LES interface.

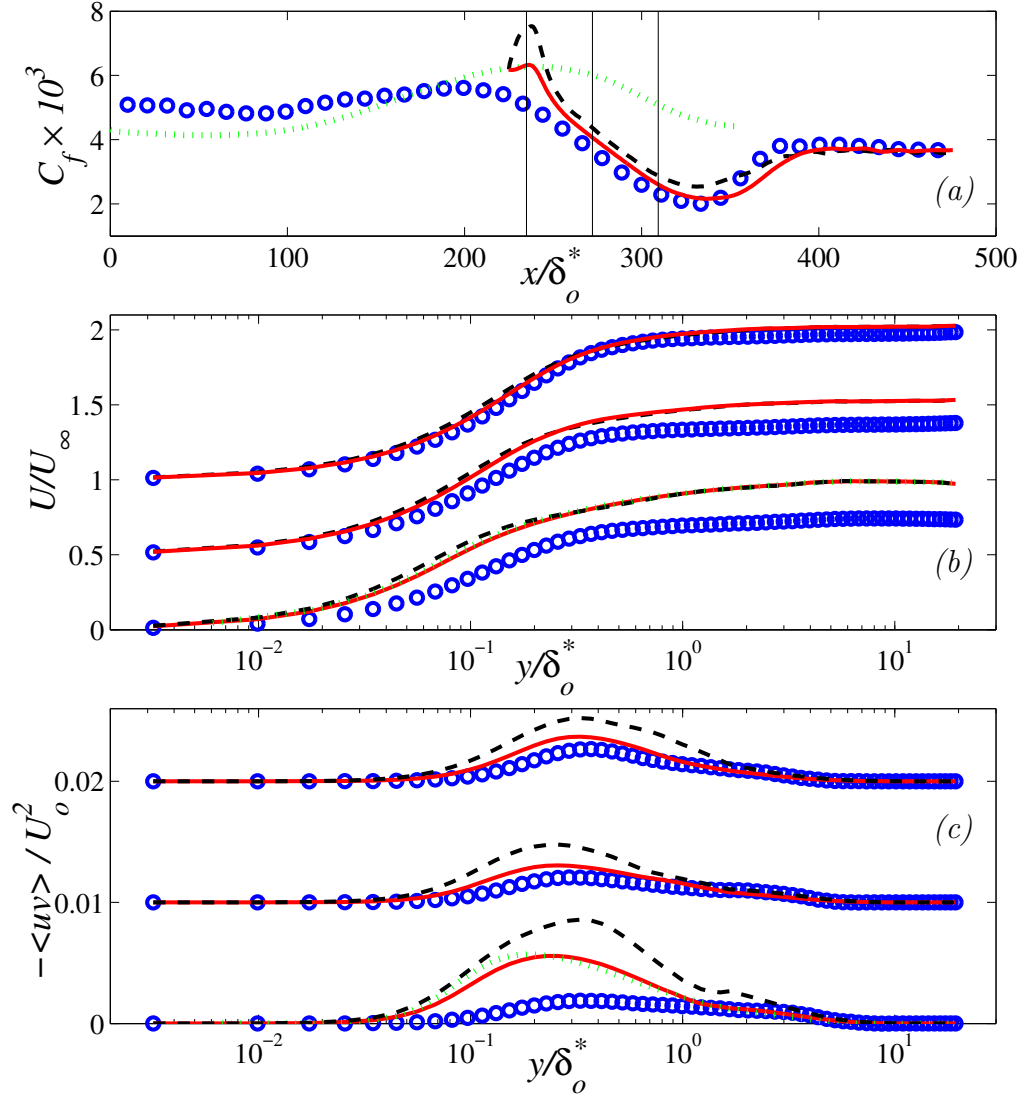


Figure 4.9: Favorable-pressure-gradient boundary layer. (a) Skin friction coefficient C_f (b) mean velocity profiles and (c) profiles of the Reynolds shear stress at the locations indicated by a vertical line in part (a). \circ Reference LES; \cdots SA RANS; --- hybrid SA/LES, T_{ave} from LES data; --- hybrid SA/LES, T_{ave} from RANS data; .

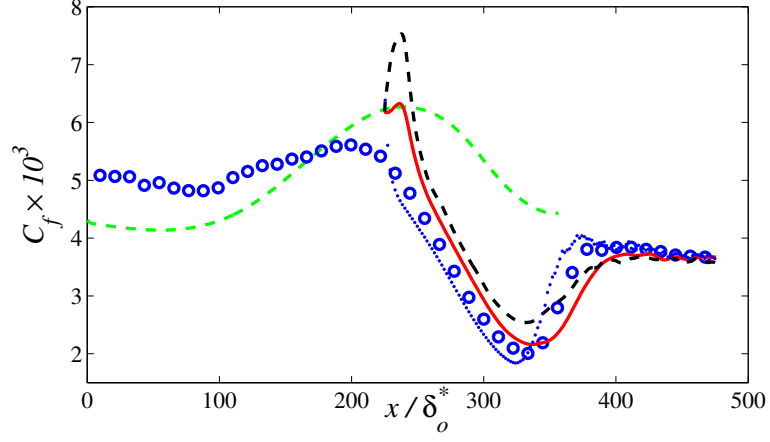


Figure 4.10: Skin friction parameter C_f for the favorable pressure gradient boundary layer: \circ reference LES, $---$ RANS, $—$ hybrid RANS/LES with $T_{ave} = 2.4$ and $---$ $T_{ave} = 1$; \cdots Hybrid SA/LES with only Batten synthetic turbulence at the interface

All the different RANS model tested give significant modeling error; in particular, no model was able to predict the relaminarization and the re-transition of the accelerating boundary layer correctly. Furthermore, with the SA model, the timescale δ^*/u_τ at the interface location was found to be approximately 2, while the value obtained from the full LES calculation is twice as large in the region where the control was applied. Two hybrid calculation were performed, one that used a value of T_d close to the time-scale predicted by the RANS (giving $T_{ave} = 1$), and another that matched the LES timescale ($T_{ave} \simeq 2.4$). Figure 4.9 compares the results of the various simulations. The mean data at the interface, which is supplied by the RANS, is not accurate; the controller tries to drive the LES towards the RANS

region, but when T_{ave} is small a smooth $\langle u'v' \rangle$ cannot be obtained, and excessive forcing is applied, resulting in an initial overshoot of the skin-friction coefficient. Once the control is released, the flow adjusts fairly rapidly towards the full-domain LES. When a longer average is used, the controller is more successful in driving the LES shear stress towards the desired distribution (Figure 4.9(c)) and the LES adjusts more rapidly and with no overshoot. Note finally that this is a very challenging test case: RANS models cannot be expected to predict relaminarization accurately; furthermore, since the energy of the fluctuations is decreasing because of the acceleration, adding energy through the forcing term is moving the flow away from its equilibrium. This is evident in Figure 4.10 where are shown the two cases with control presented before, and the case when only synthetic turbulence is used at the inflow: in this last case the flow is drawn through the full LES configuration soon after the first grid cell; however, the retransition to turbulent flow is leaded. Despite the fact that this can be considered an off-design application for the controlled forcing, the results are altogether acceptable.

4.1.4 3-D Boundary layer

Simulations were then performed on a 3D boundary layer obtained by applying a spanwise pressure gradient to a flat-plate boundary layer. The pressure gradient increased from zero, at $x/\delta_o^*=100$, up to 1.5×10^{-3} at $x/\delta_o^*=150$, and remained constant thereafter. The magnitude of the pressure gradient was set in such a way

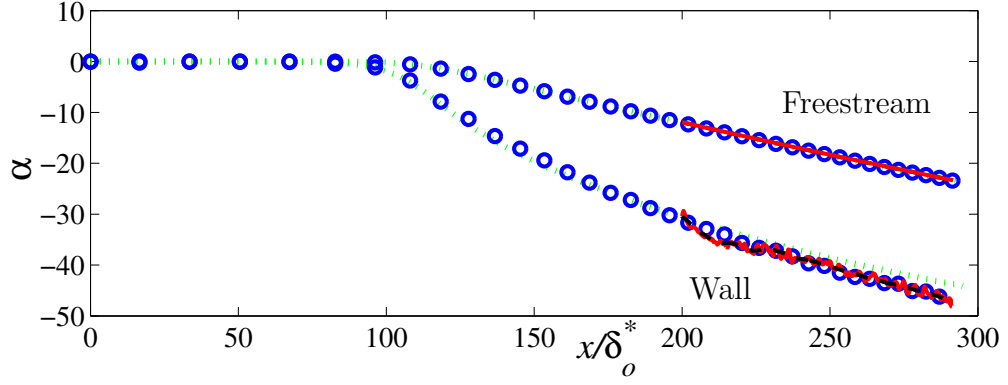


Figure 4.11: 3D boundary layer. Flow angle $\alpha = \tan^{-1} U/W$. \circ Reference LES.
 ----- SA-RANS; - - - error based on $\langle u'v' \rangle$; — production-based error.

as to turn the flow by 45° near the wall and 24° at the free stream by the end of the domain. Figure 4.11 shows the turning angle near the wall and in the freestream.

Once again, two simulations were carried out: a full-domain LES, and one hybrid RANS/LES calculations. The computational domain of the reference LES was $291\delta_o^* \times 20\delta_o^* \times 20\delta_o^*$ with a grid of $720 \times 100 \times 292$. An inflow plane from a precursor simulation was used with an inflow Reynolds number of $Re_{\delta^*} = 1260$. Because of the turning of the flow, the grid had to be refined in the streamwise direction in the downstream area. We define a local coordinate frame with ξ in the flow direction and ζ in the lateral direction in the wall plane:

$$\Delta\xi^+ = \Delta x^+ \cos \alpha + \Delta z^+ \sin \alpha; \quad \Delta\zeta^+ = \Delta x^+ \sin \alpha + \Delta z^+ \cos \alpha. \quad (4.2)$$

We maintained streamwise and spanwise grid resolutions of $\Delta\xi^+ < 50$ and $\Delta\zeta^+ < 13$ as is shown in figure 4.12. Here, α is the flow angle at the wall and wall units are

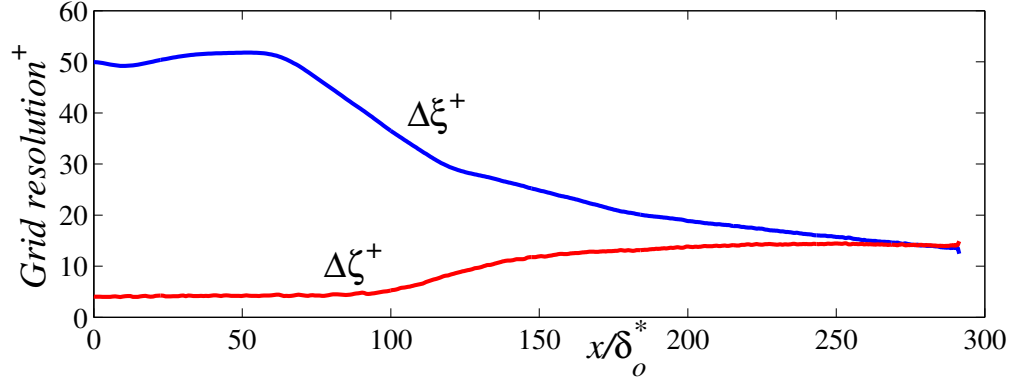


Figure 4.12: Grid resolution obtained in the 3D boundary layers — $\Delta\zeta^+$; — $\Delta\xi^+$

defined using the resultant wall stress

$$\rho u_\tau = (\tau_{xy,w}^2 + \tau_{xz,w}^2)^{1/4}; \quad \tau_{xy,w} = \mu \left. \frac{\partial U}{\partial y} \right|_{y=0}; \quad \tau_{xz,w} = \mu \left. \frac{\partial W}{\partial y} \right|_{y=0}. \quad (4.3)$$

In the hybrid cases, the RANS equations was solved using the Spalart-Allmaras model. The LES region started at $x/\delta_o^* \approx 200$ where the flow angle was 32° near the wall and 12° in the free-stream. The SA model predicts a value of $\delta^*/u_\tau = 40$ at the RANS/LES interface; consequently, we set $T_{ave} = 14$ (corresponding to $T_d \simeq 42$). We also performed simulations with the production-based error, in addition to those with the standard definition of e .

Figure 4.13 shows the skin friction coefficient and mean velocity profiles in the streamwise and spanwise directions. The development of $C_{f,x}$ is similar to that of the ZPG case (with an initial decrease followed by a quick recover). For the lateral flow we observe remarkably good agreement with the reference simulation beginning from the end of the controlled region, approximately two boundary layer thicknesses

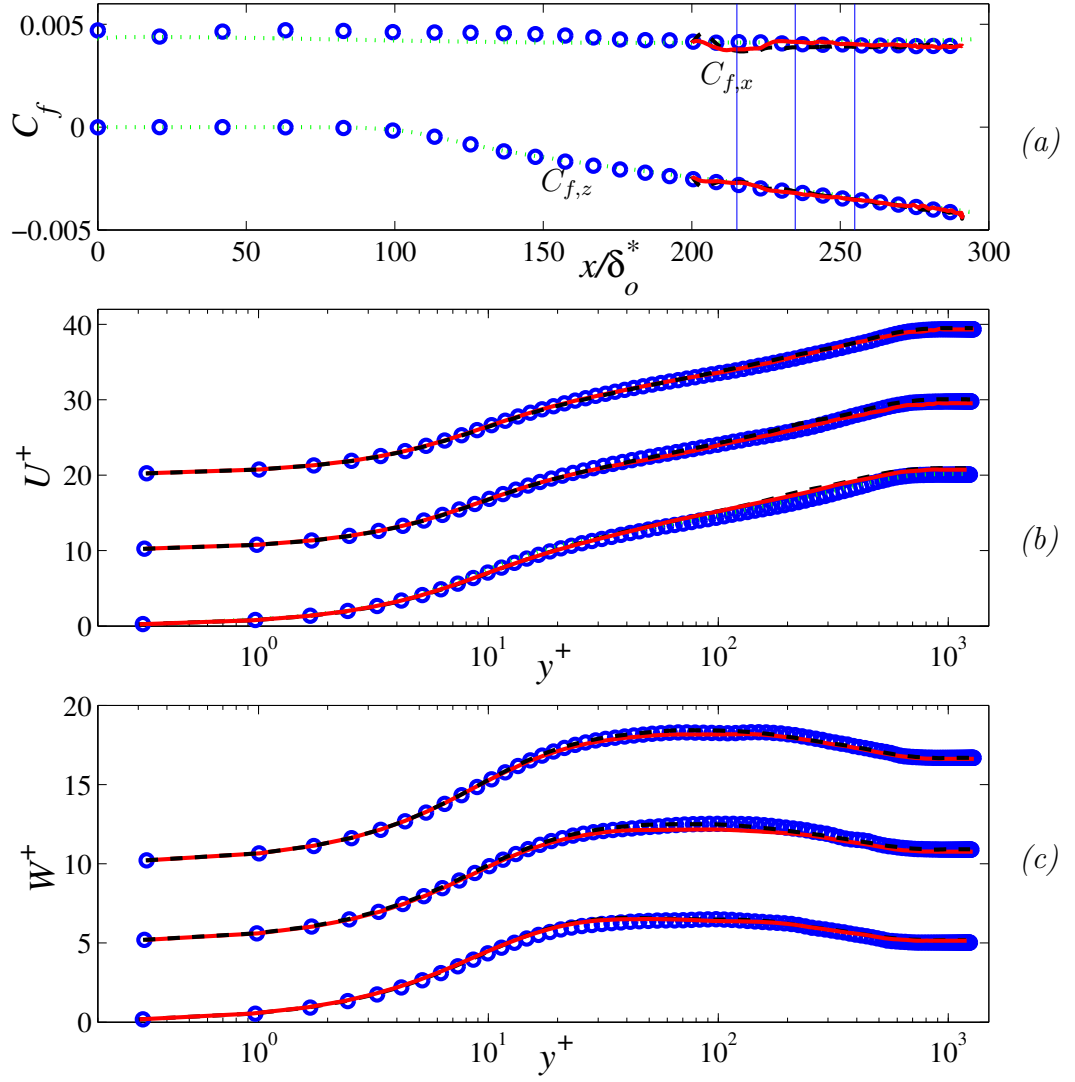


Figure 4.13: 3D boundary layer. (a) Streamwise and spanwise skin friction coefficients, $C_{f,x}$ and $C_{f,z}$; (b) mean streamwise velocity profiles and (c) mean spanwise velocity profiles at the locations indicated by a vertical line in part (a). \circ Reference LES; \cdots SA RANS; $---$ error based on $\langle u'v' \rangle$; $—$ production-based error.

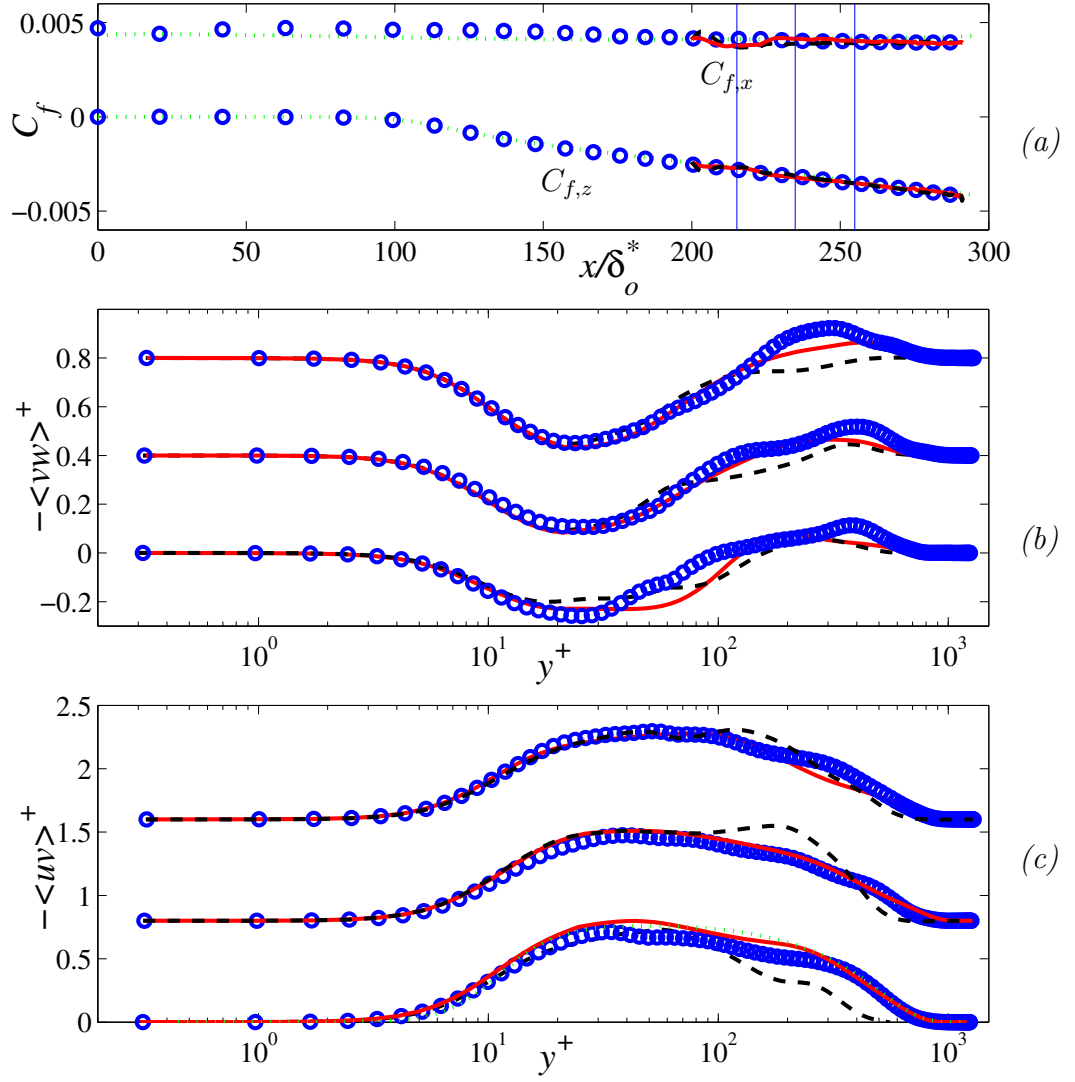


Figure 4.14: 3D boundary layer. (a) Streamwise and spanwise skin friction coefficients, $C_{f,x}$ and $C_{f,z}$; (b) secondary shear stress $\langle v'w' \rangle$ and (c) principal shear stress $\langle u'v' \rangle$ at the locations indicated by a vertical line in part (a). \circ Reference LES; \cdots SA RANS; $---$ error based on $\langle u'v' \rangle$; $---$ production-based error.

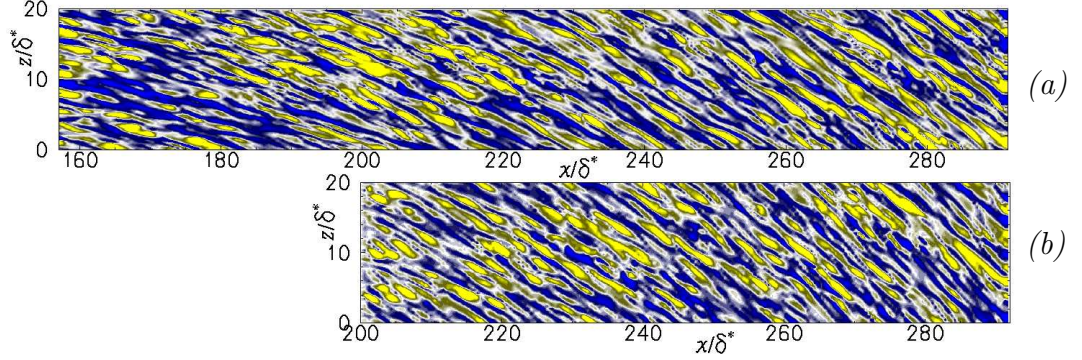


Figure 4.15: Contours of streamwise velocity fluctuations in a xz -plane at $y/\delta_o^* = 0.18$. (a) Reference LES (only part of the domain is shown); (b) hybrid RANS/LES.

downstream of the inflow. The principal shear stress, $\langle u'v' \rangle$ and the secondary ones $\langle v'w' \rangle$ develop quite rapidly as is shown in 4.14. Notice that by adding the forcing into the v equation we amplify the production of the secondary stress, $\langle v'v' \rangle \partial W / \partial y$, as well as that of $\langle u'v' \rangle$.

Figure 4.15 shows streamwise velocity fluctuations in a plane parallel to the wall. We observe again a very rapid build-up of the streaky structure starting from the synthetic turbulence.

4.2 Conclusions

In this Chapter we show further validation of the controlled-forcing method for turbulence generation at RANS/LES interfaces. The method has shown itself to be robust and efficient. By studying the zero-pressure-gradient boundary layer (which, despite its simplicity is one of the most challenging cases examined) we developed

guidelines for the determination of the parameters of this method. Perhaps the most important parameter is the length of the averaging used to determine the computed Reynolds stresses in the definition of the error (3.1) or (4.1).

Of the flows examined, we found the zero-pressure-gradient and favorable-pressure-gradient boundary layers to be the most challenging: in the zero-pressure-gradient case no external mechanism amplify the instability of the flow, so that the generation of turbulence is entirely due to the synthetic turbulence and controlled forcing; since the latter is less effective in the outer layer (where the turbulence production mechanisms are weaker), we observe the slow development of the outer layer. The favorable-pressure-gradient boundary layer presents a different set of problems: The acceleration results in relaminarization of the flow. Therefore, the injection of energy due to the forcing drives the flow in the wrong direction. In addition, RANS models are not very accurate in the strong acceleration region, which results in three sources of error: first, the mean velocity at the interface is far from the result obtained with the full-domain LES. Second, the target stresses are not close to the “correct” ones; thus, the controller drives the solution towards an incorrect one. Finally, the time-scale obtained from the RANS is substantially different from that obtained from the reference calculation, so that the moving average is suboptimal.

The method worked well in the adverse-pressure-gradient case, in which the deceleration (and, to an even greater extent, the separation) amplifies the distur-

bances, thus aiding the generation of turbulent eddies. This result is consistent with the findings of Terracol [25], who had some success using synthetic turbulence generation in the adverse-pressure-gradient region on the suction side of a turbine blade. In the 3D boundary layer the turning of the streamline imposed by the spanwise pressure gradient drives the lateral flow, with secondary stresses that develop from nearly zero at the RANS/LES interface. The controller proves to be able to seed the turbulence enough that the growth of the secondary stresses, and hence the lateral mean velocity profile, can be predicted accurately.

In summary, we have shown that the controlled forcing method is robust and efficient. The least favorable results are obtained in mildly unstable flows like the ZPG pressure gradient, or in re-laminarizing ones. Even in these situations, within 5 boundary layer thicknesses of the end of the control region a realistic flow was established. In realistic applications, especially in curved flows and in adverse pressure gradients (an important class of applications) the controlled forcing gives very rapid development of realistic eddies.

Chapter 5

Favorable pressure gradient boundary layer

5.1 Introduction

Turbulent boundary layers subjected to a favorable pressure gradient (FPG) (*i.e.*, one that results in freestream acceleration) are common in many engineering applications, such as airfoils and curved ducts. While the canonical zero-pressure-gradient (ZPG) boundary layer is relatively well understood, FPG boundary-layers are less well known. The simplest case of an accelerating boundary layer is the “sink flow”, in which the acceleration parameter $K = (\nu/U_\infty^2)dU_\infty/dx$ is constant with the streamwise distance x . This flow has been studied experimentally and numerically; it is known that, for strong acceleration ($K > 3 \times 10^{-6}$) turbulence cannot be maintained, and the flow re-laminarizes. The sink flow is, of course, an idealization: in real cases, a large acceleration parameter cannot be sustained for long distances, and, in practical applications, a region of FPG and streamwise acceleration is followed by one with constant or adverse pressure gradient (such is the case for the flow on an airfoil downstream of maximum thickness). In these conditions, full re-laminarization may not occur, and the pressure gradient may leave the flow in a “laminarescent” [83] state. As the pressure gradient is removed,

the flow may then return to a turbulent state; the re-transitioning process may be strongly affected by the state of the turbulence at the end of the acceleration region.

For these reasons it is important to understand the mechanisms of relaminarization. Reviews of current knowledge can be found in several articles by Narasimha and Sreenivasan [84, 85] and by Sreenivasan [83]; here, only the main findings are summarized. Re-laminarization can be caused by three mechanisms: (1) a decrease in the Reynolds number accompanied by an increase in the viscous dissipation; (2) stratification or flow curvature, or (3) flow acceleration. Experimental investigations of re-laminarization due to flow acceleration started in the early 1960s. Wilson [86] found the first evidence that the flow did not follow the semi-empirical theories for a fully turbulent boundary layer: the measured heat-flux rates on a convex surface of a blade were considerably lower than the predicted values. Wilson [86] conjectured the possibility of a “reverse transition” of the flow due to the low local value of the Reynolds number. However, Patel and Head[87] later observed that there is no explicit correlation between a low Re and the relaminarization process, as long as the initial Re is high enough to allow the turbulence to be self-sustained.

Senoo [88] studied the boundary layer on the end-wall of a turbine nozzle cascade; he found that it was laminar in the region of the throat, while the upstream layer was turbulent. His findings did not explain the phenomenon of relaminarization. Moreover, the effects of secondary flow were not clear in his study.

Studying a similar configuration, Launder [89, 90] observed that relaminariza-

tion of the flow, at least in terms of macro-scale properties and integral parameters, starts near the end of the acceleration region. In the upstream region, the boundary layer was found to be turbulent but with a departure from the universal law of the wall. Only further downstream the boundary layer became close to the laminar state. Moreover, he documented an increase of the energy at low wave-numbers in the near-wall region and an even more pronounced one in the outer part of the boundary layer. He found an explanation of that energy shift in the time-lag between inner and outer regions: the latter is relatively distant from the turbulence production peak, so the eddies in that region are not fast enough to adjust their frequency as the free stream is accelerated. He, therefore, proposes a picture in which the flow dynamics are completely dominated by the near wall region. Launder [89, 90] also observed that the turbulence does not vanish, but an increasing fraction of it plays a passive role in the boundary-layer development. Because of this inability of turbulent structures to adjust to the flow acceleration and the rapid increase of momentum, the viscous stresses grow larger than the turbulent ones; consequently, the dissipation exceeds production, leading to a decay of turbulence and to laminarization. However, Badri-Narayan *et al.* [91] found that dissipation never exceeds production in an accelerated boundary layer, and that both production and dissipation decrease.

Kline *et al.* [92] found a correlation between the drastic drop of eruptions in the buffer layer and the acceleration parameter K : for K that approach the value of

$K_{\max} \approx 3.5 \times 10^{-6}$ the burst rate tended to zero. Narasimha and Sreenivasan [85] suggested that the bursting frequency decreases exponentially in an accelerated boundary layer before the flow relaminarizes, but never goes to zero completely.

Patel and Head [87] showed a strong correlation between the distribution of the shear-stress gradient near the wall and the relaminarization. They defined a non-dimensional shear-stress-gradient parameter, and they inferred the onset of relaminarization from the position where this parameter has a minimum value of -0.009 . However, Narasimha and Sreenivasan [85] observed that this non-dimensional parameter reaches that value before the turbulent boundary-layer actually reverts to a laminar-like state; in this sense, the Patel and Head [87] parameter predicts deviation from the universal law for ZPG boundary layers, but not necessarily relaminarization.

Blackwelder and Kovasznay [93] noted an increase of the Reynolds stress and turbulent kinetic energy (TKE) along streamlines in the outer part of the boundary layer as the flow was accelerated. In the inner layer, on the other hand, they found a decrease of those quantities along streamlines. Moreover, they studied the space-time correlations of the large structure in the outer layer. They found no change compared to the ZPG case for the uu correlations; this suggested that the acceleration had no strong effect on the large streamwise structure (those close to the boundary-layer edge). On the other hand, they noted a drastic change of the normal velocity component of the outer-layer structures, as the vv correlations lost

the anti -symmetrical part found in the ZPG case.

Narasimha and Sreenivasan [84] point out that relaminarization is the result of the domination of pressure forces over the slowly responding Reynolds stresses in the outer layer, and the generation of a new laminar sub-layer that is maintained stable by the acceleration. In their model the turbulent structures in the outer layer are only distorted and not destroyed by the rapid acceleration. The new sub-layer and the distorted outer layer do not interact, but they only provide the appropriate boundary conditions to each other. Rapid distortion theory could be applied in the outer part to predict the turbulence intensities there, but the interior part of the layer was not well understood and the wall-normal components were not well predicted. In the same period, Falco [94] performed a smoke-visualization study, and suggested that in the relaminarization process large scale structures existed upstream of the contraction that accelerates the flow: the boundary layer in the later stages of the acceleration is dominated by an array of large scale streamwise vortices; thus, an inner-outer layer interaction could exist and the relaminarization seems to begin from the outer region with a strong coupling between inner and outer parts. This visual observation was reconfirmed by Ichimiya *et al.* [95], who conjecture that non-turbulent fluid on the outside of the boundary layer penetrates near the wall, so that the beginning of relaminarization is due to the outer region together with the change in ejection-sweep phenomena.

Recent experimental studies of FPG boundary layers have been performed by

Fernholz and Warnack [96] and by Warnack and Fernholz [97]. Their measurements showed that the Reynolds number had little effect on the relaminarization, and the pressure-gradient effects were dominant. They found a strong increase in the anisotropy of the normal Reynolds stresses (which decreased) in the outer region of the boundary layer, but observed the opposite effect in the inner layer. By calculating the integral length-scales, they found that the near-wall vortices are stretched in the streamwise direction, but are only slightly smaller in the wall-normal direction. They measured high levels of flatness of the instantaneous skin friction coefficient, which indicated the presence of intermittent high-frequency bursts in the re-laminarizing flow.

Other recent experiments by Escudier *et al.*[98] found that the streamwise RMS velocity in the inner layer scales with the local freestream velocity, while in the outer layer it is “frozen” (*i.e.*, remains relatively constant) in the accelerated region. They inferred that the frequency content of the turbulence was only changed at the highest frequencies, and that the bulk of the turbulence generated in the thick upstream boundary layer prior to acceleration was at frequencies too low to cause significant Reynolds stresses within the accelerated boundary-layer.

Numerical calculations of a boundary layer with variable acceleration parameters (as opposed to the sink flow studied by Spalart [34]) were carried out by Piomelli *et al.* [99], who examined the effect of the acceleration on the near-wall vortical structures. They observed that the near-wall streaks became more elon-

gated and showed fewer undulations. Since they found that the vorticity levels in the acceleration region were similar to those in the zero-pressure gradient (ZPG) boundary-layer, and that the vortex scales in the cross-plane were unchanged, they suggested that the additional vortex-stretching due to the streamwise velocity gradient must be counterbalanced by other mechanisms. However, from the results presented, it was unclear which physical phenomena provide this balance.

The mechanisms involved in the relaminarization of the turbulent boundary layer in an FPG are still poorly understood. What is clear, however, is that the turbulence in the outer layer remains frozen through the acceleration, and is, therefore, strongly dependent on the conditions of the upstream boundary layer (*i.e.*, neither on the local near-wall behavior nor on the local freestream velocity). Closer to the wall, the flow undergoes a process of laminarization, in which the skin friction coefficient drops sharply. Finally, after the acceleration is completed, the flow quickly re-transitions to an equilibrium boundary layer. Several questions are still open; among them are: (1) Does the outer layer turbulence play a part in the relaminarization phenomenon? (2) How do the inner and outer layers interact during and after the acceleration? (3) How does the re-transition to turbulence takes place (and why does it take place so abruptly)?

In an attempt to clarify at least the first of these points, large-eddy simulations (LES) of boundary layers in FPG are performed with different acceleration parameters. The first simulation, which matches the high-acceleration experiment

of Warnack and Fernholz [97] ($K_{\max} \approx 4 \times 10^{-6}$) (where $K = (\nu/U_\infty^2)(dU_\infty/dx)$ is the acceleration parameter), shows a substantial reduction in turbulent kinetic energy production, and the flow becomes laminar-like in the acceleration region. A second simulation is performed at a lower acceleration ($K_{\max} \approx 3 \times 10^{-6}$) (obtained by scaling down the high- K case) resulting in less of a “laminar-like” behavior in the acceleration (for comparison, on a 0.3m-long NACA0012 airfoil at $Re = 1.5 \times 10^6$, K has values of the order 3×10^{-6} in the region between 2% of the chord and the point of maximum thickness).

In the following we will present the numerical approach employed. Then will show results of the simulations, including statistics and flow visualizations; we will describe the results of some numerical experiments in which the flow was artificially altered, to isolate the structures responsible for the re-transition. Finally, we shall draw some conclusions.

5.2 Problem formulation

In this study we perform large-eddy simulations (LES) of a flat-plate boundary layer in the presence of an accelerating freestream. Most experimental measurements in FPG boundary layer are performed on a flat surface in which the pressure gradient is imposed through contouring of the opposite wall of the wind-tunnel, or by including a contoured body above the flat wall to produce the desired acceleration

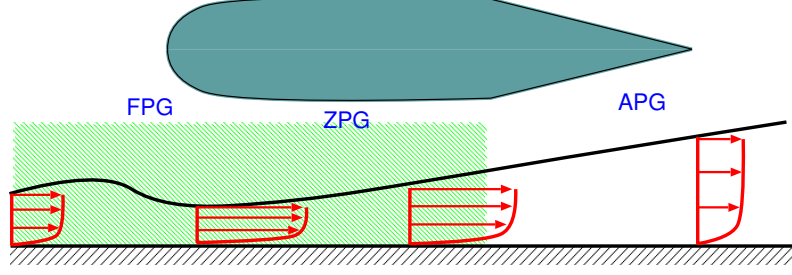


Figure 5.1: Sketch of the configuration. The computational domain is shown as a hatched area.

(Figure 5.1). In our case we imposed directly a variable freestream velocity¹ $U_\infty(x)$ on the top boundary of the domain [102]. The other two velocity components were obtained by requiring that the vorticity in the freestream is zero. An unsteady inflow boundary condition was obtained from a separate simulation that used the recycling/rescaling method [102], while a convective outflow boundary condition was used at the downstream boundary.[82] Periodic conditions were used in the spanwise direction.

The simulations were performed on a domain of size $476\delta_o^* \times 20\delta_o^* \times 20\delta_o^*$ (in the streamwise, wall-normal and spanwise directions, respectively), using $1136 \times 104 \times 192$ grid points for the high-acceleration case, and $1024 \times 64 \times 128$ grid points for the low-acceleration one. The results obtained using this resolution compare well with coarser calculations. The Reynolds number, based on freestream velocity at the inflow, U_o , and on the displacement thickness at the inflow, δ_o^* , is 1,260.

¹In the following, U_∞ denotes the (variable) freestream velocity, whereas $U_o = U_\infty(0) = 1$ is the reference velocity for the flat-plate region upstream of the FPG region.

The equations of motion were integrated for $3171\delta_o^*/U_o$ time units. Statistical data were obtained by averaging over the last 2415 time units, and over the spanwise direction. In the following, time-averaged quantities are denoted by angle brackets, and fluctuating ones by a prime.

5.3 Results

In the present investigation we studied two cases: one with high-acceleration, another with lower acceleration. Figure 5.2(*a*) shows the freestream velocity, U_∞/U_o , and the resulting friction velocity $u_\tau/u_{\tau,o}$ for the two cases of high and low acceleration. Figure 5.2(*b*) shows the acceleration parameter, K . In the case of high K , the freestream velocity at the outflow is almost three times that at the inflow.

The momentum-thickness Reynolds number $Re_\theta = U_\infty\theta/\nu$, with

$$\theta = \int_0^\infty \frac{U}{U_\infty} \left(1 - \frac{U}{U_\infty}\right) dy \quad (5.1)$$

(where $U = \langle \bar{u} \rangle$) is shown in Figure 5.2(*c*); Re_θ decreases as the flow begins to accelerate ($x/\delta_o^* > 140$). This reflects profound changes in the velocity profile, which result in significant decrease of θ and will be discussed further later. The skin-friction coefficient is shown in Figure 5.2(*d*). Again, it can be observed that, although the mean freestream velocity increases in both cases, C_f begins to decrease near the location of maximum K (this decrease begins to occur downstream of the corresponding decrease in Re_θ). After the pressure gradient is relaxed, rapid re-transition towards an equilibrium turbulent value occurs ($x/\delta_o^* \simeq 310$). The chain-dotted line shows the

equilibrium ZPG value of C_f obtained from the correlation [104] $C_f = 0.0576 Re_x^{-0.2}$. At the inflow, while the computations show good agreement with the experimental correlation, the experiments have lower skin friction, suggesting that pressure gradient effects are already significant on the upstream boundary layer. The region of relaminarization is predicted well by the LES. The re-transitioning occurs more abruptly than in the experiment, and the downstream C_f is higher in the LES, even taking into account the initial shift. Several factors can account for this difference. First, the different geometry: in the experiment the measurements are made on the inside wall of a cylinder, whereas the calculation uses a flat plate [94]; the ratio between cylinder radius and boundary-layer thickness varies between 12 and 9, so curvature effects may play a role. Furthermore, despite the fact that the grid in the streamwise direction was refined in the re-transition region, the three-fold increase in the friction velocity results in marginal resolution of the boundary layer in the fully turbulent region downstream of the acceleration: in the upstream region we have $\Delta x^+ \simeq 28$, $\Delta z^+ \simeq 6.2$, while in the recovery region $\Delta x^+ \simeq 56$ and $\Delta z^+ \simeq 19$.

The lower acceleration case shows similar behavior to the high-acceleration one; however the re-laminarization is less severe. Re_θ and C_f are reduced by a much smaller amount in the acceleration region, and recovery takes place earlier than for the high- K case.

Figure 5.3 shows the mean velocity profiles in outer coordinates at several locations in the flow. If the velocity profiles are plotted in wall coordinates (Figure 5.4),

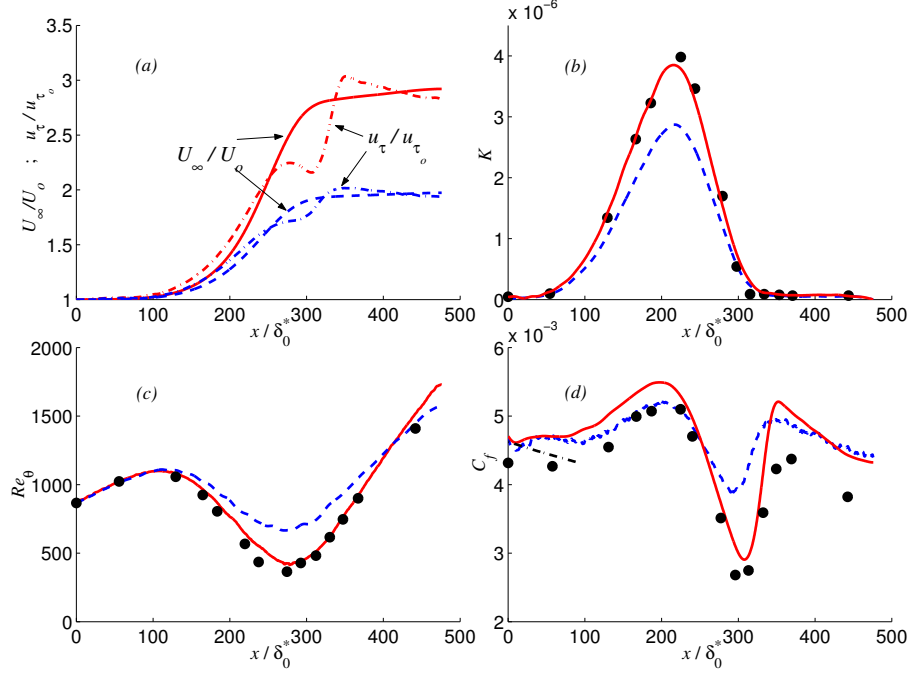


Figure 5.2: Streamwise development of statistical quantities. (a) Freestream velocity, U_∞/U_o and friction velocity $u_\tau/u_{\tau,o}$; (b) Acceleration parameter K ; (c) Momentum-thickness Reynolds number Re_θ ; (d) Skin friction coefficient C_f . • Experiments [97]; — high- K case; - - low- K case; - · - ZPG boundary-layer correlation.

one can observe the existence of a logarithmic layer (following the standard law, $U^+ = 2.5 \log y^+ + 5$) at the inflow and in the mild acceleration region ($x/\delta_o^* < 150$). As the FPG becomes significant, the slope of the logarithmic region decreases (a well-known effect of acceleration [34]). The two cases are in good agreement up to the point of maximum K . Thereafter, the high- K case departs significantly from the equilibrium boundary layer profile, becoming more laminar-like. The recovery

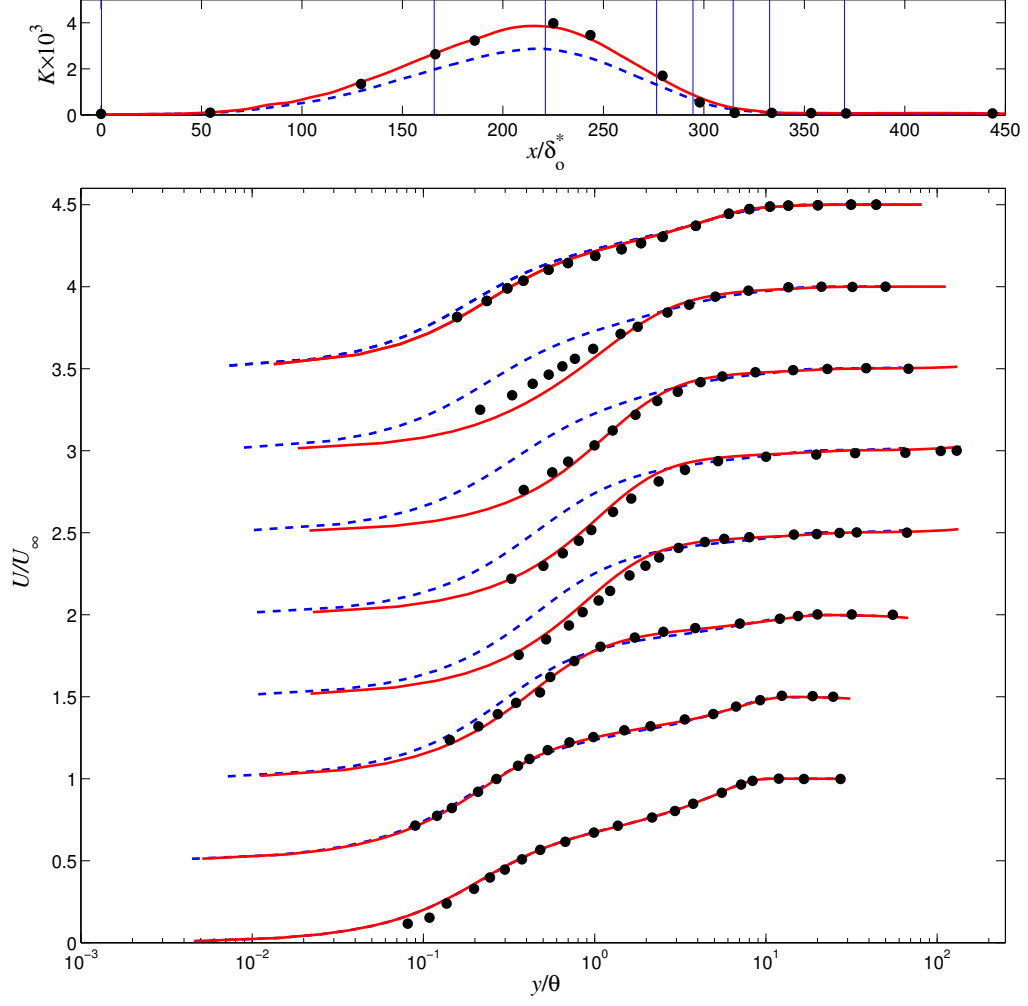


Figure 5.3: Wall-normal profiles of the mean streamwise velocity at the locations shown in the top figure. • Experiments [97]; — high- K case; - - low- K case. Each profile is shifted by 0.5 units for clarity

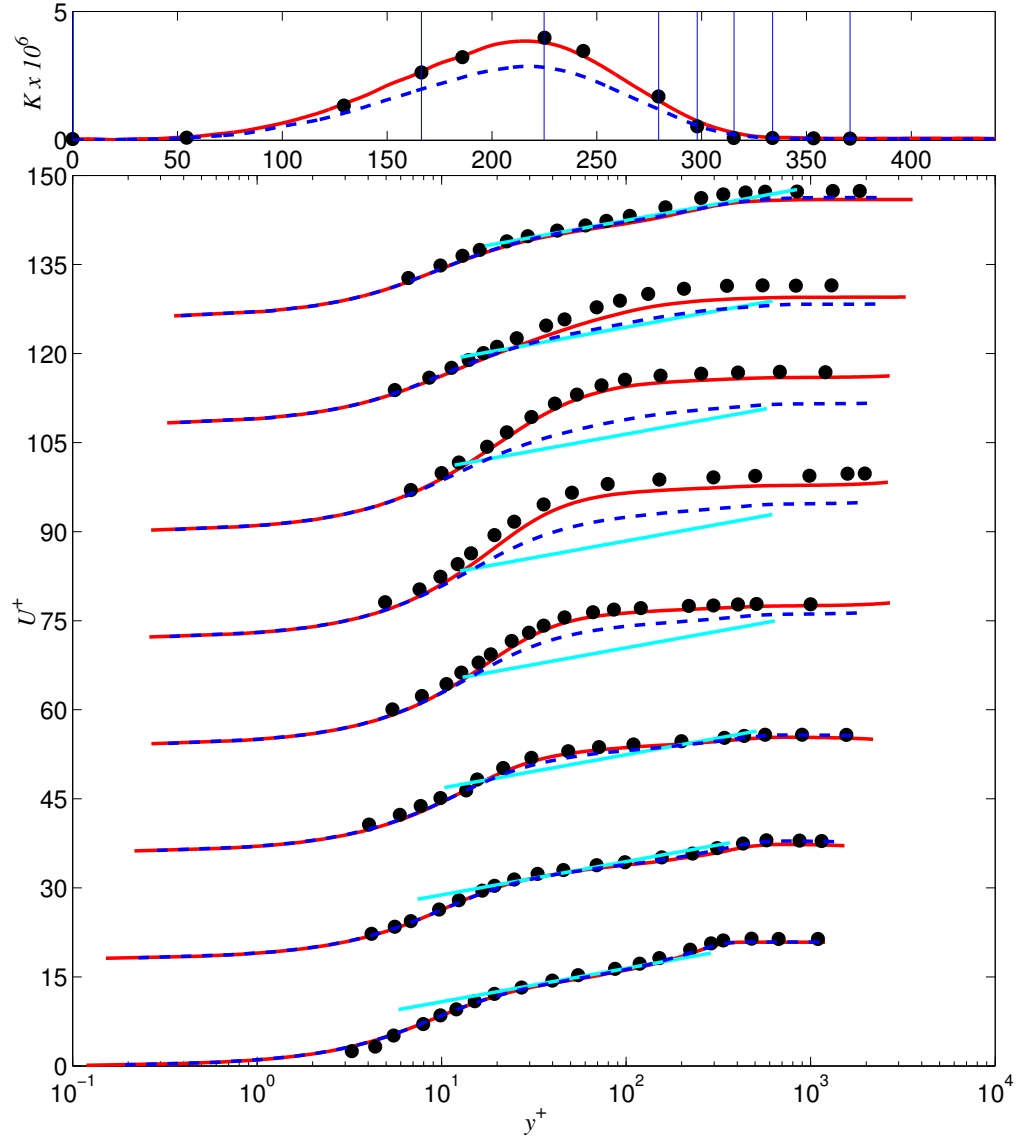


Figure 5.4: Wall-normal profiles of the mean streamwise velocity in inner coordinates at the locations shown in the top figure. • Experiments [97]; — high- K case; - - - low- K case; — $U^+ = 2.5 \log y^+ + 5$. Each profile is shifted by 18.0 units for clarity

of the inner layer to an equilibrium logarithmic law occurs quite rapidly, between $x/\delta_o^* \simeq 330$ and 370. The agreement with the experimental data is very good. One should observe that in the region of high acceleration there is a significant region of well-mixed fluid, in which the normal velocity gradient is nearly zero (from $y/\theta > 5$ at $x/\delta_o^* = 320$, for instance).

Very good agreement is also observed in the prediction of the normal Reynolds stresses (Figure 5.5). The decrease of the magnitude of the stresses following the maximum of the acceleration is evident, and is due to the increase of u_τ^2 , which is used to normalize the stresses, rather than to a decrease of the stresses themselves, which remain approximately equal to their upstream value (see the discussion below).

Figure 5.6 shows the Reynolds stresses in inner units; again, there is very good agreement with the experimental results. The Reynolds stresses decrease significantly in the region where K has the maximum value. In many cases flow relaminarization is due to decorrelation between the wall-normal and the streamwise fluctuation, which remain significant but do not contribute to the Reynolds shear stress. In this flow, the cause of the decrease of $\langle u'v' \rangle$ appears to be different. Figure 5.7 shows contours of the normal Reynolds stresses $\langle u'u' \rangle$ and $\langle v'v' \rangle$, of the shear stresses $\langle u'v' \rangle$, and of the correlation coefficient

$$C_{uv} = \frac{\langle u'v' \rangle}{(\langle u'u' \rangle \langle v'v' \rangle)^{1/2}} = \frac{\langle u'v' \rangle}{u_{rms} v_{rms}}. \quad (5.2)$$

From this figure it appear that, while the correlation coefficient decreases significantly around $x/\delta_o^* \simeq 300$, the decrease of the v' fluctuations is much more dramatic.

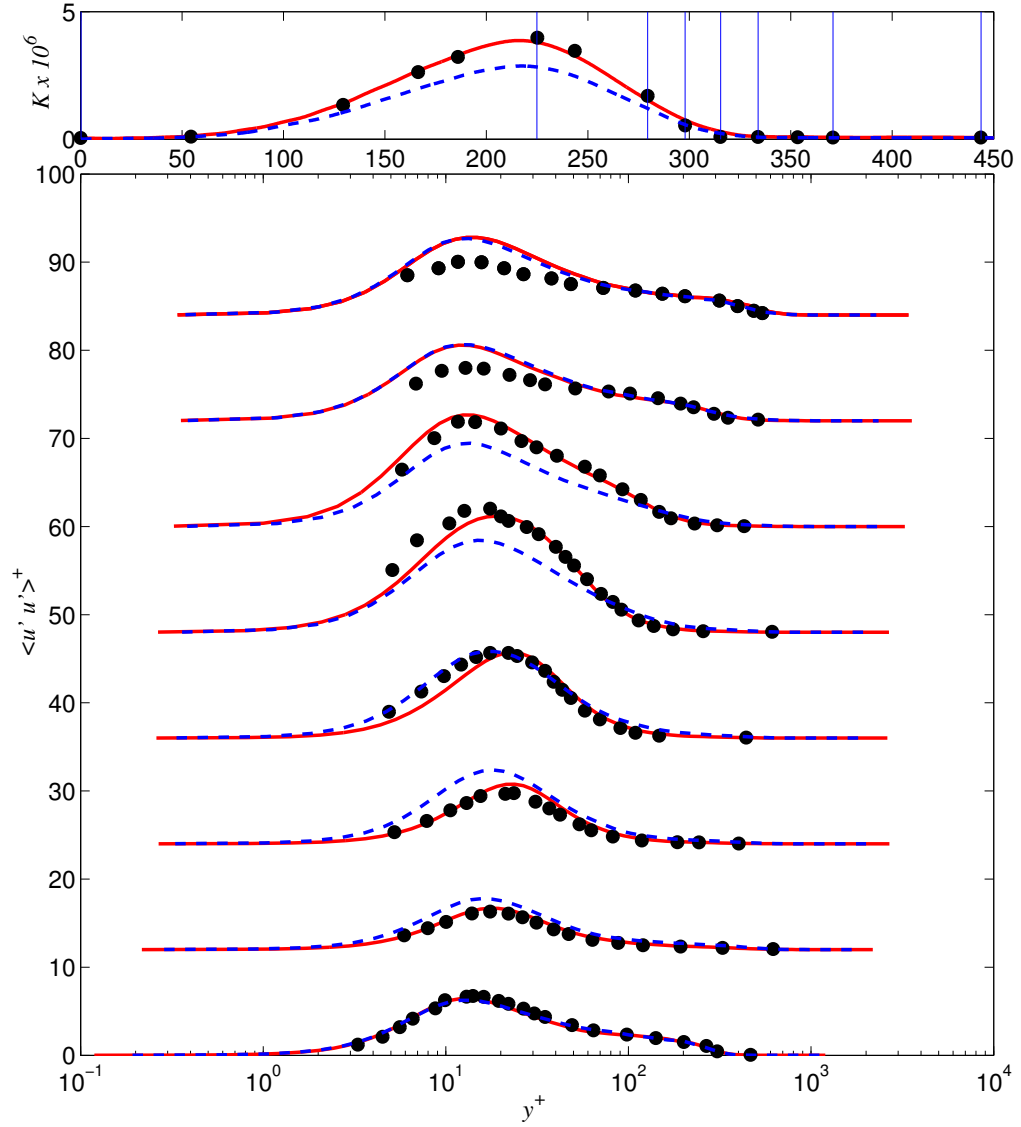


Figure 5.5: Wall-normal profiles of the streamwise Reynolds stresses at the locations shown in the top figure. • Experiments [97]; — high- K case; - - low- K case. Each profile is shifted by 12.0 units for clarity

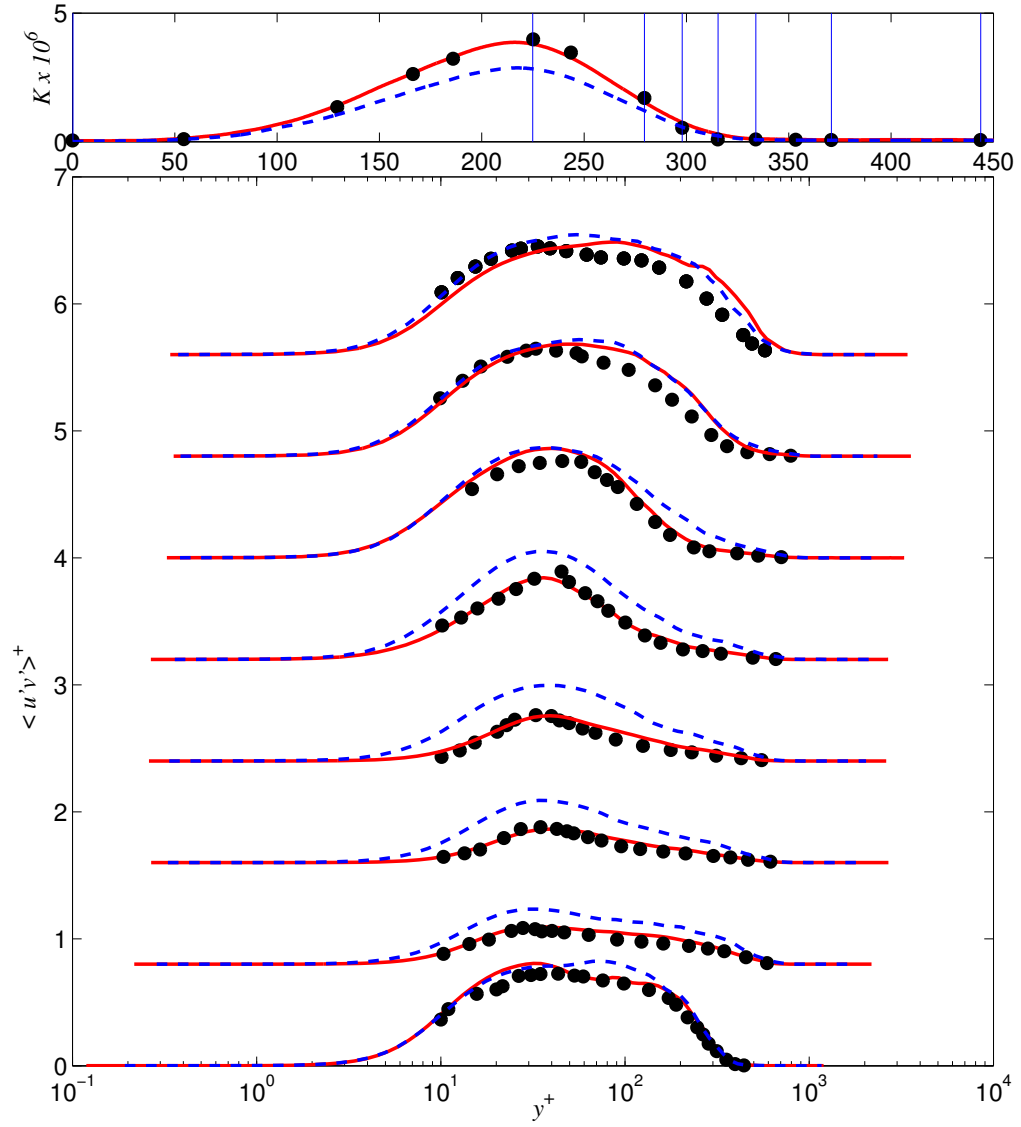


Figure 5.6: Wall-normal profiles of the Reynolds shear stresses at the locations shown in the top figure. • Experiments [97]; — high- K case; - - low- K case. Each profile is shifted by 0.8 units for clarity

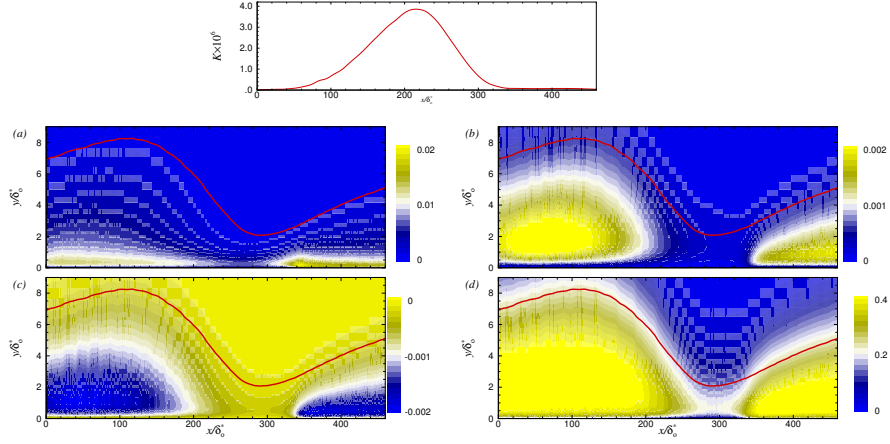


Figure 5.7: Contours of averaged quantities for the high- K case. The red line shows the local boundary layer thickness δ_{99} . (a) $\langle u'u' \rangle / U_\infty^2$; (b) $\langle v'v' \rangle / U_\infty^2$; (c) $\langle u'v' \rangle / U_\infty^2$; (d) $C_{uv} = \langle u'v' \rangle / u_{rms} v_{rms}$.

The same phenomenon is better illustrated in Figure 5.8. Here, we identified four streamlines (one in the outer layer, two in the logarithmic region and one in the buffer layer), and plot the streamwise development of the Reynolds stresses along each streamline. This method allows one to account for the significant thinning of the boundary layer in the high-acceleration region, and for its subsequent thickening in the re-transition region.

Focusing our attention first on the streamwise stresses, $\langle u'u' \rangle / U_o^2$ (Figure 5.8(b)), we observe that in the outer layer their level is essentially frozen (*i.e.*, they remain constant and equal to their upstream value) until a location well after the maximum acceleration point ($x/\delta_o^* \simeq 300$). They then begin to increase, an increase that occurs later for the streamline located farther away from the wall. Along the

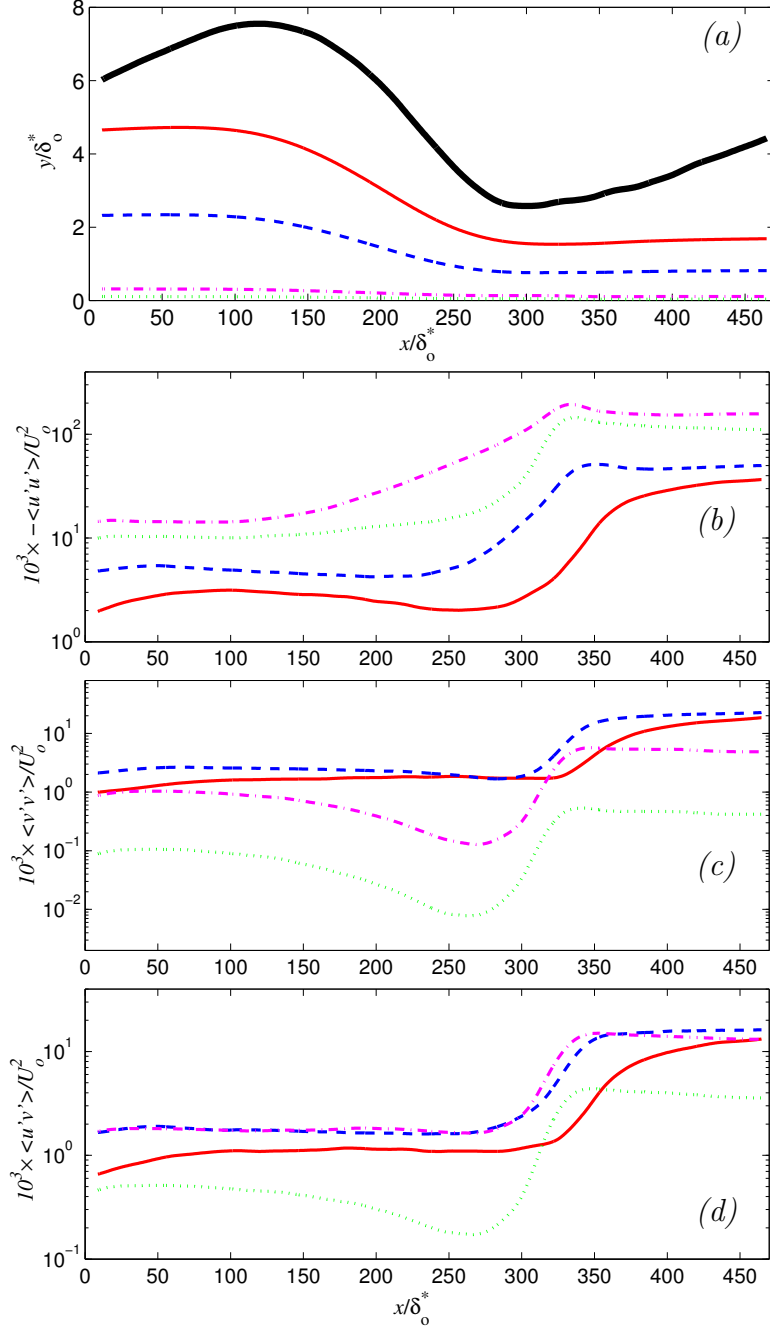


Figure 5.8: Development of the Reynolds stresses along selected streamlines. (a) Streamline coordinates; (b) $\langle u'u' \rangle / U_o^2$; (c) $\langle v'v' \rangle / U_o^2$; (d) $\langle u'v' \rangle / U_o^2$. The thick black line corresponds to the boundary-layer edge. Streamline originating in: — outer-layer; — middle boundary layer; — log region; — viscous sublayer.

streamline in the buffer layer the increase in $\langle u'u' \rangle / U_o^2$ begins earlier, as soon as the freestream velocity begins to increase ($x/\delta_o^* \simeq 120$). A different behavior can be observed for the wall-normal stresses $\langle v'v' \rangle / U_o^2$ (Figure 5.8(c)): along the outer-layer streamlines the stresses also appear to be frozen to their upstream value. They begin to increase well after the peak acceleration, and also after the rise of the streamwise ones. Near the wall, on the other hand, we observe a significant decrease (by over one order of magnitude) of the wall-normal Reynolds stresses (consistent with the observations of Blackwelder and Kovasznay [93]) which is reflected in a similar decrease of the Reynolds shear stress $\langle u'v' \rangle / U_o^2$ (Figure 5.8(d)) in the buffer layer and in the viscous sublayer. In the logarithmic region, on the other hand, the increase in the streamwise fluctuation level balances the decrease of the wall-normal ones, resulting in constant shear stress until the recovery region (we will show later that the correlation coefficient does not vary very much in this region). Note that the data showed in this figure were normalized using the inflow freestream velocity, U_o , to emphasize advection effects. If one used either the local freestream velocity, U_∞ , or the friction velocity u_τ , which increase through the acceleration region, all these quantities would be observed to decrease through the region in which the pressure gradient is applied.

Figure 5.9 shows the structure parameter $a_1 = |\langle u'v' \rangle| / \langle u'_i u'_i \rangle$ and the correlation coefficient C_{uv} . The structure parameter is a measure of the efficiency of turbulence in extracting Reynolds shear stress from the available turbulent kinetic

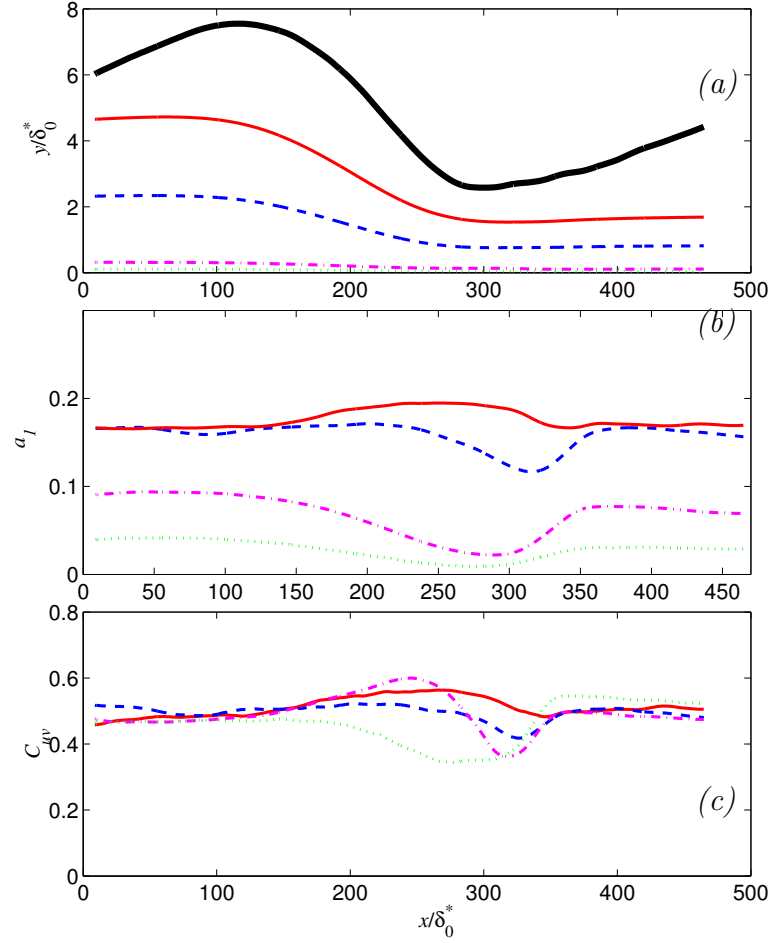


Figure 5.9: Development of a_1 parameter and correlation coefficient along selected streamlines. (a) Streamline coordinates; (b) a_1 ; (c) C_{uv} . The thick black line corresponds to the boundary-layer edge. Streamline originating in: — outer-layer; --- middle of the boundary layer; - - - logarithmic region; viscous sublayer.

energy and, in equilibrium flows, it has a value close to 0.15. The acceleration causes a significant departure from its equilibrium value: we observe a significant decrease of a_1 over the lower half of the boundary layer. The decrease is particularly strong in the logarithmic layer (the value of a_1 is lower in this region even in equilibrium ZPG boundary layers). The correlation coefficient C_{uv} , on the other hand, remains close to the canonical value for flat-plate boundary layers ($C_{uv} \simeq 0.4 - 0.5$) everywhere, with variations of less than 10%. Thus, the relaminarization does not seem to be due to so much to a decorrelation between the frozen fluctuations, but rather to a re-organization of the flow that results in much lower wall-normal fluctuations that, although reasonably well-correlated with the streamwise ones, can only produce a much reduced shear stress. The decreased mixing due to the turbulent transport, in turn, causes the decrease of the skin-friction coefficient that is considered one of the symptoms of relaminarization.

The significant changes to the turbulent statistics observed above must be accompanied by similar alterations of the turbulent structure, which we will now describe. The contours of streamwise velocity fluctuations in an xz -plane near the wall are shown in Figure 5.10. We can observe the regular streaky structure of the boundary layer near the inflow. In the region of high K we observe fluctuations of magnitude comparable to those in the equilibrium region; they form, however, very long streamwise streaks, without the kinks characteristic of the burst event. This indicates the change towards a very stable and more orderly inner layer, as pointed

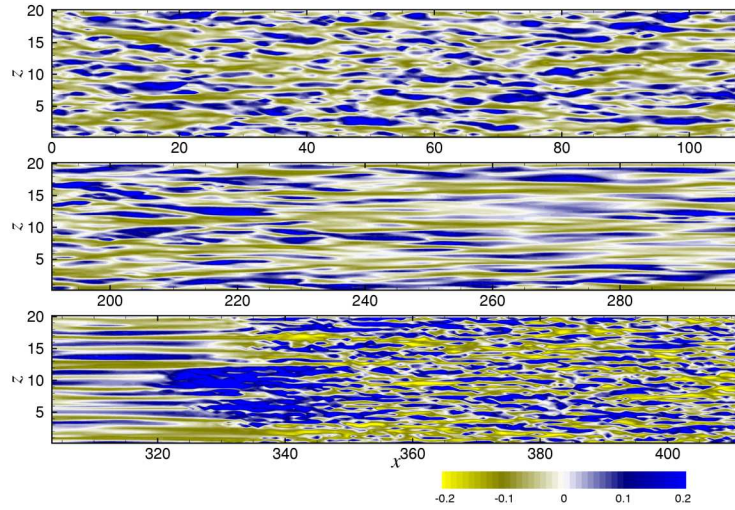


Figure 5.10: Instantaneous contours of u' velocity fluctuations in a plane parallel to the wall.

out by Narasimha and Sreenivasan [84]. Figure 5.10 also shows a fast re-transition to turbulence when the pressure gradient is turned off ($x/\delta_o^* \simeq 310$).

In Figure 5.11 the coherent structures in the outer layer are visualized through isosurfaces of the second invariant of the velocity gradient tensor

$$Q = -\frac{1}{2} \left(\frac{\partial u'_i}{\partial x_j} \frac{\partial u'_j}{\partial x_i} \right) \quad (5.3)$$

(see Dubief and Delcayre[105]). We note that the outer layer vortices become aligned in the streamwise direction in the acceleration region. This is most likely a kinematic effect, as the dominant component of the velocity gradient in this region, $\partial U/\partial x$, has the effect of stretching and re-orienting the coherent eddies into the streamwise direction. We note, however, that the more orderly structure of the flow observed in the inner layer (Figure 5.10) is reflected in a more orderly outer layer structure.

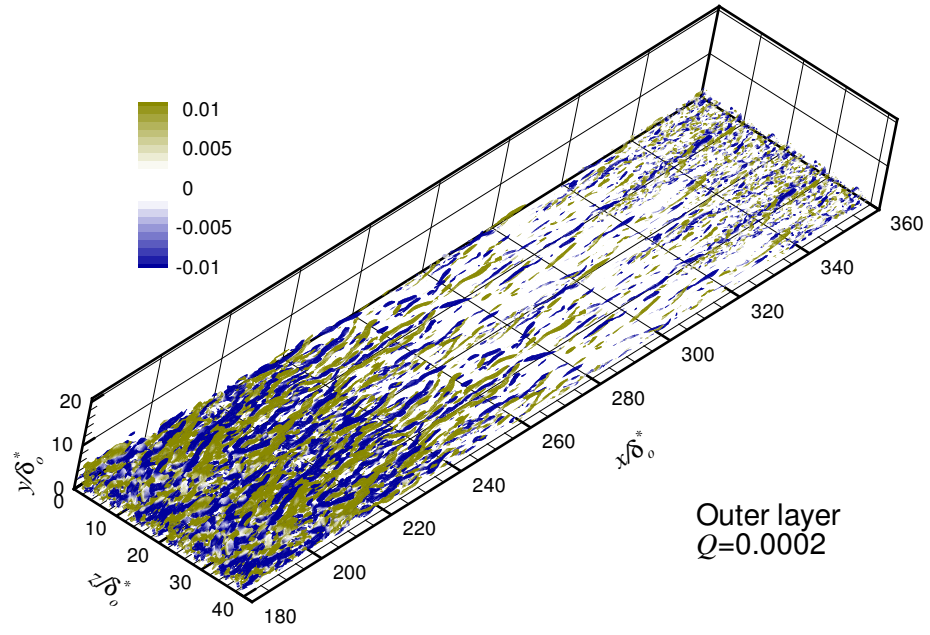


Figure 5.11: Instantaneous isosurfaces of $Q = -0.002$ in the outer layer colored by the streamwise vorticity.

An obvious question that needs to be addressed is whether the inner layer, with its reduced burst frequency, is unable to “scramble” the outer layer structures, or if the outer layer forces a more orderly inner-layer structure. The outer layer structures certainly affect the inner layer: Figure 5.12 shows contours of the instantaneous $u'v'$ correlation in planes normal to the mean flow, and secondary $(v-w)$ velocity vectors. One can observe that these vortices occur mostly in the well-mixed region mentioned above (the two thick lines that denote contours of $\bar{u} = 0.95U_\infty$ and $0.99U_\infty$ show the extent of this well-mixed region); they may, in fact, be responsible for it, as they induce vigorous motions of high-speed fluid towards the wall, and low-speed fluid outwards. Moreover, some of the motions induced by these large vortices result in significant values of the $u'v'$ correlation (at $x/\delta_o^* = 321$ and $z/\delta_o^* = 11$, or at $x/\delta_o^* = 260$ and $z/\delta_o^* = 4$, for instance).

5.4 Conclusions

We performed LES of the flow in an accelerating boundary layer, using two different levels of acceleration. The low-acceleration case remains in quasi-equilibrium, with a logarithmic law observed through most of the flow (albeit with decreased slope). The high-acceleration case results in relaminarization and re-transition of the flow. The computed statistics are in good agreement with the experimental data [96], which gives us confidence that the LES can be used to study the physics of this complex flow.

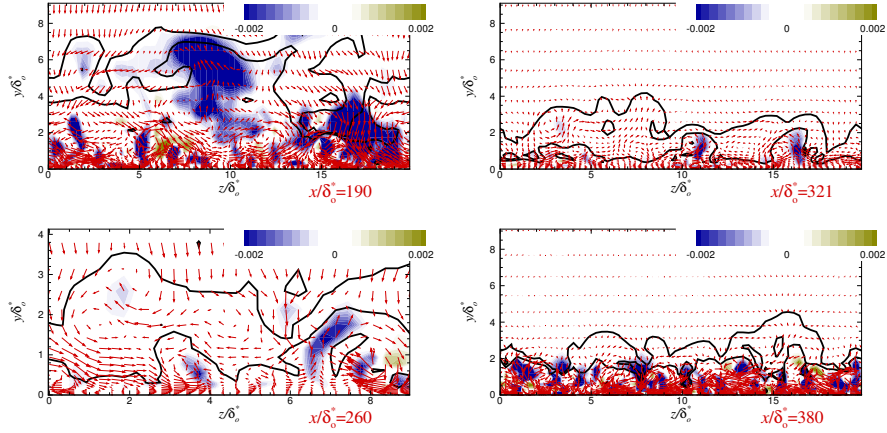


Figure 5.12: Contours of instantaneous $u'v'$ correlation in planes normal to the mean flow, and secondary $(v - w)$ velocity vectors. The two solid lines represent contours of $U/U_\infty = 0.95$ and 0.99 .

Examining the flow development along streamlines we observe that in the outer layer the turbulent fluctuations appear to be largely frozen to their initial state, and the flow is dominated by advection. A notable feature of the flow is that the correlation coefficient C_{uv} does not decrease very significantly. The decrease of the Reynolds shear stresses that is observed is mostly due to the damping of the wall-normal fluctuations.

We observed changes in the turbulent structures both in the inner and in the outer layers. The acceleration affects the outer-layer eddies by changing their structure and shape; in particular, large coherent structures are formed that are oriented in the streamwise direction. This results in the formation of a well-mixed outer layer, in which the turbulence production is decreased, and the turbulence

advected from upstream remains frozen. The inner layer is also affected: because of the strong acceleration, the flow becomes more orderly, with longer, more two-dimensional streaky structures and decreased frequency of bursts. However, a fast re-transition to turbulence is observed as soon as the applied pressure gradient is negligible. This may be due to the coherent structures in the outer part of the flow that trigger the re-transition to turbulence.

Two possible scenarios can explain the flow behavior: one, which matches the results of Blackwelder [93], Launder [89, 90], Narasimha and Sreenivasan [84], and Sreenivasan[83], is that the inner layer is made stable by the pressure gradient, and the turbulence in the outer layer remains relatively high and “frozen”: once the stabilizing influence of the pressure gradient is removed, transition occurs very rapidly, following a process that resembles bypass transition due to high freestream turbulence. A different picture was conjectured by Falco [94] and later by Ichimiya *et al.* [95]: the relaminarization seems to begin from the outer region with a strong coupling between inner and outer parts. The outer layer structures could induce strong incursions of more quiescent, outer-layer fluid into the wall region, and strong ejections of inner-layer fluid into the outer flow. Our data show that both of these mechanisms are present. Additional work is required to determine which of them is dominating.

Chapter 6

Conclusion and future work

6.1 Hybrid RANS/LES

This work shows that a PI feedback control applied to the Navier-Stokes equations accelerates the adjustment of synthetic turbulence generated at the inflow plane towards well-resolved LES turbulence. It has been proved that the PI control is stable and robust with different non-equilibrium flows. In this Chapter we summarize the major findings.

6.1.1 Control parameters

The averaging window used to determine the error, T_{ave} , has a strong effect on the control, and it seems to be the most critical parameter: if the averaging time is too large, the control acts on quantities that carry information not related with the actual state of the flow. On the other hand, if the averaging time is too short the input of the PI control does not have smooth stationary information, so it can input excessive energy into the system. If this parameter is not well tuned, two main effects can be expected: the transient time of the calculation increases and the simulation requires large amounts of CPU time; also, the steady state error can be

large and affect the results in the region downstream the last control plane.

Another issue that has an influence on the steady state results is the spanwise average that was used to define the error by previous researchers. The error, if no spanwise average is performed, reflects more accurately the local state of the flow, so that the PI control can locally adjust the control signal. Both the tuning of the time averaging window and the absence of spanwise average reflect the fact that in the feedback control is important to feed the PI control with the correct instantaneous information that allow for a correct response. Any delay can be dangerous.

To summarize the effect of K_I and K_P in the control it is conceptually useful to divide the computational domain in two regions: the controlled one, where the PI control is activated and the region downstream the control. The controlled region does not have a fluid-dynamical interest because it is not a region where realistic turbulence exists, but it is seen as a transition from RANS to LES, in which a mismatch from the desired quantities is tolerated. However, from the point of view of the control, in this region the PI control tries to match the target: the two constants K_I and K_P determinate the steady-state match of the desired quantities. If these two constants are not well-tuned, we can have a large steady state error within that region. A residual error, however, has a weak effect on the result in the region downstream the controlled one, as can be seen in the work of Keating *et al.* [30]. In fact, downstream of the last control plane the flow is biased to the exact solution of the NS equation. This is true especially when an external forcing is

applied to the flow (3D Boundary layer, Adverse Pressure gradient boundary layer): the bias in these cases is even stronger than in a boundary layer where no external force is applied (as the zero pressure gradient case). However, if the external forcing has the opposite trend of the control, the natural bias could not work. This is the case of the favorable pressure gradient: the acceleration damps the turbulent kinetic energy in the inner layer, instead the control tries to add energy towards a RANS solution with strong modeling errors. As was shown in the results, this kind of flow was extremely tedious to control. The same is true for the ZPG boundary layer: there is no external force and the solution in the region downstream the control is more sensible to the choice of the parameters.

The coefficient K_I and K_P have a strong influence in the stability of the system. Destabilization can be obtained if the PI system (or any other systems close in a feedback loop) introduce a lag in the loop. If K_I is too large or K_P too small the output of the PI control can be affected by a time lag that can destabilize the Navier-Stokes equations. However, for stable values of K_P and K_I , the results outside the control region are insensitive to these parameters.

6.1.2 Applications

In the hybrid RANS/LES results, we found that an important part is played by the modeling error in the RANS solution. In the zero pressure gradient and adverse pressure gradient boundary layer, we found that a rapid adjustment to the

LES results is obtained when the $k - \epsilon$ model is used in the RANS region. The fact that this model gives independent values of k and ϵ , while with the SA model must be estimated empirically, is a particularity desirable feature. In the favorable pressure gradient, on the other hand, any of the RANS model was unable to predict correctly the behavior of the flow. In the 3D boundary layer, we have seen that a recovery of the main shear stress $\langle u'v' \rangle$ and the secondary shear stress $\langle v'w' \rangle$ is obtained, with the forcing applied only to the $\langle u'v' \rangle$ stress. However, if the wrong time-averaging is used, the secondary stress is not matched.

In the case of the zero pressure gradient and 3D boundary layer, we tried to force the turbulent kinetic energy production in order to have a control that was coordinate-invariant. We tested a production-based error in these two flows obtaining the same result as in the Reynolds stress-based error; the only difference was in the controlled region: here the steady state error was large in the outer part of the boundary layer.

6.2 Resolved LES of the favorable pressure gradient boundary layer

Large-eddy simulation of flat-plate boundary layers in favorable pressure gradients (FPG) are performed for two different acceleration parameters. The high-acceleration case is in good agreement with the experimental data by Fernholz and Warnack [96, 97]. Substantial reduction in turbulent kinetic energy and shear stress production, and a reduction of the bursting frequency indicate that the inner part of

the accelerated boundary layer is in a laminar-like state when the pressure-gradient parameter K exceeds a threshold value. Downstream of this region, the boundary layer has a fast re-transition to turbulence. In the low K case, the boundary layer does not depart significantly from equilibrium. In the outer part of the boundary layer, the turbulent kinetic energy and the shear stress correlation maintained the same level as before the acceleration began. Two main hypotheses have been made: the inner and outer layers do not interact; or, the relaminarization is the consequence of inner-outer layer coupling. The results of our well-resolved calculations of the FPG boundary layer highlighted some significant differences in the inner-outer layer interactions compared to a canonical ZPG case. They did not, however, allow us to determine whether the relaminarization process begins in the inner layer and propagates outwards, or if the reorganization of the outer layer forces the inner layer to become more stable.

6.3 Future work

An important extension of the hybrid RANS/LES calculation is to compressible flow. The use of controlled forcing in this case can be challenging, because the control that we examined adds energy into the domain. One possible consequence is that not all the energy goes in turbulent fluctuations but a fraction of that can be found as internal energy; this would make the method less effective and could require different control strategies. One first step to allow the extension to com-

pressible flow, could be the finding of more accurate control coefficients. This can be possible if a simplified model of the Navier-Stokes equation is found, so that well-known tested models can be applied to the feedback control.

Regarding the favorable pressure gradient boundary layer, in order to give an answer to the issue of inner-outer layer coupling, a possible strategy is perform falsifying experiments [106]. In a first set of simulations the flow can be manipulated to suppress the outer layer eddies and observes the behavior of the inner layer. In a second set of calculations the turbulence in the inner layer can be removed, and study the development of the outer layer in isolation. Another possibility is to study a single horseshoe vortex subjected to acceleration to determine whether the outer-layer re-organization is due to the freestream acceleration only, or if it is affected by the decreased frequency of the bursts also.

Bibliography

- [1] Spalart, P.R. 2000 “Strategies for turbulence modelling and simulations” *Int. J. Heat Fluid Flow*, **21**, 252-263.
- [2] Chapman, D.R. Computational aerodynamics, development and outlook. *AIAA J* **17** 1293-1313
- [3] Piomelli, U. and Balaras, E. 2002 “Wall-layer models for large-eddy simulations,” *Annu. Rev. Fluid Mech.* **34**, 349 (2002).
- [4] Sagaut, P., Deck, S., Terracol, M. 2006 Multiscale and multiresolution approaches in turbulence *Imperial College Press* .
- [5] Spalart, P.R., Jou, W.H., Strelets, M. and Allmaras, S.R. 1997 “Comments on the feasibility of LES for wings, and on a hybrid RANS/LES approach,” In *Advances in DNS/LES*, edited by C. Liu and Z. Liu, (Greyden Press, Columbus, OH).
- [6] Balaras, E., Benocci, C. 1994 Subgrid-scale models in finite-difference simulations of complex wall bounded flows. *AGARD CP 551* pp 2.1-2.5
- [7] Speziale, C. 1997 Turbulence modelling for time-dependent RANS and VLES: A review. *AIAA Paper 97-2051*
- [8] Batten, P., Goldberg, U. and Chakravarthy, S. 2000 Sub Grid Turbulence Modeling for Unsteady Flow with Acoustic Resonance *AIAA Paper 2000-0473* .
- [9] Spalart, P.R., Deck, S., Shur, M.L., Squires, K.D., Strelets, M. Kh. and Travin, A., 2006, A new version of detached-eddy simulation, resistant to ambiguous grid densities. *Theo. Comput. Fluid Dyn.*, **20**, 181–195.
- [10] Girimaji, S.S., Abdol-Hamid, K.S. 2005 Partially-averaged Navier Stokes Model for Turbulence: Implementation and Validation *AIAA 2005-502* pp 1-14
- [11] S. Deck, 2005 Zonal-detached-eddy simulation of the flow around a high-lift configuration *AIAA J.* **43:11**, 2372–2384.

- [12] Nikitin, N.V., Nicoud, F., Wasistho, B., Squires, K.D. and Spalart, P.R. 2000 An approach to wall modeling in large-eddy simulations. *Physics of Fluids*, **12**, 1629-1632.
- [13] Cabot, W. Moin, P. 2000 Approximate wall boundary conditions in the large-eddy simulation of high Reynolds number flows. *Flow Turbulent Comb* **63**, 269
- [14] Hamba, F. 2003 A hybrid RANS/LES simulation of turbulent channel flow. *Theoret. Comput. Fluid Dyn.*, **16**, 387-403.
- [15] Piomelli, U. Balaras, E. Pasinato, H. Squires, K.D. and Spalart, P.R. 2003 The inner-outer layer interface in large-eddy simulations with wall-layer models *Int. J. Heat Fluid Flow*, **24**, 538.
- [16] Davidson, L. and Dahlstrom, S. 2005 Hybrid LES-RANS: An approach to make LES applicable at high Reynolds number. *19*, 415-427.
- [17] Temmerman, L., Hadziabdic, M., Leschziner, M. A. and Hanjalic, K. 2005 A hybrid two-layer URANS-LES approach for large eddy simulation at high Reynolds numbers. *International journal of heat and fluid flow*, **26**, 173-190.
- [18] Davidson, L. and Billson, M. 2006 Hybrid LES-RANS using synthesized turbulent fluctuations for forcing in the interface region. *International journal of heat and fluid flow*, **27**, 1028-1042
- [19] Hamba, F. 2006 A hybrid RANS/LES simulation of high-Reynolds-number channel flow using additional filtering at the interface. *Theoret. Comput. Fluid Dyn.*, **20**, 89-101.
- [20] Keating, A. and Piomelli, U. 2006 A dynamic stochastic forcing method as a wall-layer model for large-eddy simulation. *J. of Turbulence*, **7(12)**, 1-24.
- [21] Tessicini, F. Temmerman, L. Leschziner, M.A. 2006 Approximate near-wall treatments based on zonal and hybrid RANS-LES methods for LES at high Reynolds numbers. *Int. J. Heat and fluid flow*, **27**, 789-799.
- [22] Benarafa, Y. Cioni, F. Ducros, F. Sagaut, P. 2006 RANS/LES coupling for unsteady turbulent flow simulation at high Reynolds number on coarse meshes *Comput. Methods Appl. Mech. Engrg.* **195**, 2939-2960

- [23] Dahlstrom S., Davidson L. 2003 Hybrid LES-RANS with additional conditions at the matching region *Turbulence heat and mass transfer 4* Ney York, Wallingford (UK)
- [24] Labourasse, E. and Sagaut, P. 2002 Reconstruction of turbulent fluctuations using a hybrid RANS/LES Approach *Journal of Comp. Physics* **182**, 301-336
- [25] Terracol, M. 2005 A zonal RANS/LES approach for noise sources prediction. In *Engineering Turbulence Modelling and Experiments 6* edited by W. Rodi and M. Mulas, Elsevier, Amsterdam, 699–708.
- [26] Sagaut, P., Garnier, E., Tromeur, E., Larchevêque, L., and Labourasse, E, 2004, Turbulent inflow conditions for LES of compressible wall-bounded flows, *AIAA J.* **42**, 469–477.
- [27] Sandham, N.D., Yao, Y.F., Lawal, A.A., 2003, Large-eddy simulation of transonic turbulent flow over a bump *Int. J. Heat FLuid Flow*, **24**, 584–595.
- [28] Mathey, F. Cokljat, D. Bertoglio, J.P. and Sergent, E., 2006, Assessment of the vortex method for Large Eddy Simulation inlet conditions *Progress in Comp Fluid Dynamics* **6**, 58–67
- [29] Sanchez-Rocha, M. Kirtas, M. Menon, S. 2006 Zonal Hybrid RANS-LES method for static and oscillating airfoils and wings *AIAA Paper 2006-1256*
- [30] Keating, A., De Prisco, G., and Piomelli, U., 2006 Interface conditions for hybrid RANS/LES calculations *Int. J. Heat FLuid Flow*, **27**, 777–788.
- [31] Batten P., Goldberg, U. and Chakravarthy, S. 2004 Interfacing statistical turbulence closures with large-eddy simulation, *AIAA J.* **42**, 485–492.
- [32] Davidson, L. 2005 Hybrid LES-RANS: Inlet boundary conditions *Proc. 3rd National Conf. Comput. Mech.*, 7–22.
- [33] Sandham, N.D., Yao, Y.F., Lawal, A.A. 2003 Large-eddy simulation of transonic turbulent flow over a bump *Int. J. Heat FLuid Flow*, **24**, 584–595.
- [34] Spalart, P.R. 1986 Numerical study of sink-flow boundary layers *J. Fluid Mech.*, **172**, 307 (1986).

- [35] Spalart, P.R. 1986 Direct simulation of a turbulent boundary layer up to $Re_\theta=1410$ *J. Fluid Mech.*, **187**, 61.
- [36] Spalart, P.R. and Watmuff, J.H. 1993 Experimental and numerical study of a turbulent boundary layer with pressure gradients *J. Fluid Mech.*, **249**, 337.
- [37] Lund, T.S. Wu, X. and Squires, K.D. 1998 Generation of inflow data for spatially-developing boundary layer simulations *J. Comput. Phys.*, **140**, 233.
- [38] Ferrante A. and Elghobashi, S.E. 2004 A robust method for generating inflow conditions for direct simulations of spatially-developing turbulent boundary layers *J. Comput. Phys.* **198**, 372.
- [39] Schlüter, J.U., Wu, X., Kim, S. Alonso, J.J. and Pitsch, H., 2004, Coupled RANS-LES computation of a compressor and combustor in a gas turbine engine. *AIAA Paper 2004-3417*.
- [40] Schlüter, J.U. Pitsch, H. and Moin, P. 2004 LES inflow conditions for coupling with Reynolds-averaged flow solvers *AIAA J.*, **42**, 478.
- [41] Medic, G. You, D. and Kalitzin, G. 2006 An approach for coupling RANS and LES in integrated computations of jet engines *CTR Annual Research Briefs*
- [42] Schlüter J.U., Pitsch H., Moin P. 2002 Consistent boundary conditions for integrated LES/RANS conditions *AIAA paper*
- [43] Batten P., Goldberg, U. and Chakravarthy, S. 2002 LNS- An approach Towards Embedded LES, *AIAA 2002-0427*, 1–10.
- [44] Le, H. Moin, P. and Kim, J. 1997 Direct numerical simulation of turbulent flow over a backward-facing step *J. Fluid Mech.*, **330**, 349.
- [45] Lee, S. Lele, S. and Moin, P. 1992 Simulation of spatially evolving compressible turbulence and application of Taylor's hypothesis," *Phys. Fluids A* **4**, 1521.
- [46] Kraichnan, R.H. 1969 Diffusion by a random velocity field *Phys. Fluids* **13**, 22-31
- [47] Smirnov, A. Shi, S. and Celik, I. 2001 Random flow generation technique for large eddy simulations and particle-dynamics modeling *J. Fluids Eng.*, **123**, 359.

- [48] Klein, M. Sadkiki, A. and Janicka, J. 2003 A digital filter based generation of inflow data for spatially developing direct numerical or large eddy simulations *J. Comput. Phys.*, **186**, 652.
- [49] Spille-Kohoff, A. and Kaltenbach, H.-J. 2001 Generation of Turbulent Inflow Data with a Prescribed Shear-Stress Profile. In *DNS/LES Progress and challenges*, edited by C. Liu, L. Sakell, T. Beutner (Greyden, Columbus, OH, 2001), 319–326.
- [50] Keating, A., Piomelli, U., Balaras, E. and Kaltenbach, H.-J., 2004, A priori and a posteriori tests of inflow conditions for large-eddy simulation, *Phys. Fluids* **16**, 4696–4712.
- [51] Keating, A. 2003 Large-eddy simulation of Heat transfer in turbulent channel flow and in the turbulent flow downstream of a backward-facing step, PhD dissertation, *The University of Queensland, Brisbane, Australia*
- [52] Lilly, D.K. 1967, The representation of small-scale turbulence in numerical simulation experiments *Proceedings of the IBM Scientific Computing Symposium on Environmental Sciences, Yorktown Heights, NY*
- [53] Moin, P. and Kim, J. 1982 Numerical Investigation of Turbulent Channel Flow, *Journal of Fluid Mechanics* **118**, 341–377
- [54] Piomelli, U. and Zang, T.A. and Speziale, C.G. and Hussaini, M.Y. 1990, On the large-eddy simulation of transitional wall bounded flows, *Physics of Fluids A* **1** 257–265
- [55] Clark, R.A. and Ferziger, J.H. and Reynolds, W.C. 1979 Evaluation of subgrid-scale turbulence models using an accurately simulated turbulent flow *Journal of Fluid Mechanics* **91**, 1–16
- [56] Liu, S. and Menveau, C. and Katz, J. 1994, On the properties of similarity subgrid-scale models as deduced from measurements in a turbulent jet *Journal of Fluid Mechanics* **275**, 83–119
- [57] Vreman, B. and Geurts, B. and Kuerten, H. 1997 Large-eddy simulation of the turbulent mixing layer *Journal of Fluid Mechanics*, **339**, 357–390
- [58] Bardina, J. and Ferziger, J.H. and Reynolds, W.C. 1980, Improved subgrid-scale models for large-eddy simulations, *AIAA Paper 80-1357*

- [59] Germano, M. Piomelli, U. Moin, P. and Cabot, W. 1991 A dynamic subgrid-scale eddy viscosity model *Phys. Fluids* **3**, 1760.
- [60] Lilly, D.K. 1992 A proposed modification of the Germano subgrid-scale closure model, *Physics of Fluids A*, **4**, 633-635
- [61] Spalart, P.R. and Moser, R.D. and Rogers, M.M. 1991 Spectral methods for the Navier-Stokes equations with one infinite and two periodic directions *Journal of Computational Physics* **96**, 297-324
- [62] Akselvoll, K. and Moin, P. 1996 An efficient method for temporal integration of the Navier-Stokes equation in confined axisymmetric geometries *Journal of Computational Physics* **125** 454-463
- [63] Morinishi, Y. and Lund, T.S. and Vasilyev, O.V. and Moin, P. 1998 Fully conservative higher order finite difference schemes for incompressible flow *Journal of Computational Physics* **143**, 90-124
- [64] Moin, P. and Mahesh, K. 1998 Direct numerical simulation: A Tool for Turbulence Research, *Annual Review of Fluid Mechanics* **30**, 539-578
- [65] Harlow, F.H. and Welch, J.E. 1965 Numerical calculation of time-dependent viscous incompressible flow of fluid with free surface. *The Physics of Fluids* **8**, 2182-2189
- [66] Akselvoll, K. 1995 Large eddy simulation of turbulent confined coannular jets and turbulent flow over a backward facing step, *PhD thesis, Stanford University*
- [67] Piomelli, U. 1993 High Reynolds number calculations using the dynamic subgrid-scale stress model, *Physics of Fluids A* **5**, 1484-1490
- [68] Ghosal, S. and Moin, P. 1995 The basic equations for the large eddy simulation of turbulent flows in complex geometry, *Journal of Computational Physics* **118**, 24-37
- [69] Cabot, W. and Moin, P. 1993 Large eddy simulation of scalar transport with the dynamic subgrid-scale model, *Large eddy simulation of complex engineering and geophysical flows*, Cambridge University Press
- [70] Spalart, P.R. and Allmaras, S.R. 1992 A one-equation model for aerodynamic flow *AIAA paper 92-0439*

- [71] Launder, B.E., and Spaulding, D.B., 1972, *Lectures in mathematical models of turbulence*, Academic Press, London.
- [72] Chen, H.C., and Patel, V.C., 1988, Near-wall turbulence models for complex flows including separation. *AIAA J.* **26**, 641–648.
- [73] Bradshaw, P. Ferriss, D.H. Atwell, N.P. 1967 Calculation of boundary layer development using the turbulent energy equation *Journal Fluid Mechanics* **23**, 31-64
- [74] Townsend, A.A. Equilibrium layers and wall turbulence 1962 *Journal Fluid Mechanics* **11** 97-120
- [75] Menter, F.R. Eddy viscosity transport equations and their relation to $k - \epsilon$ model *Journal Fluids Engineering* **119**, 876-884
- [76] Cohen, G.H. and Coon, G.A. 1953 Theoretical consideration of retarded control, *Trans. ASME* **75**, pp 827-834
- [77] Balaras,E. Benocci,C. Piomelli,U. Two-layer approximate boundary conditions for large-eddy simulations 1996 *AIAA J.*, **34**, 1111.
- [78] Benarafa Y., Cioni F., Ducros F., Sagaut P. 2006 RANS/LES coupling for unsteady turbulent flow simulation at high Reynolds number on coarse meshes” *Comput. Methods Appl. Mech. Engrg*, **195**, 2939-2960
- [79] Spalart, P.R. and Allmaras, S. R. 1994 *La Recherche Aéronautique*, **1**, 5–.
- [80] Meneveau,C. Lund,T.S. and Cabot,W.H. 1996 A Lagrangian dynamic subgrid-scale model of turbulence J. Fluid Mech. **319**, 353–.
- [81] Kim,J. and Moin,P. 1985 Application of a fractional step method to incompressible Navier-Stokes equations *J. Comput. Phys.*, **59**, 308.
- [82] Orlanski,I. 1976 A simple boundary condition for unbounded hyperbolic flows *J. Comput. Phys.* **21**, 251.
- [83] Sreenivasan, K.R. (1982) Laminarising, Relaminarizing and Retransitional Flows. *Acta Mech.* **44**, pp.1–48.

- [84] Narasimha, R. and Sreenivasan, K.R. (1973) Relaminarization in highly accelerated turbulent boundary layers. *J. Fluid Mech.* **61**, pp.417–447.
- [85] Narasimha, R. and Sreenivasan, K.R. (1979) Relaminarization of Fluid Flows. *Adv. Appl. Mech.* **19**, pp.221–309.
- [86] Wilson, D. (1954) Convective heat transfer to gas turbine blades. *Proc. Inst. Mech. Eng.*
- [87] Patel, V. and Head, M. (1968) Reversion of turbulent to laminar flow. *J. Fluid Mech.* **34**, pp 371–392
- [88] Senoo, Y. (1972) The boundary layer on the end wall of a turbine nozzle cascade. *Transaction of the ASME. MIT Gas Turbine Laboratory.* **35**, pp 1711–1720
- [89] Launder, B.E., (1963) The Turbulent Boundary Layer in a Strongly Negative Pressure Gradient Gas. *MIT Gas Turbine Laboratory Report* **71**, pp. 1–28
- [90] Launder, B.E., (1964) Laminarisation of the Turbulent Boundary Layer by Acceleration. *MIT Gas Turbine Laboratory Report* **77**, pp. 1–50
- [91] Badri Narayanan, M., Rajagopalan, S. and Narasimha, R. (1977) Experiment on the fine structure of turbulence. *J. Fluid Mech.* **80**, pp. 237–257.
- [92] Kline, S., Reynolds, W., Schraub, F. and Runstadler, P. (1967) The structure of turbulent boundary layers. *J. Fluid Mech.* **30**, pp. 741–773.
- [93] Blackwelder, R.F. and Kovasznay, L.S.G. (1972) Large-scale motion of a turbulent boundary layer during relaminarization *J. Fluid Mech.* **53**, pp. 61–83
- [94] Falco, R.E. (1980) Combined simultaneous flow visualization/hot-wire anemometry for the study of turbulent flows *J. Fluids Eng.* **102**, pp. 174–182
- [95] Ichimiya, M., Nakamura, I., and Yamashita, S. (1998) Properties of a relaminarizing turbulent boundary layer under a favorable pressure gradient *Exp. Thermal Fluid Sci.* **17**, pp. 37–48
- [96] Fernholz, H.H. and Warnack, D. (1998) The effects of a favourable pressure gradient and of the Reynolds number on an incompressible axisymmetric turbulent boundary layer. Part 1. The turbulent boundary layer. *J. Fluid Mech.* **359**, pp. 329–356.

- [97] Warnack, D. and Fernholz, H.H. (1998) The effects of a favourable pressure gradient and of the Reynolds number on an incompressible axisymmetric turbulent boundary layer. Part 2. The boundary layer with relaminarization. *J. Fluid Mech.* **359**, pp. 357–381.
- [98] Escudier, M.P., Abdel-Hameed, A., Johnson, M.W. and Sutcliffe, C.J. (1998) Laminarisation and re-transition of a turbulent boundary layer subjected to favourable pressure gradient. *Exp. Fluids* **25**, pp. 491–502.
- [99] Piomelli, U., Balaras, E., & Pascarelli, A. (2000) Turbulent structures in accelerating boundary layers. *J. Turbulence* **1** (001) pp. 1–16.
- [100] Germano, M., Piomelli, U., Moin, P. and Cabot W. H. (1991) A dynamic subgrid-scale eddy viscosity model. *Phys. Fluids A* **3**, pp. 1760–1765.
- [101] Lilly, D. K. (1992) A proposed modification of the Germano subgrid-scale closure method. *Phys. Fluids A* **4**, pp. 633–635.
- [102] Lund, T. S., Wu, X., and Squires, K. D. (1998) Generation of turbulent inflow data for spatially-developing boundary layer simulations, *J. Comput. Phys.* **140**, pp. 233–258.
- [103] Chorin, A. J. (1968) Numerical solution of the Navier-Stokes equations. *Math. Comput.* **22**, pp. 745.
- [104] Schlichting, H. (1979) Boundary layer theory, McGraw Hill, New York.
- [105] Dubief, Y., and Delcayre, F. (2000) On coherent-vortex identification in turbulence. *Journal of Turbulence* **1**, 1-22.
- [106] Jimenez, J. and Pinelli, A. 1999, The autonomous cycle of near-wall turbulence. *J. Fluid Mech.*, **389**, 335 – 359